

**Enhancing understanding of mineral accessible surface area to improve
simulation of mineral reaction rates in porous media**

by

Fanqi Qin

A dissertation submitted to the Graduate Faculty of
Auburn University
in partial fulfillment of the
requirements for the Degree of
Doctor of Philosophy

Auburn, Alabama
August 7, 2021

CO₂-brine-mineral reaction, accessible surface area, image processing, reactive
transport modeling, core-flood experiment

Copyright 2021 by Fanqi Qin

Approved by

Lauren E. Beckingham, Chair, Assistant professor, Department of Civil and
Environmental Engineering

Mark O. Barnett, Professor, Department of Civil and Environmental Engineering

Joel Hayworth, Associate Professor, Department of Civil and Environmental
Engineering

Ming-kuo Lee, Professor and Chair, Department of Geosciences

Tae-Sik Oh, Assistant Professor, Department of Chemical Engineering

Abstract

Geological formations have great potential for large scale carbon sequestration, where the CO₂ is mineralized through geochemical reactions. These reactions are rather complex and can potentially alter the formation properties including porosity and permeability. Reactive transport modeling is a powerful tool to enhance the understanding of the impact of CO₂ injection on formation properties by simulating the CO₂-brine-mineral reactions over both laboratory- and geological- time scales. Mineral reactive surface area (RSA) is one of the rate-controlling parameters in geochemical reactions, where 1 – 5 orders of magnitude variations in mineral reactive surface area have been reported in the literature. These surface areas are measured/estimated through different methods, such as Brunauer–Emmett–Teller (BET) adsorption method, geometry approximations and imaging techniques. Previous work has found that simulations carried out using mineral accessible surface areas calculated from imaging better reproduces the changes observed in core-flood experiments. However, how accessible mineral surface area is impacted by image resolution, how simulations are impacted by surface area variations and if mineral accessible surface area is predictable remain to be answered. This work aims to improve our understanding of mineral accessible surface area and explore the possibility of predicting mineral accessible surface areas from other mineral properties such as mineral abundance. To understand the impact of image resolution on quantified mineral properties, a rock sample extracted from the Paluxy formation (Kemper, Mississippi) was imaged using scanning electron microscope under varying resolutions (0.34 μm to 5.71 μm). Porosities and mineral abundances agree relatively well with changing resolutions, while less than one order of magnitude variations were observed in mineral accessible surface areas. Accessible surface areas from high (0.34 μm) and low (5.71 μm) resolution images were then used in continuum-scale reactive transport simulations to study the impact of image resolution on simulated mineral reactions. Only minor differences were observed between the simulations at both short (1 week) and long time-scales (20 years), indicating the impact of variations in surface area resulting from image resolution on simulated reactions is small. Simulations were also carried out using geometric surface area and BET specific surface area from the literature to understand how surface area variation affects simulated reactions. Small variations were observed at short times, where carbonate minerals are slightly impacted by surface area variations. At longer times, large differences occurred in simulated reactions for non-carbonate mineral phases. Depending on mineral composition and simulation duration, it is not always necessary to quantify mineral accessible surface area from imaging. While imaging approaches are a promising means of estimating reactive surface area values, this approach is time and resource intensive. Here, further investigation of the relationships among the quantified mineral properties including mineral abundance, accessibility, accessible surface area, clay content and connected surface area is explored as a means of predicting mineral accessible surface area without extensive image processing. Ten

sandstone samples were imaged and processed using similar approaches to quantify mineral properties, and the results were compared to explore the relationships among these properties. No distinct pattern was found to directly link mineral accessible surface area to other properties determined from imaging. However, the accessibilities of quartz and feldspars were found to be predictable based on their abundances as well as clay content. Lastly, efforts were made to understand the evolution of accessible mineral surface area as mineral dissolution reactions progress. Core-flood experiments were performed on Bandera Grey and Kentucky sandstone samples using 0.01 M hydrochloric acid (HCl) as the reacting fluid. Mineral accessible surface areas before and after the experiments were calculated using the imaging approach and compared to evaluate the changes of surface area for different mineral phases.

Acknowledgements

It is a genuine pleasure to express my deep gratitude and appreciation to my mentor, Dr. Lauren E. Beckingham, who has been patient, resourceful, responsible and provided the help, guidance and advice I need to complete my work. I truly appreciate what she has taught me over the five years of my Ph.D. journey, not only for the knowledge I acquired as a researcher, but also for all the lessons I learned and all abilities I've developed as a person. All these things will continue to influence and benefit my career as well as my life. To me, this is a priceless gift, and no words can express how grateful I am for everything that she has done and taught me.

As the only child in my family, who has traveled half of the earth, coming to a new country, life has changed for me as well as for my parents over these years. There are ups and downs in life, and I felt sorry for those times I couldn't be there to keep company to my parents when they needed help and support. All I heard from them are good news, and they kept those hard times to themselves. Being the son of my parents is the proudest thing of my life as the love they gave me is more valuable than anything else in this world. I sincerely thank my parents for their care, support and understanding for me, and wish they will always be happy and healthy.

Being in WRISES group over the five years, I've got the chance to know and work with people from all of the world. Chidera Iloejesi from Nigeria, Ishan Anjekar from India, Jeffery Steinwinder from Mississippi, Olivia Brunhoeber from Alabama, Md. Fahim Salek from Bangladesh and Parisa Asadi from Persia. It was a truly amazing experience working and learning with them. This group is energetic, supportive, resourceful and there is great "chemistry" in this group. I really appreciate the help and support from all of the group members.

I was never good at expressing my gratitude, but I always remember those who has helped, supported me in my life. Here I want to give my sincerest thanks to all of you, it was an amazing experience for me to get to know and to work with all of these wonderful people. You have made my life better and made me a better person. Thank you all!

Table of Contents

Abstract.....	2
Acknowledgements	4
Chapter 1. Introduction.....	11
1.1 Impact of image resolution on quantified mineral properties	11
1.2 The impact of image resolution on simulated mineral reactions	12
1.3 Relationships among the quantified mineral properties	13
1.4 Mineral accessible surface area evolution	14
Chapter 2. Impact of image resolution on quantification of mineral abundances and accessible surface areas	16
Abstract.....	16
2.1 Introduction	16
2.2 Materials and methods	19
2.2.1 Samples and sample preparation.....	19
2.2.2 2D SEM Imaging	20
2.2.3 3D X-ray CT imaging	22
2.2.4 Accessible surface area quantification	23
2.3 Results	24
2.3.1 SEM Imaging	24
2.3.2 3D X-ray CT imaging	32
2.4. Discussion.....	34
Conclusions.....	36
Acknowledgement	38
Reference	38
Chapter 3. The impact of mineral reactive surface area variation on simulated mineral reactions and reaction rates	43
Abstract.....	43
3.1. Introduction.....	43
3.2. Materials and methods	46
3.2.1 Sample characterization	46
3.2.2 Reactive transport simulations	47
3.3. Results	51
3.3.1 Imaging-based simulations	52
3.3.2 Non-imaging based simulations.....	57

3.3.3 Mineral surface area evolution.....	62
3.4. Discussion.....	64
Conclusions.....	68
Acknowledgement.....	71
References.....	71
Chapter 4. Estimation of mineral accessible surface area from mineral abundance and clay content.....	78
4.1 Introduction.....	78
4.2 Materials and Methods.....	80
4.2.1 Sample characterization and preparation.....	80
4.2.2 Imaging acquisition and mineral properties quantification.....	80
4.3 Results.....	82
4.3.1 Image processing and mineral property quantification.....	82
4.3.2 Relationship evaluation of quantified mineral properties.....	91
4.4 Discussion.....	97
Conclusions.....	98
Acknowledgement.....	99
References.....	100
Chapter 5. Evaluation of mineral accessible surface area evolution induced by geochemical reactions.....	104
5.1 Introduction.....	104
5.2 Materials and methods.....	105
5.2.1 Sample characterization and preparation.....	105
5.2.2 Mineral properties quantification.....	106
5.2.3 Core-flood dissolution experiments.....	108
5.2 Results.....	109
5.3.1 Image segmentation and mineral property quantification.....	109
Future work:.....	114
5.3.1 Effluent sample analysis.....	115
Future work:.....	115
5.4 Discussion.....	116
Acknowledgement.....	116
References.....	117
Chapter 6. Conclusions and contribution to new knowledge.....	119

6.1 Enhanced understanding of the impact of image resolution on quantified mineral properties.....	119
6.2 Improved understanding of the impact of surface area variation on simulated reactions	119
6.3 Connections between the quantified mineral properties and estimation of mineral accessibility without image processing	120
6.4 Mineral surface area evolution during mineral reactions.....	121

List of Tables

Table 2.1.....	20
Table 2.2.....	24
Table 2.3.....	28
Table 2.4.....	29
Table 2.5.....	30
Table 2.6.....	30
Table 2.7.....	33
Table 2.8.....	34
Table 3.1.....	47
Table 3.2.....	48
Table 3.3.....	49
Table 3.4.....	64
Table 3.5.....	69
Table 4.1.....	89
Table 4.2.....	92
Table 5.1.....	106
Table 5.2.....	106
Table 5.3.....	110
Table 5.4.....	113

List of Figures

Figure 2. 1	25
Figure 2. 2	26
Figure 2. 3	27
Figure 2. 4	29
Figure 2. 5	32
Figure 3. 1	48
Figure 3. 2	52
Figure 3. 3	54
Figure 3. 4	55
Figure 3. 5	57
Figure 3. 6	59
Figure 3. 7	61
Figure 3. 8	62
Figure 3. 9	63
Figure 3. 10	65
Figure 4. 1	82
Figure 4. 2	83
Figure 4. 3	84
Figure 4. 4	85
Figure 4. 5	86
Figure 4. 6	87
Figure 4. 7	88
Figure 4. 8	93
Figure 4. 9	94
Figure 4. 10	95

Figure 4. 11	96
Figure 4. 12	97
Figure 5. 1	106
Figure 5. 2	108
Figure 5. 3	109
Figure 5. 4	109
Figure 5. 5	112
Figure 5. 6	113
Figure 5. 7	115

Chapter 1. Introduction

Mineral reactive surface area estimation is critical for understanding and predicting mineral reaction rates. Surface area can be estimated through different approaches such as the BET adsorption method (Brunauer et al., 1938), a geometric approximation (Anbeek, 1992; Gunter et al., 2000; Noiriél et al., 2009), and emerging imaging techniques (Peters 2009; Landrot et al., 2012; Beckingham et al. 2016). The estimated mineral reactive surface area using different approaches varies up to seven orders of magnitude (Black et al., 2015; Bourg et al., 2015). It has been proven in previous work (Beckingham et al., 2017) that mineral accessible surface area quantified from imaging better reproduces the mineral reaction rates observed in core-flood experiments. However, the impact of image resolution on the quantified mineral properties as well as on the simulated mineral reactions are unknown. During mineral reactions, the evolution of mineral surface area is not well understood. In addition, whether mineral accessible surface areas are predictable through other sample properties remains to be answered. This thesis improves our understanding of accessible mineral surface area in multi-mineralic porous media. Specifically, the impact of image resolution on mineral properties quantified from images, and implications for simulating mineral reactions and reaction rates is explored. In addition, the relationships among these quantified mineral properties and their evolution during dissolution are evaluated to explore the possibility of predicting mineral accessible surface area without complex image processing steps.

1.1 Impact of image resolution on quantified mineral properties

Imaging has emerged as a powerful means of porous media characterization, providing information on porosity, mineral abundances, surface roughness, and mineral surface areas. Optical microscopy, including petrographic microscopy and fluorescence light microscopy (FLM), are commonly used methods for characterization of pore space features but are often not adequate to accurately characterize pore shape, connectivity and other micro pore features (Bultreys et al., 2016). Scanning electron microscopy (SEM) can capture pore and grain features at higher resolutions than optical microscopy and it is capable of characterizing mineral volumes at microscopic scales when equipped with backscatter electron (BSE) detector and energy-dispersive X-ray spectroscopy (EDS) units. Automated mineral identification is even possible with proper calibration and the support of the correct software or means of post-processing (Bultreys et al., 2016). These images can then be evaluated to determine mineral porosity, abundances and accessibilities by pixel counting. While SEM can provide detailed information on microstructures and mineral identities in two dimensions, it cannot account for the nature of the pore-grain structure in three dimensions. Focused ion beam (FIB)-SEM can be used to capture images in three dimensions at high resolutions, however, it is inherently destructive in nature and is often practically limited in sample size (Xiong et al., 2016). X-ray computed tomography (X-ray CT) is

a non-destructive imaging technique, although limited in resolution to 100s of nm for micron scale samples, that can be used to capture images in three dimensions and to measure connected surface areas (Xiong et al., 2016; Beckingham et al., 2017). Combining accessibilities measured from 2D BSE images with connected surface area calculated from 3D CT images can yield mineral accessible surface areas (Landrot et al., 2012). These measured mineral properties can then be used as input to inform reactive transport simulations (Peters 2009, Beckingham et al. 2016).

While imaging can be utilized to parameterize reactive transport simulations, the variations in the technique or image processing approach may largely impact results as has been extensively considered for image thresholding (Wildenschild and Sheppard, 2013; Schlüter et al., 2014; Anovitz and Cole, 2015). In addition, images can be captured at a wide range of resolutions, the impact of which is largely unknown. This work uses a coupled imaging approach to process five SEM BSE images with resolution varying from 0.34 μm to 5.71 μm and addresses the following research questions:

- 1) Do the quantified mineral properties (porosity, abundance, accessibility and accessible surface area) vary with changing resolutions?
- 2) What properties are impacted most by image resolution differences?
- 3) What are the most impacted mineral phases and why they are impacted?

1.2 The impact of image resolution on simulated mineral reactions

Reactive transport modeling has been used extensively to enhance understanding of geochemical reactions and transport phenomena happening in a wide variety of surface and subsurface systems (Steeffel et al., 2005; Pallud et al., 2007; Boana et al., 2014). Evaluating CO_2 -induced dissolution and precipitation reactions and corresponding porosity and permeability evolution in subsurface environments (White et al., 2005; Audigane et al., 2007; Bacon et al., 2009; Navarre-Sitchler et al., 2011; Aradóttir et al., 2012; Nogues et al., 2013; Ng et al., 2015; Steefel et al., 2015) is one of them. However, simulating mineral reactions is challenging not only due to the complexity of the reactions, but also due to the uncertainties involved in the modeling. Mineral reaction rates are commonly estimated using a rate law based on transition state theory (TST) (Lasaga, 1981, 1984; Aagaard and Helgeson, 1982) where the reaction rate is given by,

$$R_m = A_m k_m [f \Delta G_r] \quad (1)$$

where A_m is mineral reactive surface area, k_m is mineral rate constant, and $f \Delta G_r$ is the thermodynamic driving force for the reaction (Steeffel et al., 2015). While the thermodynamic aspect of mineral reactions is generally well understood, difficulties exist in estimating rate constants under elevated conditions and mineral reactive surface

areas which may result differences in simulated results. Estimated rate constants typically vary one order of magnitude whereas variations in reported mineral surface area values span several orders of magnitude (Black et al., 2015; Bourg et al., 2015).

Mineral surface areas can be measured through the Brunauer–Emmett–Teller (BET) adsorption method (Brunauer et al., 1938), geometry approximations (Anbeek, 1992; Gunter et al., 2000; Noiriél et al., 2009) or through imaging techniques (Landrot et al. 2012; Beckingham et al., 2016 and 2017; Qin and Beckingham, 2019). Imaging and image analysis is powerful means of quantifying mineral properties to inform reactive transport simulations including accessible surface areas. However, capturing images under high resolutions and processing high resolution images is time-consuming and may have high computational costs. The necessity of this time and resource investment to improve simulation of mineral reactions and reactions rates, however, is not well understood. This work utilizes continuum scale reactive transport modeling to evaluate the following research questions:

- 1) Are the variations in mineral accessible surface area that result from image resolution differences affecting the simulated mineral reactions and reaction rates?
- 2) How different are the simulated mineral reactions and reaction rates when BET specific surface areas and geometric surface areas are used in the simulations?
- 3) What approaches should we use to quantify mineral surface areas? Is image processing always needed?

1.3 Relationships among the quantified mineral properties

Quantifying mineral accessible surface area from 2D BSE and 3D CT images has been proven to be valuable since simulations carried out using accessible surface areas yield satisfying results compared to the reaction rates observed in core-flood experiments (Beckingham et al., 2017). Therefore, quantifying mineral properties through the imaging processing technique is the preferred approach. However, the time and resources required for image acquisition, mineral phases segmentation, mineral property quantification can be tremendous. Mineral properties including porosity, abundance, accessibility can be quantified from 2D SEM BSE images while the connected surface area can be estimated from 3D CT images. The correlations among these estimated properties have not been evaluated. If certain correlations were found among these properties, for example, relationships between mineral abundances and accessible surface area or accessibility may be identified. These relationships would be beneficial to quantify mineral accessible surface area as it would significantly reduce the time and resources for quantifying mineral accessibility/accessible surface areas as compared to the multi-scale imaging approach.

In this work, we aim to evaluate the potential patterns and relationships among mineral properties measurable from images for various sandstone samples to explore the possibility of predicting mineral accessible surface areas without imaging processing. Mineral abundance, accessibility, accessible surface area, clay content and connected surface area are computed, compared and evaluated for their connections as well as their individual impact on other properties. Through analysis of these relationships, we aim to address the following research questions:

- 1) Can we predict mineral accessible surface area through other mineral properties like mineral abundance?
- 2) How does clay and carbonate content affect the estimated mineral accessible surface areas?

1.4 Mineral accessible surface area evolution

Mineral reactive surface area is one of the many controlling factors of geochemical reactions (Carroll et al., 2013; Navarre-Sistchleret al., 2013; Luhmann et al., 2017; Prikryl et al., 2017; Yang et al., 2018). It is also an important parameter in reactive transport modeling where the simulated reaction rates and extents are largely impacted by reactive surface area input. However, the evolution of mineral reactive surface area during geochemical reactions is not well understood. When pore connectivity increases (Navarre-Sistchleret al., 2013) or mineral grains disaggregate (Noiriel et al., 2009; Israeli and Emmanuel, 2018), mineral reactive surfaces area could increase. Conversely, rapid dissolution of fine mineral grains with large surface area (Noiriel et al., 2004; Noiriel et al., 2009) could decrease mineral reactive surface area.

Simulating changes in surface area is important for accurate quantification of mineral reaction rates. In CunchFlow (Steele et al., 2015), a powerful tool for multi-component reactive transport modeling, the reactive surface area is calculated and updated when there is change in mineral volume fraction and porosity. This is expressed as

$$A_m = A_{m,0} \left\{ \begin{array}{ll} [(\frac{\phi}{\phi_0})(\frac{\phi_m}{\phi_{m,0}})]^{2/3} & \text{dissolution} \\ [\frac{\phi}{\phi_0}]^{2/3} & \text{precipitation} \end{array} \right\} \quad (1)$$

where A_m represents mineral reactive surface area, $\phi_{m,0}$ represents the initial volume fraction of the mineral m and ϕ_0 refers to the initial mineral porosity. Similar relationships have been proposed and used in other studies (Lichtner, 1988; Emmanuel and Berkowitz, 2005; Carroll et al., 2013) in which the mineral grains are assumed to be spherical and have smooth surfaces. However, 2D BSE images captured using scanning electron microscopy reveal that most of the mineral surfaces are neither

smooth nor spherical. More importantly, these proposed relationships imply that the entire mineral surface is involved in reactions, whereas it is more likely that only a fraction of the surface will be actively involved in reactions within a multi-phase consolidated sample. Therefore, estimating mineral reactive surface areas in these systems is difficult and requires further investigation to improve our understanding.

This work aims to quantify the change of mineral accessible surface areas before and after core-flood dissolution experiments through imaging techniques to address the following research questions:

- 1) What changes have occurred during the experiments (e.g. porosity, abundance, accessible surface area, pore connectivity)?
- 2) Are the changes in mineral accessible surface areas different among different mineral species?
- 3) Do these changes follow the current theory?

Chapter 2. Impact of image resolution on quantification of mineral abundances and accessible surface areas

Fanqi Qin, Lauren E. Beckingham

Department of Civil and Environmental Engineering, Auburn University, AL, 36849

Published in *Chemical Geology*, 2019, 523(30), 31-41.

Abstract

Imaging has emerged as a valuable means of geological sample characterization and parameterizing reactive transport simulations where image analysis can provide porosity, mineral composition and mineral accessible surface area data, for example. Images can be collected using a variety of techniques and at a range of resolutions, yet the impact of image resolution on measured properties is largely unknown. In this work, the impact of 2D image resolution on the calculated mineral abundances, accessibilities and effective surface areas are examined for a sample from the Paluxy formation, Kemper County, Mississippi. Scanning electron microscopy (SEM) backscatter electron (BSE) images of thin sections were captured at resolutions ranging from 0.3 μm to 6 μm . Images were segmented into pores and discrete mineral phases using ImageJ and algorithms developed in MATLAB. Porosity, mineral abundances and mineral accessibilities were calculated by counting pore and mineral pixels in the segmented image where accessible minerals were deemed as those adjacent to the pore space. A 3D X-ray computed tomography (CT) image of a core sample was collected, segmented, and analyzed to evaluate the 3D connected porosity. Cuboids with the same total area as the 2D image were randomly sampled and used to calculate the 3D connected surface area. This was then multiplied by mineral accessibility to calculate accessible mineral surface areas for non-clay minerals. Minimum variations were observed for mineral abundances calculated from images with varying resolutions. For high resolution images, 0.3 μm to 1 μm , mineral accessibilities agreed relatively well. For images with resolutions from 1 μm to 6 μm , the calculated accessibility of smectite/illite decreased with decreasing resolution while quartz accessibility increased. This in turn resulted in higher effective surface areas for quartz with decreasing resolution. No significant variations were observed for calcite, siderite and K-feldspar.

2.1 Introduction

Reactive transport modeling is an essential tool that has been used in hydrology and soil physics to enhance understanding of contaminant transport (Apul et al., 2007; Xu et al., 2010; Essaid et al., 2015), in environmental geochemistry for weathering and CO₂ induced geochemical reactions (Audigane et al., 2007; White et al., 2010; Navarre-Sitchler et al., 2011; Ng et al., 2015) and in biogeochemistry to simulate uranium bioremediation and microbial induced calcite precipitation (Yabusaki et al., 2011; Martinez et al., 2014). Simulations have also been utilized to enhance understanding of

the potential impact of mineral reactions on formations properties (Knauss et al., 2005; Gaus, 2005, 2010, Steefel et al. 2015, Min et al. 2016, Prikryl et al. 2017, Liu et al. 2018, Hommel et al. 2018).

Depending on the application, reactive transport simulations can be built at both the continuum-scale and pore-scale (Li et al., 2006, Bashtani et al. 2018, Lamy-Chappuis et al. 2018). Continuum-scale models are based on a representative elementary volume with average properties of the system (Steefel et al., 2015). These simulations are constructed based on formation input data, including porosity, mineral abundances, mineral surface areas, and reaction rate constants, etc. which can be acquired through a variety of different techniques. Rate constants are often obtained from thermodynamic databases while porosity, mineral abundances and surface areas are often measured. X-ray diffraction (XRD), for example, is frequently used to analyze the mineral composition of rock samples, but only mineral phases with weight percentages larger than 0.33% - 5%, depending on the equipment, can be detected (O'Connell and Regalbuto, 2015). Simulations based on XRD results alone may omit potentially reactive mineral phases that are present at fractions less than detection limits, resulting in neglect of important chemical reactions.

Imaging has emerged as a powerful means of porous media characterization, providing information on porosity, mineral abundances, surface roughness, and mineral surface areas. Optical microscopy, including petrographic microscopy and fluorescence light microscopy (FLM), are commonly used methods for characterization of pore space features but are often not adequate to accurately characterize pore shape, connectivity and other micro pore features (Bultreys et al., 2016). Scanning electron microscopy (SEM) can capture pore and grain features at higher resolutions than optical microscopy. SEMs equipped with backscatter electron (BSE) mode and energy-dispersive X-ray spectroscopy (EDS) units enable characterization of mineral volumes at microscopic scales by providing chemical information of mineral phases. Automated mineral identification is even possible with proper calibration and the support of the correct software or means of post-processing (Bultreys et al., 2016). These images can then be evaluated to determine porosity and mineral abundances or volume fractions by pixel counting for input to reactive transport simulations (Peters 2009, Beckingham et al. 2016).

While SEM can provide detailed information on microstructures and mineral identities in 2D, it cannot account for the nature of the pore-grain structure in three dimensions. Focused ion beam (FIB)-SEM and X-ray computed tomography (X-ray CT) can be used to capture images in three dimensions. FIB-SEM imaging creates a 3D depiction of the sample from a series of high-resolution (nm) 2D SEM images, using an ion beam to mill away small layers from the surface of interest (e.g. Vilcaez et al. 2017). While FIB-SEM imaging facilitates high resolution 3D imaging, it is inherently destructive in nature and is often practically limited in sample size (Xiong et al., 2016). X-ray CT imaging has the advantage of being non-destructive and non-invasive but is

often limited in image resolution where high-resolution X-ray CT imaging requires use of a synchrotron (Xiong et al., 2016; Beckingham et al., 2017). Furthermore, phase identification in X-ray CT images is limited and often requires use of a second, complementary, analysis (Beckingham et al., 2013, Ellis and Peters 2016, Liu et al 2018).

Accurate simulation of mineral reaction rates in porous media is crucial to assessing the reactive changes in the system, including porosity and permeability evolution. Mineral reaction rates are commonly simulated using a rate law based on transition state theory (Lasaga, 1981, 1984; Aagaard and Helgeson, 1982) where the reaction rate is given by,

$$R_m = A_m k_m [f \Delta G_r] \quad (1)$$

where A_m is the reactive surface area ($\text{m}^2 \text{m}^{-3}$ porous medium), k_m is the rate constant ($\text{mol m}^{-2} \text{s}^{-1}$), and $f \Delta G_r$ is the thermodynamic driving force for the reaction (Steele et al., 2015). Large imprecisions have been observed in simulations of mineral reaction rates especially when upscaling from the pore-scale to continuum-scale (Atchley et al. 2014; Liu et al. 2015; Tutolo et al. 2015; Beckingham et al., 2016; Al-Khulaifi et al., 2017; Navarre-Sitchler and Jung 2017). Reaction rates depend on a variety of parameters including temperature, pH, reactivity of the phase, surface area, etc. (Bourg et al., 2015; Black et al., 2015). While the thermodynamic properties of mineral dissolution and precipitation reactions are generally pretty well understood, large discrepancies in estimates of mineral reactive surface area exist (Bourg et al., 2015) and mineral reactive surface areas estimates are a major source of uncertainty in reactive transport simulations. Typically, geometric or specific surface areas (SSA) are used as a means of estimating mineral reactive surface area. Geometric surface area approximations assume that all the grains are spherical and of uniform size (Anbeek, 1992; Gunter et al., 2000; Noiriél et al., 2009) where an additional, smaller, grain diameter may be assumed if clay minerals are present (White et al., 2005; Alemu et al., 2011; Beckingham et al., 2016). Specific surface areas, those that account for grain surface roughness, can be obtained by applying a scaling factor to geometric surface areas, through BET method, or by measuring the perimeter of a grain surface (Dogan et al., 2007; Bourg et al., 2015; Beckingham et al., 2016). Specific surface areas of clay minerals can be measured from atomic force microscopy (AFM) and from gas and liquid adsorption where comparisons in Macht et al. (2011) indicated that SSA measured from AFM are larger.

Mineral surface areas can vary by up to seven orders of magnitude, depending on the estimation approach and type of surface area estimated (e.g. geometric, specific, or effective) (Dogan et al, 2007; Bourg et al. 2015; Beckingham et al. 2016; Strehlau et al., 2017; Hegyesi et al., 2017). Specific and geometric surface areas, however, do not reflect porous media effects which may limit access to mineral surfaces where recent studies have suggested effective surface areas that reflect the accessibility of mineral

surfaces may be a more appropriate means of estimating mineral reactive surface area (Beckingham et al., 2017). A new approach was introduced in Landrot et al. (2012) to measure mineral accessible surface area using a multi-scale imaging approach combining 2D SEM imaging and 3D X-ray CT imaging. This effective surface area reflects pore connectivity and grain coatings that may limit access to mineral surfaces and result in mineral accessibilities that differentiate from mineral abundances (Peters, 2009; Waldmann et al., 2014; Beckingham et al., 2017). This approach was used to quantify accessible surface areas in a core sample in Beckingham et al. (2017) and were used to accurately simulate observed dissolution rates from a core-flood dissolution experiment.

While imaging is a powerful means of parameterizing reactive transport simulations, there is little guidance for many of these approaches where variations in technique or image processing approach may largely impact results as has been extensively considered for image thresholding (Wildenschild and Sheppard, 2013; Schlüter et al., 2014; Anovitz and Cole, 2015). In addition, images can often be captured at a wide range of image resolutions, the impact of which is largely unknown. Variations in pore network properties, including porosity, pore and pore-throat size distributions, and pore connectivity, have been observed with varying image resolution (Peng et al. 2012; Shah et al. 2016; Guan et al. 2018). However, the impact of image resolution on measured mineral properties key for reactive transport simulations, including mineral abundance and mineral accessible surface area, remains unknown where variations in these properties will result in discrepancies in the simulated rate and extent of mineral reactions. This work will evaluate the impact of image resolution on measured mineral properties including porosity, mineral abundance, accessibility and accessible surface area, focusing on images with resolutions ranging 0.34 μm to 5.71 μm .

2.2 Materials and methods

2.2.1 Samples and sample preparation

Sandstone samples from the Paluxy formation at the Kemper County power plant, Kemper, Mississippi are used here. These samples were subsampled from whole-core extracted from well MPC 34-1. Samples from the Paluxy formation at depths of 1539 m, 1540 m, 1542 m, 1548 m, 1550 m, 1554 m and 1565 m were analyzed and samples from depths of 1539 m and 1550 m selected for the in depth analysis here. XRD analysis was performed using Bruker D2 Phaser X-Ray Diffractometer in the Department of Geosciences at Auburn University, and data were analyzed using PC-based Datascan software DIFFRAC.EVA with results indicating quartz as the predominant phase. Other mineral species discussed in the following sections were not apparent in the XRD analysis but were observed and identified in SEM BSE images and EDS maps as discussed below.

Bulk samples were sent to Applied Petrographic Services, Inc. (Westmoreland,

Pennsylvania) for thin section preparation. This included impregnating samples with epoxy, sectioning, adhering to glass slides and polishing. To prepare for SEM imaging, a conductive carbon coating was applied to each thin section using EMS 550X Sputter Coating Device at Auburn University.

2.2.2 2D SEM Imaging

2.2.2.1 Image acquisition

Table 2.1 Details of SEM BSE images captured at resolutions ranging from 0.34 μm to 5.71 μm .

Image resolution (μm)	Image size (pixel x pixel)	Image size (mm^2)
0.34	8550 x 5400	5.34
0.98	3000 x 1875	5.40
2.22	1332 x 835	5.48
4.44	670 x 418	5.52
5.71	517 x 322	5.43

Thin sections were imaged using a ZEISS EVO 50VP Scanning Electron Microscope at Auburn University in backscatter electron mode, where a beam intensity of 20 kV and working distance of 8.5 mm were used. BSE images were captured at five different image resolutions (Table 2.1) covering an area of $\sim 5.4 \text{ mm}^2$. For high resolution images, this required capturing a series of individual BSE images and stitching them together using the “Pairwise stitching” plugin in ImageJ. For the 0.34 μm resolution images, for example, nine BSE images were captured and then stitched using ImageJ to generate the 5.34 mm^2 BSE image for further analyses. Lower resolution images that did not require image stitching were manually cropped to the same area of interest using ImageJ where minor variations in image size exist due to human error when cropping. This SEM is also equipped with an EDS detector, which enables elemental analysis of samples and was used to obtain elemental maps of the area of interest. BSE and EDS images were used for image segmentation as well as mineral identification as described below (Sections 2.2.3.1 and 2.2.3.2).

2.2.2.2 Image thresholding

SEM BSE images are grayscale images with pixel intensities and shades ranging from 0 to 255 and black to white, respectively. Pixel intensities in SEM BSE images relate to the average atomic number of the phase where elements with higher atomic number backscatter electrons more strongly (Lloyd, 1987). In these images, epoxy-

filled pores have the lowest intensity and therefore are the darkest in the image and the dominant mineral phase, quartz, appears in gray. Minerals that contain elements with relatively higher atomic numbers, such as K, Ca, and Fe, appear brighter in BSE images.

SEM BSE images were processed here to identify grain and mineral pixels using ImageJ and algorithms developed in MATLAB. Images were first thresholded using a segmentation algorithm developed by Peters (2009) that aims to find the threshold value that minimizes the sum of normalized differentials as given by,

$$\min \left(\frac{1}{N_p} \left| \frac{dN_p}{dI_{p,G}} \right| + \frac{1}{N_{BQ}} \left| \frac{dN_G}{dI_{p,G}} \right| \right) \quad (2)$$

where N_p is the number of pore pixels, N_G is the number of grain pixels, and $I_{p,G}$ is the threshold value of pores and grains. Once the pore threshold value was determined using equation 2, the threshold value was validated by visual inspection and adjusted as needed. The final threshold value was selected as the value that gave the most accurate characterization of pores and grains by visual inspection. Image porosities were then calculated by counting pore and grain pixels using an algorithm developed in MATLAB.

2.2.2.3 Mineral identification

SEM BSE images provide a relative identification of mineral phases. In samples with abundant quartz, it can be helpful to segment mineral pixels into those with intensities higher and lower than quartz, as proposed in Peters (2009) where this segmentation was carried out using the relationship expressed in equation 2. However, identifying the thresholds that differentiate individual mineral phases is challenging and many minerals have intensities close to quartz (e.g. feldspars). Minerals in SEM BSE images can be identified with the additional information provided by elemental SEM EDS maps in conjunction with observations of mineral characteristics where clay minerals, for example, appear distinctly different than aluminosilicates. Here, discrete mineral phases were identified in SEM BSE images using elemental maps, SEM EDS line-scan analyses, and visual observations of mineral characteristics including grain structure and phase distribution. Minerals that are commonly observed in sandstone (e.g. quartz, feldspar, calcite), were identified using SEM EDS elemental maps. Minerals with complex chemical compositions (e.g. smectite/illite) and minerals that might have chemical formula similar to other mineral species (e.g. siderite, muscovite) were identified through EDS line-scans to acquire elemental data and through comparison with SEM BSE images published in existing literature (Welton, 1984). Minerals were first identified in the BSE image with highest resolution 0.34 μm before identifying the mineral phases in the other four images using the same approach. Images with mineral phases indicated by different colors were then created for each resolution.

2.2.2.4 Mineral abundance and accessibility

Mineral abundances and accessibilities were calculated from segmented images depicting discrete mineral phases. Mineral abundances were computed by counting number of pixels of each mineral and dividing by the total number of mineral pixels. Accessible minerals are deemed minerals that are adjacent to the pore space or black pixels. The accessibility of each mineral phase was calculated by counting the number of accessible pixels of each mineral and dividing by the total number of accessible mineral pixels.

2.2.2.5 2D pore connectivity

The mineral accessibility analysis in section 2.2.4 assumes all pore pixels are accessible. However, mineral accessibility can be largely impacted by pore connectivity (Landrot et al., 2012) where pore connectivity at the nano and macro scale needs to be considered as pores may be connected through nanopores in clay minerals (Landrot et al. 2012, Beckingham et al. 2016). Here, smectite is the predominant clay mineral and evaluation of the nature of the connected nanopores in smectite was considered using FIB-SEM imaging in Beckingham et al. (2016). This analysis revealed that smectite contains abundant, well-connected nanoporosity and contributes to the overall pore connectivity (Beckingham et al. 2016). Here, the accessibility of minerals to connected nano and macro pores was considered. Connected porosity was first determined using a method modified from Landrot et al. (2012) and Beckingham et al. (2017) where smectite was assumed to contain well-connected nanopores (Beckingham et al. 2016). In this method, pore pixels at the image edge are first identified before using a burning algorithm to determine connected macro and nano-pores. Connected pore pixels were then counted and the connected porosity of the images with various resolutions calculated.

2.2.3 3D X-ray CT imaging

2.2.3.1 Image acquisition

To prepare for 3D X-ray micro-CT imaging, a 0.5 cm x 0.5 cm x 1 cm cuboid was extracted from the bulk sample. X-ray CT images were captured using NANO-CT-GE V TOME X M 240 at the Research Service Center, Herbert Wertheim College of Engineering, University of Florida. The voxel resolution of captured images is 6.6 μm . A total of 400 cross-sectional slices were extracted from the micro-CT image and cropped into approximate 2.7 mm x 5.3 mm rectangles corresponding to a total area of 5814 mm^2 . Cross-sectional slices were then stacked to reconstruct the 3D micro-CT image of the sample.

2.2.3.2 Image thresholding

Before thresholding the micro-CT image into pores and grains, the grey values

were rescaled to enhance the differences between pores and grains. However, the grey values of the original and enhanced image varied along the length of the cuboid. To correct for this, the 400 cross-sectional images of the cuboid were categorized into 10 groups based on their original brightness and contrast and location in the image sequence. Image subsets were then thresholded independently of each other using the same thresholding procedure as for the BSE images as described in section 2.2.2.2. As needed, manual adjustment of the threshold was performed to improve grain and pore classification. Manual inspection of each image set was performed by comparing the segmented image with the original image to minimize the error introduced by this method. The porosity of the 3D micro-CT image was then calculated by counting pore and grain pixels.

2.2.4 Accessible surface area quantification

2D SEM BSE and 3D X-ray micro-CT images have unique advantages and disadvantages. While 2D SEM images can provide information on mineral identifies and abundances, they cannot reflect the 3D pore connectivity. 3D X-ray micro-CT images capture the 3D pore connectivity but identification of discrete mineral phases in these images remains challenging. It is also difficult to account for nano-pore connectivity in 3D X-ray micro-CT images (Beckingham et al, 2017) since the resolutions are typically low. Here, an approach combining the 2D SEM and 3D X-ray micro-CT images, developed in Landrot et al. 2012, is used to quantify accessible mineral surfaces. This includes analysis of connected porosity and quantification of accessible mineral surface areas in 3D X-ray micro-CT cubes combined with information on mineral accessibility from 2D SEM BSE images.

Pore connectivity and corresponding accessible mineral surface areas are quantified using the 3D X-ray micro-CT image. The 3D X-ray micro-CT image has a total cross-sectional slice area of 5814 mm² where the area of the 2D SEM BSE image analyzed here is only 5.4 mm². To ensure the 3D quantified mineral surface area is comparable to the 2D SEM sample, sub-cubes with a total cross-sectional slice area equivalent to the SEM BSE image were extracted from the larger X-ray micro-CT image. Sub-cubes consist of twelve adjacent 662 μm x 662 μm slices randomly selected and cropped from the 400 cross-sectional slices to create a 3D cube that has the same surface area of the 2D SEM BSE image analyzed. Ten such cubes were created and processed using a MATLAB code modified from Landrot (2012) that uses a burning and marching cube algorithm to identify and quantify the connected surface area in each cube. The porosity of each cube was also calculated to ensure the representativeness of the selected cubes. The average connected surface area of the ten cubes was calculated and multiplied by the accessibility of each non-clay mineral species, determined using the 2D SEM BSE images (Section 2.2.2.4), to get the accessible surface area of each mineral. It should be noted that this method is only valid for non-clay minerals due to the nanoporosity and layered structure of clay minerals.

2.3 Results

2.3.1 SEM Imaging

2.3.1.1 Image acquisition and thresholding

Table 2.2 Calculated porosity of segmented images (Fig. 2.1) for images with different resolutions.

Resolution (μm)	0.34	0.98	2.22	4.44	5.71
Number of pore pixels	1.16E+07	1.41E+06	2.75935	69260	40867
Number of total pixels	4.61E+07	5.62E+06	1.10E+06	277056	164160
Porosity	0.2516	0.2511	0.2500	0.2500	0.2490

Five BSE images captured at resolutions ranging from 0.34 μm to 5.71 μm and the corresponding thresholded images, displaying pores in black and grains in white, are shown in Figure 2.1. The porosity of each image, calculated by counting pore pixels in the segmented image (Figure 1 b,d,f,h,j), is given in Table 2.1. As evident in Table 2.1, the calculated porosity of each segmented image agrees relatively well. While no major variations in porosity are observed, the porosity decreases slightly (25.16% to 24.90%) as image resolution decreases. In addition, the captured images appear blurrier as image resolution decreases, resulting in a loss of some fine mineral features such as surface roughness as shown in Figure 2.2. Moreover, some mineral pixels with low intensity, such as clay minerals in this case, become difficult to distinguish from background/pore pixels due to similarities in pixel intensities (Fig. 2.2).

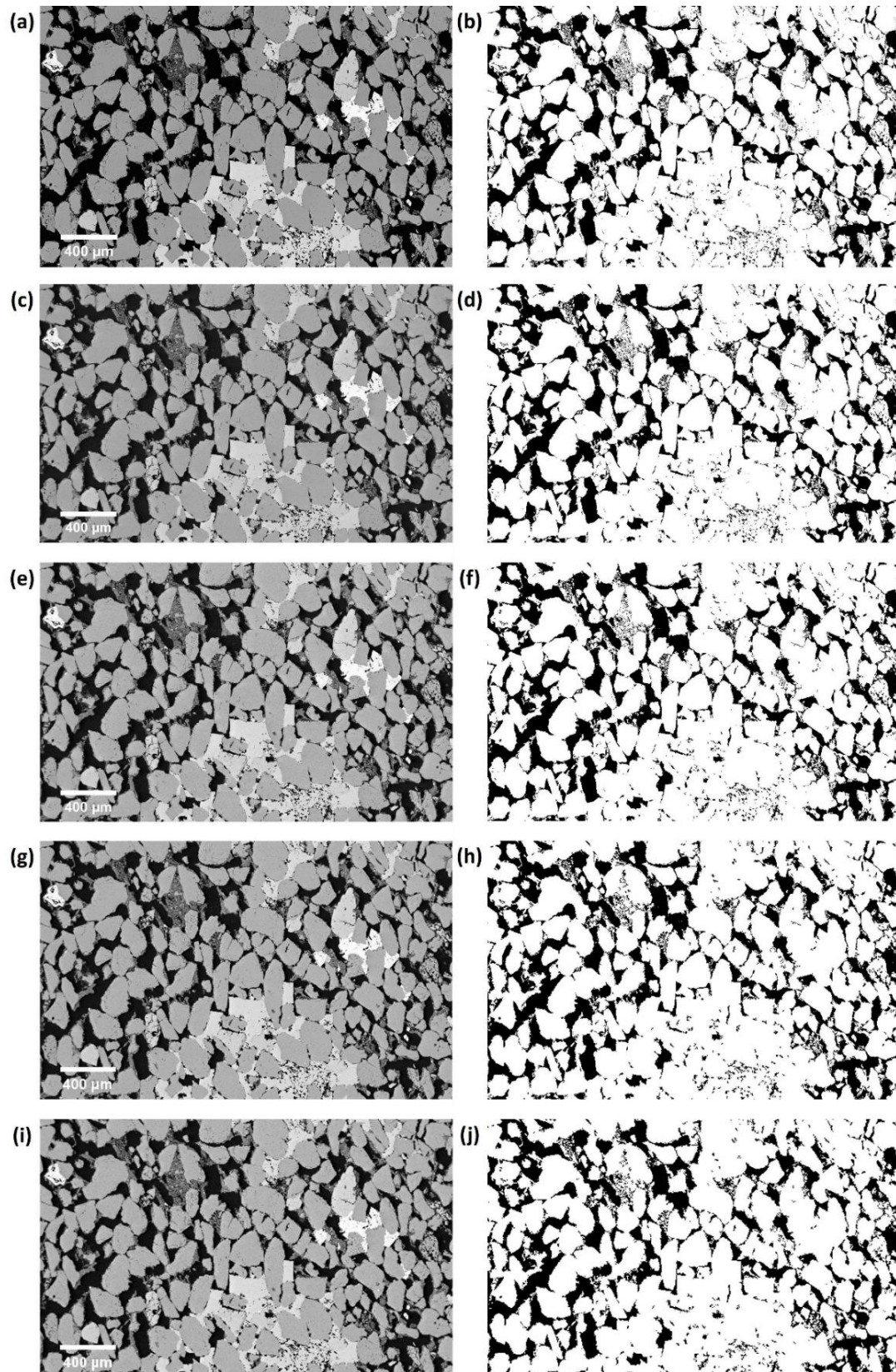


Figure 2. 1. SEM BSE images (left) of a sandstone sample from the Paluxy formation at depth of 5048 ft and the corresponding segmented images (right) depicting grains (white) and pores (black) for images with resolutions (a, b) 0.34 μm , (c, d) 0.98 μm , (e, f) 2.22 μm , (g, h) 4.44 μm , and (i, j) 5.71 μm .

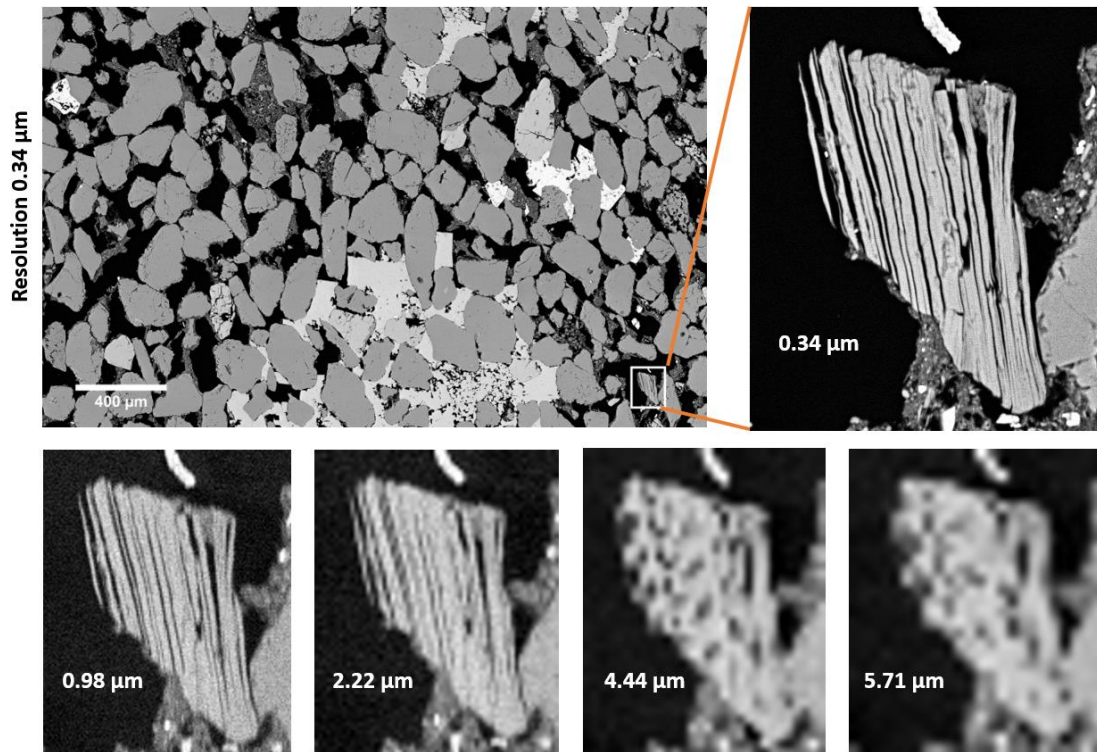


Figure 2. 2. BSE images of a muscovite grain under 5 different image resolutions demonstrating the resulting differences in surface features among the set of images.

2.3.1.2 Mineral identification and quantification

Segmented SEM images, where minerals were identified using EDS elemental maps, quantitative line scans, and by visual observation of mineral grain structures, are shown in Figure 2.3. In these segmented images, each mineral phase is shown in a different color. Initial mineral segmentation by grayscale intensity resulted in some errors in mineral identification that were manually corrected. For example, the cavities on quartz grains were erroneously identified as clay minerals or pores due to a slightly lower grayscale intensity. EDS elemental maps, however, revealed these areas to be topographical in nature and they were manually corrected in the segmented image using ImageJ.

The five mineral phase segmented images with varying resolutions are shown in Figure 2.3. Large discrepancies in phase identification were not observed in these images. However, as image resolution decreases (Fig. 2.3a to Fig. 2.3e), some small features such as the surface roughness of smectite/illite became difficult to capture (Fig. 2.3f to Fig. 2.3j) and the interfaces of phases increasingly difficult to distinguish. For example, distinguishing internal porosity from grain surface features is increasing difficult as resolution decreases, increasing the likeliness of erroneous classification of these features.

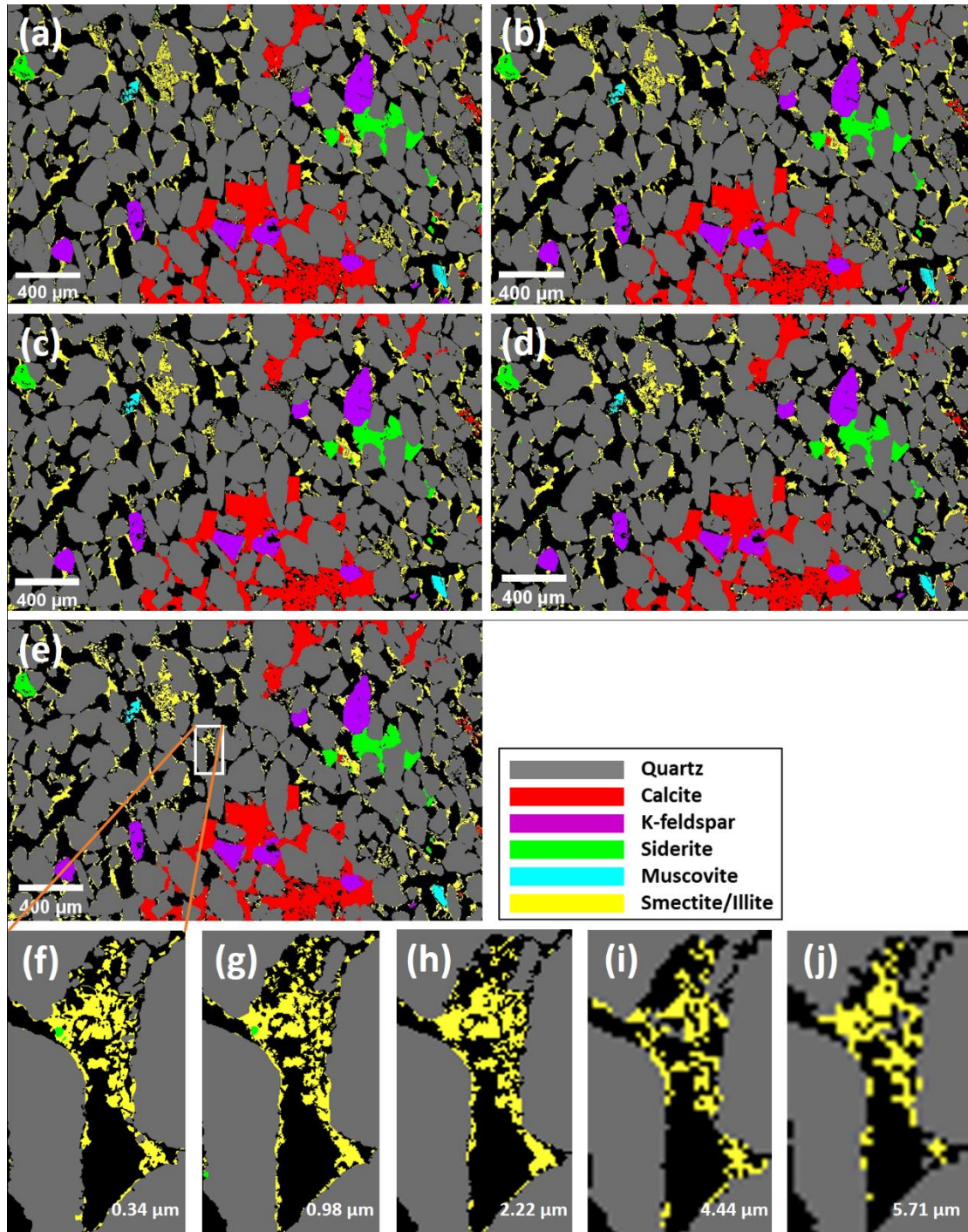


Figure 2. 3. Mineral phase segmented images of a rock sample thin section from the Paluxy formation at depth of 1539 m with image resolutions of (a) 0.34 μm , (b) 0.98 μm , (c) 2.22 μm , (d) 4.44 μm , and (e) 5.71 μm . Subsets (f) – (j) are examples of variations in smectite/illite characterization under image resolutions from 0.34 μm to 5.71 μm . Here, the most dominant phase, quartz, is shown in gray, calcite in red, K-feldspar in purple, siderite in green, smectite/illite in yellow and muscovite in cyan.

Table 2.3 Mineral abundance calculated from BSE segmented images under 5 different resolutions.

Resolution (μm)	Quartz (%)	K-feldspar (%)	Calcite (%)	Smectite/ Illite (%)	Muscovite (%)	Siderite (%)
0.34	76.45	3.50	9.63	8.23	0.31	1.88
0.98	77.14	3.37	9.04	8.32	0.31	1.82
2.22	78.31	3.33	9.00	7.31	0.33	1.73
4.44	77.99	3.34	9.33	7.02	0.30	2.02
5.71	78.74	3.24	8.74	7.26	0.32	1.70

Mineral abundances were calculated for each image by counting discretized mineral pixels in segmented images (Fig. 2.3 a – e) and dividing by the total number of mineral pixels. Calculated abundances for each phase are given in Table 2.3. As evident in Table 2.3, this sample is predominantly quartz (~76.5% of all mineral pixels), with approximately 9.6% calcite, and ~8.2% clay minerals (smectite/illite). In general, with image resolution changing from 0.34 μm to 5.71 μm , the calculated mineral abundance remained stable for muscovite, while abundance of quartz increased slightly from 76.5% to 78.7%, and all other mineral species decreased in abundance, albeit all within ~1%.

3.1.3 2D pore connectivity

The 2D connected porosity was calculated by counting all the pore pixels that are connected through either pore throats or smectite/illite nanopores. Figure 4 shows an example of the 2D connected porosity for the image with 0.34 μm resolution where the mineral segmented map (Fig. 2.4a) was processed to find all the connected pore space (macro-pores and nano-pores) in two dimensions (shown in pink in Fig. 2.4b). As evident in Figure 2.4, while a majority of the pores are connected, there are some unconnected pores, shown in black in Figure 2.4b.

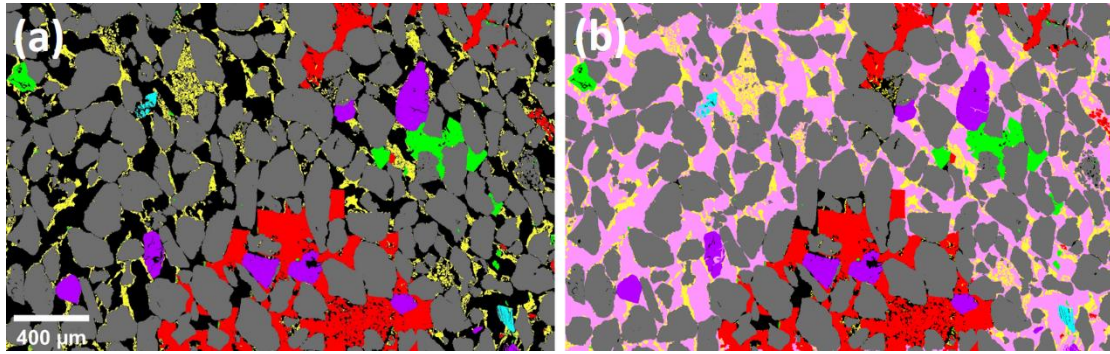


Figure 2. 4. Mineral phase segmented map (0.34 μm resolution) with each mineral mapped in different color (a) and connected porosity map (0.34 μm resolution) depicting the connected pore space in pink (b).

Table 2.4 Connected porosity calculated from mineral phase segmented images for the set of images with different resolutions.

Image resolution (μm)	Total porosity	Connected porosity
0.34	0.2516	0.2338
0.98	0.2511	0.2394
2.22	0.2500	0.2357
4.44	0.2500	0.2469
5.71	0.2490	0.2085

The calculated connected porosity for each of the five images is given in Table 2.5. The overall connected porosity was calculated to be around 0.23, close to total porosity of 0.25 for images with resolution higher than 4.44 μm. When image resolution decreases to 5.71 μm, the connected porosity was 0.21 which is relatively lower than the values calculated from higher resolution images.

3.1.4 Mineral accessibility

Table 2.5 Mineral accessibility calculated from BSE segmented images (Fig. 2.4a) with 5 different resolutions.

Resolution (μm)	Quartz (%)	K-feldspar (%)	Calcite (%)	Smectite/Illite (%)	Muscovite (%)	Siderite (%)
0.34	34.42	2.19	7.44	53.61	1.13	1.20
0.98	33.36	1.42	5.68	58.00	0.68	0.85
2.22	47.67	1.64	6.40	42.62	0.78	0.87
4.44	54.75	2.07	7.83	32.74	0.76	1.84
5.71	59.39	1.76	6.45	30.51	0.64	1.24

Table 2.6 Mineral accessibility calculated from multi-scale connected-porosity images (Fig. 2.4b) with 5 different resolutions.

Resolution (μm)	Quartz (%)	K-feldspar (%)	Calcite (%)	Smectite/Illite (%)	Muscovite (%)	Siderite (%)
0.34	31.96	1.43	1.76	63.05	1.00	0.80
0.98	30.62	0.74	1.24	66.30	0.62	0.47
2.22	45.22	0.95	1.23	51.30	0.79	0.52
4.44	54.99	1.54	1.69	39.27	0.88	1.62
5.71	57.41	0.81	1.24	38.82	0.95	0.78

Accessible mineral pixels are defined here as the pixels that are adjacent to pore pixels (black in Figure 2.4a). The accessibility of each mineral, given in Table 2.5, is calculated as the number of accessible pixels of each mineral divided by total accessible mineral pixels. It should be noted that this only accounts for pore pixels identified in the SEM BSE images and does not account for any nano-pores in clay minerals. As shown in Table 2.5, approximately 34.42% of accessible mineral pixels are quartz pixels, 53.61% are smectite/illite, and 7.44% are calcite as determined from the 0.34 μm resolution image. The accessibilities of other minerals are all less than 3%. With changing image resolution, the mineral accessibility changes where quartz and smectite/illite are most impacted. For image resolutions lower than 1 μm, the accessibility of quartz increased from 34.42% to 59.39% and the accessibility of

smectite/illite decreased from 53.61% to 30.51%. Although the change in the accessibility of muscovite is only around 1%, it actually reduces by ~45% as image resolution decreases. As evident in Figure 2.2, this is because surface features become smoother and even undefined as resolution decreases.

To account for nano- to macro-pore connectivity, pore connectivity through nano-pores in clay minerals (smectite/illite) was considered. The resulting connected porosity is shown in Figure 2.4b (pink pixels) where accessible mineral pixels are defined as the pixels adjacent to the connected pore pixels and are given in Table 2.6. Quartz and smectite/illite remain the most accessible mineral phases. With decreasing image resolution, the accessibility of smectite/illite decreases while the accessibility of quartz increases. Comparing accessibility with and without accounting for pore connectivity (Tables 2.5 and 2.6), it is evident that when nano-pore connectivity was considered the accessibility of smectite/illite increases while the accessibility of other minerals decreases.

In comparison with mineral abundance, mineral accessibility often varies. Quartz is the most abundant phase (%) but does not have the highest accessibility. Smectite/illite has the highest accessibility, comprising over half of the accessible pore/grain interface pixels. This is mainly caused by the fact that smectite/illite occurs as a grain coating or bridging phases, significantly increasing its accessibility, even with relatively low abundance.

2.3.2 3D X-ray CT imaging

2.3.2.1 Image acquisition and thresholding

The X-ray CT image of the core sample is given in Figure 2.5. Pores and grains were segmented through the same method used for 2D imaging and the final segmented image is shown in Figure 2.5b. The porosity of the sample was calculated to be 0.26 by counting the number of pore pixels and dividing by the number of total pixels. This agrees relatively well with the porosity computed from the BSE images (Section 2.3.1.1) of 0.25.

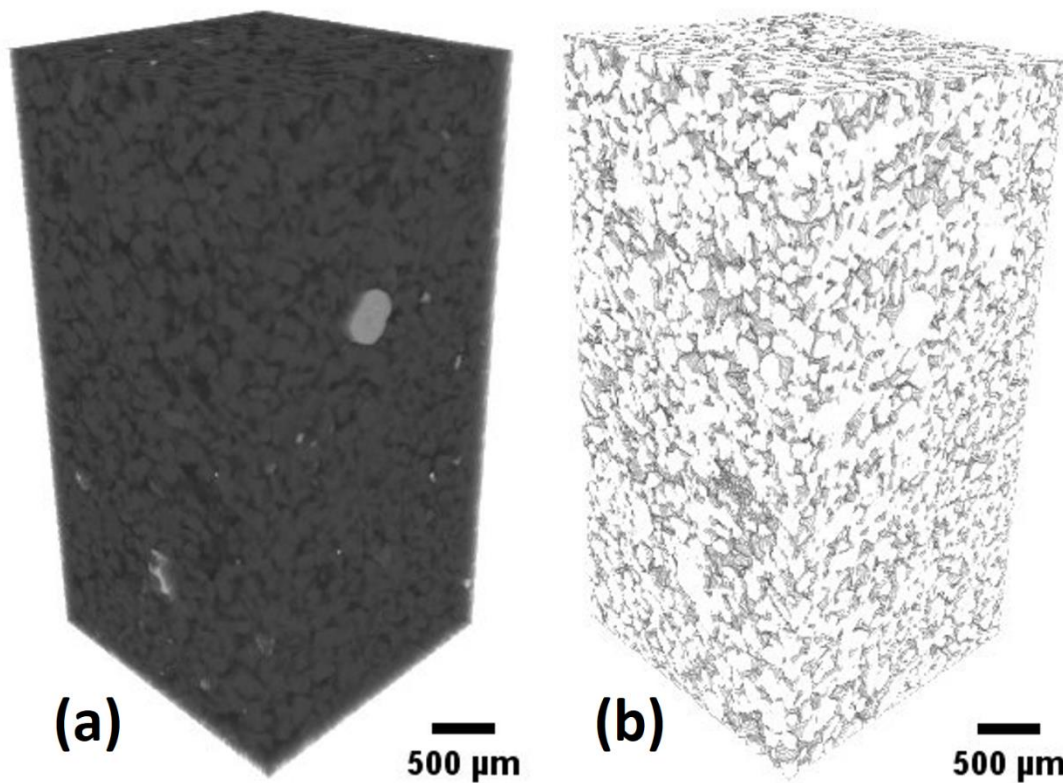


Figure 2. 5. (a) 3D X-ray CT image and (b) thresholded 3D X-ray CT image with pores depicted in black and grains in white.

2.3.2.2 Accessible surface area

Table 2.7 Mineral accessible surface area for non-clay mineral phases as computed from the imaging analysis assuming all the pores are connected.

Image resolution (μm)	Quartz (m^2/g)	K-feldspar (m^2/g)	Calcite (m^2/g)	Siderite (m^2/g)
0.34	1.59E-02	1.02E-03	3.44E-03	5.53E-04
0.98	1.54E-02	6.58E-04	2.63E-03	3.94E-04
2.22	2.21E-02	7.57E-04	2.96E-03	4.01E-04
4.44	2.53E-02	9.58E-04	3.62E-03	8.50E-04
5.71	2.75E-02	8.16E-04	2.98E-03	5.74E-04

The segmented 3D X-ray CT images were used in conjunction with the BSE images to compute mineral accessible surface areas as in Landrot et al., (2012) and Beckingham et al., (2017) as the 2D images are unable to account for the 3D connectivity. To evaluate the 3D pore connectivity in a sample size equivalent to that analyzed in the BSE images, cuboids with the same total slice surface area of the BSE images (5.4 mm^2) were randomly sampled from the 3D X-ray micro-CT image. This corresponded to cuboids of $662 \times 662 \times 80 \mu\text{m}^3$ in volume. The average mineral bulk density was calculated to be 2.66 g/cm^3 by using measured mineral percentages and the density of each mineral phase. The mass of individual cuboids was then calculated to be $1.05 \times 10^{-5} \text{ g}$. The mineral surface area adjacent to the connected pore space of ten randomly selected cuboids was first calculated by identifying the connected surface area using a marching cube and burning algorithm developed in Landrot et al. (2012). The surface area of individual cuboids was then computed by applying a mesh to the identified solid phase and computing the summing the area of each component before dividing by the mass of the mineral phase. The average mineral surface area of the 10 cubes is $0.046 \text{ m}^2/\text{g}$.

Table 2.8 Mineral accessible surface area for non-clay mineral phases as computed from the imaging analysis accounting for nano- to macro- pore connectivity.

Image resolution (μm)	Quartz (m^2/g)	K-feldspar (m^2/g)	Calcite (m^2/g)	Siderite (m^2/g)
0.34	1.48E-02	6.60E-04	8.13E-04	3.72E-04
0.98	1.42E-02	3.43E-04	5.75E-04	2.18E-04
2.22	2.10E-02	4.39E-04	5.67E-04	2.38E-04
4.44	2.54E-02	7.14E-04	7.84E-04	7.47E-04
5.71	2.65E-02	3.74E-04	5.73E-04	3.60E-04

The accessible surface area of each mineral species was calculated by multiplying the average total mineral surface area computed from the 3D cuboids ($0.046 \text{ m}^2/\text{g}$) by the accessibility of each mineral species (Tables 2.5 and 2.6). As the area of interest in the 2D images is the same for all resolutions, the connected surface area determined from the 3D X-ray micro-CT images is the same for all five images but the corresponding accessible surface areas vary due to differences in computed accessibility. It should be noted that this approach does not account for the connectivity of clay minerals in the X-ray micro-CT image and additionally cannot be used to determine the surface areas for clay minerals.

The accessible mineral surface areas for non-clay minerals determined using the imaging approach are given in Table 2.7 and 2.8. These surface area values follow the same trend as observed for mineral accessibility. For images with resolutions lower than $1 \mu\text{m}$, the calculated accessible surface area of quartz increases as resolution decreases and the accessible surface area of smectite/illite decreases.

2.4. Discussion

Mineral abundance remained relatively consistent with variations in image resolution. Fluctuations in abundances were within 2.5% for all mineral species, indicating image resolution does not have significant impact on mineral phase segmentation for images with resolutions ranging from $0.34 \mu\text{m}$ to $5.71 \mu\text{m}$. However, the relative percent change for minerals that occur as small grains or with small scale features including micro-pores, such as muscovite and smectite/illite, are impacted more than minerals that occur as large grains with little or no small scale features such as quartz and calcite. These small-scale features are not captured well with lower image resolutions which increases segmentation difficulties. For example, the surface roughness of smectite/illite can be visually observed under resolutions of 0.34 and 0.98

μm , however, it cannot be captured under lower resolutions (Fig. 2.3f to Fig. 2.3j). In addition, the pores within muscovite are easily distinguishable in the $0.34 \mu\text{m}$ resolution images (Fig. 2.2) but become blurry when the image resolution decreases to $2.22 \mu\text{m}$. At lower resolutions, these features can be erroneously recognized as grain pixels or clay coatings. While the impact of these variations are minimal for the sample considered here, they would be significant if the abundance of minerals like muscovite and smectite/illite is relatively high in the sample and would result in larger variations and imprecisions in calculated abundances for these mineral species. For simulated geochemical reactions, imprecision of mineral phase segmentation caused by lack of image resolution may result in misinterpretation of the long term evolution of permeability since many minerals with small-scale features can largely contribute to permeability (Armitage et al., 2016; Bourg et al., 2017).

Identifying grain boundaries between minerals with similar BSE intensities is additionally challenging in low resolution images. For example, K-feldspar and calcite in the BSE images analyzed here appear similarly in terms of grayscale intensity. In the low-resolution images, it is difficult to distinguish them as separate phases and identify the grain boundaries, even with the help of EDS elemental maps. Discrepancies may occur in mineral identification in low-resolution images without additional high-resolution analysis of phase distributions.

In terms of calculated mineral accessibilities, among all the mineral pixels that are accessible to pore space, over 90% of them were quartz and smectite/illite. Clay minerals (e.g. smectite) are typically highly accessible and have relatively low greyscale intensity in BSE images making them challenging to segment. Even in the $0.98 \mu\text{m}$ resolution image, the pore space at grain edges and the pore/clay interface is difficult to distinguish. This may result in misclassification of some pore/grain boundary pixels. Here, the accessibility of smectite/illite decreases as image resolution decreases from 0.98 to $5.71 \mu\text{m}$ while the accessibility of quartz increases. This is most likely due to the challenge capturing clay coatings at a low resolution and loss of small-scale features such as surface roughness in images with resolution lower than $0.98 \mu\text{m}$. Clay coatings also impacted the calculated mineral accessibility of less abundant phases where even small imprecisions of clay pixel classification can result in large variation in calculated accessibility. This was the case for K-feldspar and calcite, whose accessibilities are much smaller than quartz and smectite. These variations are most likely caused by human error when segmenting clay coatings. In general, the resulting accessibility will be overestimated if some of the clay coatings are neglected during processing, and it will be underestimated if some interface pixels or grain pixels are erroneously classified as clay coatings. Erroneous classification of clay coatings is more likely to occur in images with lower resolutions where clay coatings are only one or two pixels thick. This may result in significant variation in mineral accessibility where these challenges resulted in variations of measured accessibilities for all images with resolutions lower than $0.34 \mu\text{m}$.

Unlike mineral abundance, the mineral accessible surface area is impacted by mineral surface roughness. While quantifying mineral abundance, as long as the mineral grains are visible and differentiable from other grains, with proper processing, the calculated abundances will not largely be impacted by image resolution. However, for mineral species with rough surfaces and structures with small scale features that significantly increase mineral surface areas, image resolution may have a large impact on calculated accessible surface area. Mineral surface features and surface roughness may be captured well at high resolutions but underestimated at lower resolutions. For example, minerals with serrated surfaces (e.g. muscovite) tend to have a higher surface area than minerals with smooth surfaces (e.g. quartz, calcite). In lower resolution images, however, the surface features will be smoothed resulting in an underestimation of surface area. As these calculations depend on the calculated mineral accessibility, the challenges in identifying pore-grain boundaries discussed above impact the computed accessible surface areas as well. The impact of image resolution on measured mineral accessible surface area would likely become more significant if these mineral species are highly abundant and have clay coatings. When utilized to inform reactive transport simulations, these variations in surface area values calculated from lower resolution images would result in differences in simulated reaction rates and potentially lead to very different results.

Pore connectivity can also largely impact the accessibility of mineral surfaces. Based on the results given above, the total porosity calculated from all 5 images with different resolutions remains consistent at ~ 0.25 . From the pore connectivity analysis, it was observed that not all the pore spaces are connected in the area studied here and the calculated connected porosity is around 0.24. Overall, the connected porosity remained consistent with decreasing image resolution. However, when resolution decreased from $4.44\ \mu\text{m}$ to $5.71\ \mu\text{m}$, the calculated connected porosity decreased from 0.24 to 0.21. Therefore, lower image resolutions might result in an underestimation of connected porosity. The analysis here considered connectivity through nanopores, assuming smectite nanopores were well connected (Beckingham et al., 2017). As image resolution decreases, distinguishing clay minerals that may control pore connectivity becomes increasingly challenging. Misidentification of clay phases will impact computed connected surface area where these impacts will be larger for samples with higher fractions of clay minerals that contribute to the overall pore connectivity.

Conclusions

This work aims to enhance understanding of the impact of image resolution on quantification of sample properties important for reactive transport simulation including porosity, mineral abundance, and mineral accessible surface area. Here, these properties were determined for a sandstone sample from 2D SEM images collected at 5 different image resolutions, 0.34, 0.98, 2.22, 4.44 and $5.71\ \mu\text{m}$. For the sample and resolutions considered, there was not a large difference in the porosity and abundance

of mineral phases such that quantification of these parameters from even the coarsest resolution image here would be feasible. This may, however, not be true for samples with a higher abundance of minerals with layered structures or micro-pores where reductions in resolution may largely impact porosity and abundance calculations. In addition, reductions in image resolution can increase challenges in mineral identification and segmentation, particularly for clay minerals and minerals with similar average atomic number that are present in the same area as EDS data is inherently noisy.

The overall impact of image resolution on measured mineral accessibility and accessible surface area was quite evident. As image resolution decreases to below 0.98 μm , where many small-scale features including micro-pores, surface roughness, and layered structures are difficult or even impossible to capture, the accessibilities of such mineral species (e.g. smectite/illite, muscovite) decrease while the accessibility of quartz increases. This, in turn, results in an overestimation of the accessible surface area for quartz. The quantification of mineral surface area of the dominant mineral phase would be impacted most when clay minerals are present as coatings on its surface. As the clay fraction increases, imprecisions in the computed mineral accessibilities are likely to increase due to challenging in segmenting pore/grain/clay pixels with decreasing image resolution. For samples with little to no clay minerals, lower resolution images may be able to provide accurate estimates of accessible surface area but higher resolution images are required for samples with more abundant clay minerals and clay coatings.

While higher resolution images are generally preferred, they have additional time and computational costs to consider. Depending on the sample characteristics, lower resolution images may be sufficient to quantify mineral abundances, so long as grains and coatings can be easily distinguished. When quantifying mineral accessibility, higher resolutions are preferred ($< 0.98 \mu\text{m}$) for the sample considered here that had 4-5 μm thick clay coatings on grain surfaces. For samples with little to no clay minerals, lower resolutions may provide adequate estimates of mineral accessibilities and thus mineral accessible surface areas, applying these values in geochemical reaction simulations should yield results that agree relatively well with the case where high resolution images are used. Samples with higher fractions of clay minerals and phases with small scale features (e.g. muscovite) will require high resolution images with resolutions higher than the dominant small-scale features (e.g. $< 0.98 \mu\text{m}$) for more accurate estimates of mineral accessibility and accessible surface area. Using lower image resolutions when clay minerals are abundant might result in many misinterpretations of mineral phases in small pores and pore-throat regions. This could largely impact the simulated reaction rates and long term permeability evolution, for example, when using images to inform reactive transport simulations.

Acknowledgement

The “Establishing an Early CO₂ Storage Complex in Kemper, MS” project is funded by the U.S. Department of Energy’s National Energy Technology Laboratory and cost-sharing partners.

Reference

1. Aagaard, P. and Helgeson, H.C., 1982. Thermodynamic and kinetic constraints on reaction rates among minerals and aqueous solutions; I, Theoretical considerations. *American journal of Science*, 282(3), pp.237-285.
2. Alemu, B.L., Aagaard, P., Munz, I.A. and Skurtveit, E., 2011. Caprock interaction with CO₂: A laboratory study of reactivity of shale with supercritical CO₂ and brine. *Applied Geochemistry*, 26(12), pp.1975-1989.
3. Al-Khulaifi, Y., Lin, Q., Blunt, M.J. and Bijeljic, B., 2017. Reaction rates in chemically heterogeneous rock: Coupled impact of structure and flow properties studied by X-ray microtomography. *Environmental Science & Technology*, 51(7), pp.4108-4116.
4. Anbeek, C., 1992. Surface roughness of minerals and implications for dissolution studies. *Geochimica et Cosmochimica Acta*, 56(4), pp.1461-1469.
5. Anovitz, L.M. and Cole, D.R., 2015. Characterization and analysis of porosity and pore structures. *Reviews in Mineralogy and geochemistry*, 80(1), pp.61-164.
6. Apul, D.S., Gardner, K.H. and Eighmy, T.T., 2007. Modeling hydrology and reactive transport in roads: The effect of cracks, the edge, and contaminant properties. *Waste management*, 27(10), pp.1465-1475.
7. Armitage, P.J., Worden, R.H., Faulkner, D.R., Butcher, A.R. and Espie, A.A., 2016. Permeability of the Mercia Mudstone: suitability as caprock to carbon capture and storage sites. *Geofluids*, 16(1), pp.26-42.
8. Atchley, A.L., Navarre-Sitchler, A.K. and Maxwell, R.M., 2014. The effects of physical and geochemical heterogeneities on hydro-geochemical transport and effective reaction rates. *Journal of contaminant hydrology*, 165, pp.53-64.
9. Audigane, P., Gaus, I., Czernichowski-Lauriol, I., Pruess, K. and Xu, T., 2007. Two-dimensional reactive transport modeling of CO₂ injection in a saline aquifer at the Sleipner site, North Sea. *American journal of science*, 307(7), pp.974-1008.
10. Bashtani, F., Taheri, S. and Kantzas, A., 2018. Scale up of pore-scale transport properties from micro to macro scale; network modelling approach. *Journal of Petroleum Science and Engineering*, 170, pp.541-562.
11. Beckingham, L.E., Peters, C.A., Um, W., Jones, K.W. and Lindquist, W.B., 2013. 2D and 3D imaging resolution trade-offs in quantifying pore throats for prediction of permeability. *Advances in Water Resources*, 62, pp.1-12.
12. Beckingham, L.E., Mitnick, E.H., Steefel, C.I., Zhang, S., Voltolini, M., Swift, A.M., Yang, L., Cole, D.R., Sheets, J.M., Ajo-Franklin, J.B. and DePaolo, D.J., 2016. Evaluation of mineral reactive surface area estimates for prediction of

- reactivity of a multi-mineral sediment. *Geochimica et Cosmochimica Acta*, 188, pp.310-329.
13. Beckingham, L.E., Steefel, C.I., Swift, A.M., Voltolini, M., Yang, L., Anovitz, L.M., Sheets, J.M., Cole, D.R., Kneafsey, T.J., Mitnick, E.H. and Zhang, S., 2017. Evaluation of accessible mineral surface areas for improved prediction of mineral reaction rates in porous media. *Geochimica et Cosmochimica Acta*, 205, pp.31-49.
 14. Berrezueta, E. and Kovacs, T., 2017. Application of optical image analysis to the assessment of pore space evolution after CO₂ injection in sandstones. A case study. *Journal of Petroleum Science and Engineering*, 159, pp.679-690.
 15. Black, J.R., Carroll, S.A. and Haese, R.R., 2015. Rates of mineral dissolution under CO₂ storage conditions. *Chemical Geology*, 399, pp.134-144.
 16. Bourg, I.C., Beckingham, L.E. and DePaolo, D.J., 2015. The nanoscale basis of CO₂ trapping for geologic storage. *Environmental science & technology*, 49(17), pp.10265-10284.
 17. Bourg, I.C. and Ajo-Franklin, J.B., 2017. Clay, water, and salt: controls on the permeability of fine-grained sedimentary rocks. *Accounts of chemical research*, 50(9), pp.2067-2074.
 18. Bultreys, T., De Boever, W. and Cnudde, V., 2016. Imaging and image-based fluid transport modeling at the pore scale in geological materials: A practical introduction to the current state-of-the-art. *Earth-Science Reviews*, 155, pp.93-128.
 19. Dogan, M., Dogan, A.U., Yesilyurt, F., Alaygut, D., Buckner, I. and Wurster, D.E., 2007. Baseline studies of the Clay Minerals Society special clays: specific surface area by the Brunauer Emmett Teller (BET) method. *Clays and clay minerals*, 55(5), pp.534-541.
 20. Ellis, B.R. and Peters, C.A., 2016. 3D Mapping of calcite and a demonstration of its relevance to permeability evolution in reactive fractures. *Advances in water resources*, 95, pp.246-253.
 21. Essaid, H.I., Bekins, B.A. and Cozzarelli, I.M., 2015. Organic contaminant transport and fate in the subsurface: Evolution of knowledge and understanding. *Water Resources Research*, 51(7), pp.4861-4902.
 22. Gaus, I., Azaroual, M. and Czernichowski-Lauriol, I., 2005. Reactive transport modelling of the impact of CO₂ injection on the clayey cap rock at Sleipner (North Sea). *Chemical Geology*, 217(3-4), pp.319-337.
 23. Gaus, I., 2010. Role and impact of CO₂-rock interactions during CO₂ storage in sedimentary rocks. *International journal of greenhouse gas control*, 4(1), pp.73-89.
 24. Guan, K.M., Nazarova, M., Guo, B., Tchelepi, H., Kavscek, A.R. and Creux, P., 2018. Effects of Image Resolution on Sandstone Porosity and Permeability as Obtained from X-Ray Microscopy. *Transport in Porous Media*, pp.1-13.
 25. Gunter, W.D., Perkins, E.H. and Hutcheon, I., 2000. Aquifer disposal of acid gases: modelling of water-rock reactions for trapping of acid wastes. *Applied geochemistry*, 15(8), pp.1085-1095.
 26. Harder, H., 1972. The role of magnesium in the formation of smectite

- minerals. *Chemical Geology*, 10(1), pp.31-39.
27. Hegyesi, N., Vad, R.T. and Pukánszky, B., 2017. Determination of the specific surface area of layered silicates by methylene blue adsorption: The role of structure, pH and layer charge. *Applied Clay Science*, 146, pp.50-55.
 28. Hommel, J., Coltman, E. and Class, H., 2018. Porosity–Permeability Relations for Evolving Pore Space: A Review with a Focus on (Bio-) geochemically Altered Porous Media. *Transport in Porous Media*, pp.1-41.
 29. Knauss, K.G., Johnson, J.W. and Steefel, C.I., 2005. Evaluation of the impact of CO₂, co-contaminant gas, aqueous fluid and reservoir rock interactions on the geologic sequestration of CO₂. *Chemical geology*, 217(3-4), pp.339-350.
 30. Lamy-Chappuis, B., Yardley, B.W., He, S., Zu, Y. and Xie, J., 2018. A test of the effectiveness of pore scale fluid flow simulations and constitutive equations for modelling the effects of mineral dissolution on rock permeability. *Chemical Geology*, 483, pp.501-510.
 31. Lasaga, A.C., 1981. Transition state theory. *Rev. Mineral.; (United States)*, 8.
 32. Lasaga, A.C., 1984. Chemical kinetics of water, A. interactions. *Journal of geophysical research: solid earth*, 89(B6), pp.4009-4025.
 33. Li, L., Peters, C.A. and Celia, M.A., 2006. Upscaling geochemical reaction rates using pore-scale network modeling. *Advances in water resources*, 29(9), pp.1351-1370.
 34. Liu, C., Liu, Y., Kerisit, S. and Zachara, J., 2015. Pore-scale process coupling and effective surface reaction rates in heterogeneous subsurface materials. *Reviews in Mineralogy and Geochemistry*, 80(1), pp.191-216.
 35. Liu, M., Shabaninejad, M. and Mostaghimi, P., 2018. Predictions of permeability, surface area and average dissolution rate during reactive transport in multi-mineral rocks. *Journal of Petroleum Science and Engineering*.
 36. Lloyd, G.E., 1987. Atomic number and crystallographic contrast images with the SEM: a review of backscattered electron techniques. *Mineralogical Magazine*, 51(359), pp.3-19.
 37. Macht, F., Eusterhues, K., Pronk, G.J. and Totsche, K.U., 2011. Specific surface area of clay minerals: Comparison between atomic force microscopy measurements and bulk-gas (N₂) and-liquid (EGME) adsorption methods. *Applied Clay Science*, 53(1), pp.20-26.
 38. Martinez, B.C., DeJong, J.T. and Ginn, T.R., 2014. Bio-geochemical reactive transport modeling of microbial induced calcite precipitation to predict the treatment of sand in one-dimensional flow. *Computers and Geotechnics*, 58, pp.1-13.
 39. Min, T., Gao, Y., Chen, L., Kang, Q. and Tao, W.W., 2016. Changes in porosity, permeability and surface area during rock dissolution: Effects of mineralogical heterogeneity. *International Journal of Heat and Mass Transfer*, 103, pp.900-913.
 40. Navarre-Sitchler, A., Steefel, C.I., Sak, P.B. and Brantley, S.L., 2011. A reactive-transport model for weathering rind formation on basalt. *Geochimica et*

- Cosmochimica Acta*, 75(23), pp.7644-7667.
41. Navarre-Sitchler, A. and Jung, H., 2017. Complex Coupling of Fluid Transport and Geochemical Reaction Rates: Insights from Reactive Transport Models. *Procedia Earth and Planetary Science*, 17, pp.5-8.
 42. Ng, G.H.C., Bekins, B.A., Cozzarelli, I.M., Baedeker, M.J., Bennett, P.C., Amos, R.T. and Herkelrath, W.N., 2015. Reactive transport modeling of geochemical controls on secondary water quality impacts at a crude oil spill site near Bemidji, MN. *Water Resources Research*, 51(6), pp.4156-4183.
 43. Noiriel, C., Luquot, L., Madé, B., Raimbault, L., Gouze, P. and Van Der Lee, J., 2009. Changes in reactive surface area during limestone dissolution: An experimental and modelling study. *Chemical Geology*, 265(1-2), pp.160-170.
 44. O'Connell, K. and Regalbuto, J.R., 2015. High sensitivity silicon slit detectors for 1 nm powder XRD size detection limit. *Catalysis Letters*, 145(3), pp.777-783.
 45. Peng, S., Hu, Q., Dultz, S. and Zhang, M., 2012. Using X-ray computed tomography in pore structure characterization for a Berea sandstone: Resolution effect. *Journal of Hydrology*, 472, pp.254-261.
 46. Peters, C.A., 2009. Accessibilities of reactive minerals in consolidated sedimentary rock: An imaging study of three sandstones. *Chemical Geology*, 265(1-2), pp.198-208.
 47. Prikryl, J., Jha, D., Stefánsson, A. and Stipp, S., 2017. Mineral dissolution in porous media: An experimental and modeling study on kinetics, porosity and surface area evolution. *Applied Geochemistry*, 87, pp.57-70.
 48. Schlüter, S., Sheppard, A., Brown, K. and Wildenschild, D., 2014. Image processing of multiphase images obtained via Xenschmicrotomography: a review. *Water Resources Research*, 50(4), pp.3615-3639.
 49. Shah, S.M., Gray, F., Crawshaw, J.P. and Boek, E.S., 2016. Micro-computed tomography pore-scale study of flow in porous media: Effect of voxel resolution. *Advances in water resources*, 95, pp.276-287.
 50. Steefel, C.I., Appelo, C.A.J., Arora, B., Jacques, D., Kalbacher, T., Kolditz, O., Lagneau, V., Lichtner, P.C., Mayer, K.U., Meeussen, J.C.L. and Molins, S., 2015. Reactive transport codes for subsurface environmental simulation. *Computational Geosciences*, 19(3), pp.445-478.
 51. Strehlau, J.H., Toner, B.M., Arnold, W.A. and Penn, R.L., 2017. Accessible reactive surface area and abiotic redox reactivity of iron oxyhydroxides in acidic brines. *Geochimica et Cosmochimica Acta*, 197, pp.345-355.
 52. Tutolo, B.M., Luhmann, A.J., Kong, X.Z., Saar, M.O. and Seyfried, W.E., 2015. CO₂ sequestration in feldspar-rich sandstone: coupled evolution of fluid chemistry, mineral reaction rates, and hydrogeochemical properties. *Geochimica et Cosmochimica Acta*, 160, pp.132-154.
 53. Vilcáez, J., Morad, S. and Shikazono, N., 2017. Pore-scale simulation of transport properties of carbonate rocks using FIB-SEM 3D microstructure: Implications for field scale solute transport simulations. *Journal of Natural Gas Science and*

- Engineering*, 42, pp.13-22.
54. Waldmann, S., Busch, A., van Ojik, K. and Gaupp, R., 2014. Importance of mineral surface areas in Rotliegend sandstones for modeling CO₂–water–rock interactions. *Chemical Geology*, 378, pp.89-109.
 55. Welton, J.E., 1984. SEM petrology atlas.
 56. White, S.P., Allis, R.G., Moore, J., Chidsey, T., Morgan, C., Gwynn, W. and Adams, M., 2005. Simulation of reactive transport of injected CO₂ on the Colorado Plateau, Utah, USA. *Chemical geology*, 217(3-4), pp.387-405.
 57. Wildenschild, D. and Sheppard, A.P., 2013. X-ray imaging and analysis techniques for quantifying pore-scale structure and processes in subsurface porous medium systems. *Advances in Water Resources*, 51, pp.217-246.
 58. Xiong, Q., Baychev, T.G. and Jivkov, A.P., 2016. Review of pore network modelling of porous media: experimental characterisations, network constructions and applications to reactive transport. *Journal of contaminant hydrology*, 192, pp.101-117.
 59. Xu, T., Kharaka, Y.K., Doughty, C., Freifeld, B.M. and Daley, T.M., 2010. Reactive transport modeling to study changes in water chemistry induced by CO₂ injection at the Frio-I Brine Pilot. *Chemical Geology*, 271(3-4), pp.153-164.
 60. Yabusaki, S.B., Fang, Y., Williams, K.H., Murray, C.J., Ward, A.L., Dayvault, R.D., Waichler, S.R., Newcomer, D.R., Spane, F.A. and Long, P.E., 2011. Variably saturated flow and multicomponent biogeochemical reactive transport modeling of a uranium bioremediation field experiment. *Journal of contaminant hydrology*, 126(3-4), pp.271-290.

Chapter 3. The impact of mineral reactive surface area variation on simulated mineral reactions and reaction rates

Fanqi Qin, Lauren E. Beckingham

Department of Civil and Environmental Engineering, Auburn University, AL, 36849

Published in Applied Geochemistry, 124, p.104852.

Abstract

Reactive transport modeling is an essential tool to simulate complex geochemical reactions in porous media that can impact formation properties including porosity and permeability. However, simulating these reactions is challenging due to uncertainties in model parameters, particularly mineral surface areas. Imaging has emerged as a powerful means of estimating model parameters including porosity and mineral abundance, accessibility and accessible surface area. However, these parameters, particularly mineral accessible surface area, vary with image resolution. This work aims to enhance understanding of the impact of image resolution and other means of estimating mineral reactive surface area on simulated mineral reactions and reaction rates. Mineral surface areas calculated from images with resolutions of 0.34 μm and 5.71 μm were used to simulate mineral reactions in the context of geologic CO_2 sequestration in the Paluxy formation at the continuum scale. Additional simulations were carried out using BET surface areas collected from the literature and geometric surface areas. Simulations were run for 7300 days and mineral volume fractions and effluent ion concentrations tracked and compared. Variations in mineral surface areas measured from images are within 1 order of magnitude and yield similar simulation results, indicating the impact of image resolution on simulated reactions and reaction rates is minimum for the resolutions and sample considered. In comparison, surface areas obtained from BET and geometric approaches are 1-5 orders of magnitude higher than image-obtained surface areas and result in greater simulated reaction rates and extents. Minerals with high reaction rates (calcite and siderite) are most impacted by surface area values at short times where simulated mineral volume fractions at longer times agree relatively well, even for simulations with several orders of magnitude variation in surface area. Phases with lower reaction rates, such as K-feldspar and muscovite, are predominantly impacted over longer times where variations in surface areas impact reaction extents and porosity evolution.

3.1. Introduction

Reactive transport modeling has been used extensively to enhance understanding of geochemical reactions and transport phenomena happening in a wide variety of surface and subsurface systems (Steefel et al., 2005, 2013; Pallud et al., 2007; Boana et al., 2014; Li et al., 2017; Steefel, 2018; Maher and Navarre-Sitchler, 2019). For example, reactive transport simulations have been used to enhance the understanding

of the fate of contaminants in porous media (Sen et al., 2006; Apul et al., 2007; Xu et al., 2010; Essaid et al., 2015; Schmidt et al., 2019), to evaluate CO₂-induced dissolution and precipitation reactions and corresponding porosity and permeability evolution in subsurface environments (White et al., 2005; Audigane et al., 2007; Bacon et al., 2009; Meakin et al., 2009; Aradóttir et al., 2012; Nogues et al., 2013; Connell et al., 2015; Deng et al., 2015; Ng et al., 2015; Steefel et al., 2015; Navarre-Sitchler et al., 2011 and 2017; Bo Guo et al., 2018; Liu et al., 2019; Miao et al., 2019; Schmidt et al., 2019; Elkady and Kocscek, 2020), and to simulate biogeochemical process such as uranium bioremediation (Scheibe et al., 2009; Yabusaki et al., 2011; Martinez et al., 2014; Grandclerc et al., 2018; Shultz et al., 2018; la Cecilia et al., 2019). Models have the advantage of being able simulate the evolution of a system beyond laboratory time scales where models are developed based on experimental systems and validated with experimental observations (Martens et al., 2012; Salehikhoo et al., 2013; Beckingham et al., 2017).

While reactive transport models are widely used, simulating mineral reactions is challenging not only due to the complexity of the reactions, but also uncertainties in estimating model parameters. In addition, changes in mineral porosity, permeability and reactive surface may occur as reactions progress (Gouze and Luquot, 2011; Qajar, 2012; Qajar and Arns, 2016; Beckingham et al., 2017; Yang et al., 2018; Altree-Williams et al., 2019), which could impact the modeling results. Mineral reaction rates are commonly estimated using a rate law based on transition state theory (TST) (Lasaga, 1981, 1984; Aagaard and Helgeson, 1982) where the reaction rate is given by,

$$R_m = A_m k_m [f \Delta G_r] \quad (1)$$

where A_m is mineral reactive surface area, k_m is mineral rate constant, and $f \Delta G_r$ is the thermodynamic driving force for the reaction (Steeff et al., 2015). While the thermodynamic aspects of mineral reactions are generally well understood, difficulties exist in estimating parameters for mineral nucleation and growth, rate constants in non-ideal conditions including high temperatures and pressures, and mineral reactive surface area (SA) (Hellevang et al., 2013; Black et al., 2015; Bourg et al., 2015). These variations may result in differences in simulated results. Estimated rate constants typically vary by one order of magnitude (Black et al., 2015), whereas variations in reported mineral surface area values span several orders of magnitude (Black et al., 2015; Bourg et al., 2015).

Mineral surface areas are typically measured in the laboratory or estimated based on geometry. In the laboratory, mineral specific surface area is often measured using the Brunauer–Emmett–Teller (BET) adsorption method (Brunauer et al., 1938). Surface areas estimated based on a geometry approximation typically assume mineral grains are smooth, spherical, and of a uniform size (Anbeek, 1992; Gunter et al., 2000; Noiriél et al., 2009). When clay minerals are present, an additional smaller grain size might be assumed (White et al., 2005; Alemu et al., 2011; Beckingham et al., 2016). These

surface areas may or may not be additionally adjusted by roughness and scaling factors varying one to three orders of magnitude to account for surface roughness and variations in reactive site density (Bourg et al. 2015).

Imaging has emerged as powerful tool to quantify mineral properties including mineral abundance, mineral accessibility and mineral accessible surface area (defined in section 2.2.2.1) (Peters, 2009; Landrot et al. 2012; Beckingham et al., 2016 and 2017; Qin and Beckingham, 2019). In this approach, images of mineral thin sections captured using scanning electron microscopy (SEM) under backscatter electron (BSE) mode are segmented into discrete mineral phases utilizing energy dispersive X-ray spectroscopy (EDS) elemental maps. Mineral accessibility is calculated from 2D BSE images by first identifying connected porosity and then corresponding adjacent mineral surfaces (Beckingham et al., 2017, Qin and Beckingham, 2019). This is then combined with 3D X-ray computed tomography (CT) images to calculate pore connectivity in three dimensions and used to infer three-dimensional mineral accessible surface areas (Landrot et al. 2012, Beckingham et al., 2017, Qin and Beckingham, 2019). The required images can be captured over a wide range of resolutions where the impact of image resolution on the quantification of mineral abundance and mineral accessible surface area was assessed in Qin and Beckingham (2019). This analysis revealed mineral volume fractions calculated for a sandstone sample using images with resolutions at 0.34 μm to 5.71 μm agreed relatively well and mineral accessible surface areas varied up to 1 order of magnitude (Qin and Beckingham, 2019). Image-obtained accessible surface areas of calcite, siderite and K-feldspar decreased with decreasing resolution while the accessible surface area of quartz increased with decreasing image resolution. It was also noted that images with even higher resolutions, however, are needed to adequately depict clay minerals and phases with small-scale features (e.g. muscovite) (Qin and Beckingham 2019).

Imaging and image analysis are powerful means of quantifying mineral properties to inform reactive transport simulations, including accessible surface areas where it has been found that accessible surface area better reflects mineral reactive surface area in porous media and better reproduces observed dissolution rates (Beckingham et al. 2017). However, capturing images under high resolutions and processing high resolution images is time-consuming and may have high computational costs. The necessity of this time and resource investment to improve simulation of mineral reactions and reactions rates, however, is not well understood. This work evaluates variations in simulated mineral reactions and reaction rates using mineral surface areas obtained from images with varying resolution and values obtained using traditional approaches. Mineral surface areas measured from image analyses in Qin and Beckingham, (2019) were used here to evaluate the impact of image resolution on simulated mineral reactions extents and reaction rates. These simulations are compared to those utilizing BET mineral surface areas from the literature and geometric surface areas (GSA) calculated assuming two uniform spherical sizes, one for clay minerals

and the other for non-clay minerals. Simulations compare variations in mineral reactions, reaction rates, and porosity over short and long times.

3.2. Materials and methods

3.2.1 Sample characterization

Sandstone samples extracted from the Paluxy formation at the Kemper County power plant, Kemper County, Mississippi, a prospective pilot CO₂ injection plant, were considered in this study. These samples were also the focus of previous analysis in Qin and Beckingham (2019) where bulk samples were collected from well MPC 10-4 #1 and well MPC 34-1 at depths from 1539 m to 1624 m. XRD analysis was performed on powdered samples and SEM BSE images of thin sections were captured for image analyses (Qin and Beckingham, 2019). The mineralogy, mineral abundances, and mineral volume fractions determined from 2D SEM BSE images of a thin section of the rock sample extracted at the depth of 1539 m (Qin and Beckingham, 2019) were used here and are reported in Table 3.1. Mineral abundances are defined as mineral volume percentage without pore space (m^3 mineral volume/ m^3 total mineral volume) and mineral volume fractions are defined as mineral volume percentage within the porous medium (m^3 mineral volume/ m^3 total porous medium volume). Mineral rate constant values (Table 3.1) were interpolated following Beckingham et al. (2016) at anticipated formation conditions post CO₂ injection corresponding to a temperature of 50°C and pH of 3.5.

Table 3.1 Mineral abundances calculated from a 0.34 μm 2D SEM image in Qin and Beckingham (2019) and corresponding mineral volume fractions and rate constants for reactive transport simulations. Rate constant values: quartz (Brady and Walther, 1990), K-feldspar (Van Hees et al., 2002), calcite (Alkattan et al., 1998), smectite (Amram and Ganor, 2005), muscovite (Knauss and Wolery, 1988; Oelkers et al., 2008), siderite (Golubev et al., 2009).

Mineral	Chemical formula ^a	Abundances (%)	Volume fraction (%)	Log k (mol/m ² /s) ^b
Quartz	SiO ₂	76.45	57.46	-11.6
K-feldspar	KAlSi ₃ O ₈	3.5	2.63	-11.65
Calcite	CaCO ₃	9.63	7.24	-4.21
Smectite	(Ca _{0.2} Na _{0.15})K _{0.2} (Fe _{0.29} Mg _{0.9})(Al _{1.25} Si _{3.75})(OH) _{6.5}	8.23	6.19	-13.35
Muscovite	KAl ₂ (AlSi ₃ O ₁₀)(OH) ₂	0.31	0.23	-12.67
Siderite	Fe _{0.9} Mg _{0.1} CO ₃	1.98	1.41	-5.69

^a Smectite and siderite chemical formula are determined from EDS linescan.

^b Mineral rate constants correspond to a temperature of 50°C and pH of 3.5.

3.2.2 Reactive transport simulations

3.2.2.1 Model description

Continuum scale reactive transport simulations were built and carried out using CrunchFlow (Steeffel et al., 2015). The model system (Fig. 3.1) consisted of a 3 cm long mineral cell in equilibrium with formation brine proceeded by a cell containing a constant partial pressure of CO₂ in equilibrium with formation brine that acts as a constant source of CO₂-saturated brine throughout the simulations. The mineral composition in the mineral cell was based on the mineral volume fractions determined from analysis of thin sections in Qin and Beckingham (2019) and given in Table 3.1. The initial formation brine chemistry (Table 3.2) was determined by simulating minerals equilibrating with 1 mol/(kg fluid) NaCl brine for 100,000 years where the resulting initial pH, based on charge balance, is 8.81.



Figure 3. 1. Diagram of the simulation system.

Table 3.2 Simulated brine chemistry of the Paluxy formation.

Ion	Concentration (mol/kg fluid)
Na ⁺	1.00E-00
Cl ⁻	1.00E-00
Ca ²⁺	7.00E-04
Mg ²⁺	5.88E-07
Fe ²⁺	5.64E-05
K ⁺	1.08E-04
Al ³⁺	1.08E-06
SiO ₂ (aq)	8.82E-04
CO ₂ (aq)	7.65E-04
pH	8.81

The estimated temperature and pressure at the sample depth, 1539 m, is 50 °C and 163 bar, calculated based on a temperature gradient of 25 °C/km and surface temperature of 10 °C and pressure gradient of 105 bar/km (Bachu, 2000; Crandell et al., 2009). These conditions control the solubility of CO₂ in the formation brine, calculated in CrunchFlow using the Duan and Sun model (Duan and Sun, 2003). These conditions result in a CO₂ saturated brine with a pH of 3.5. In the simulations, the CO₂ saturated brine flowed through the mineral cell at a constant flowrate of 1 m/day and the evolution of major ions and mineral volume fractions tracked. Precipitation of potential secondary mineral phases was also considered where the potential precipitating phases were selected using the database sweep option in CrunchFlow.

3.2.2.2 Mineral surface area

Table 3.3 Mineral surface area values used in reactive transport simulations. High and low resolution correspond to 0.34 μm and 5.71 μm resolution SEM images analyzed in Qin and Beckingham (2019), respectively. The surface area of quartz, K-feldspar, calcite and siderite were determined from images while the surface area of smectite and muscovite are from Beckingham et al. (2017) and Knauss and Wolery (1989), respectively. High and low BET literature refer to BET measured surface area values collected from the literature: quartz (Brady and Walther, 1989; Tester et al., 1994), K-feldspar (Bunsenberg and Clemency, 1976; Gautier et al., 1994), calcite (Papadopoulos and Rowell, 1988; Cubillas et al., 2005), smectite (Kennedy et al., 2002; Metz et al., 2005), muscovite (Caseri et al., 1992; Knauss, 1989), siderite (Shan and Guo, 2013; Erdem and Ozverdi, 2005). GSA_{RF} refers to geometric surface area multiplied by a roughness factor, RF , of 10 to account for surface roughness and GSA_{SF} is GSA_{RF} divided by a scaling factor, SF , of 10 to account for surface site reactivity.

Mineral	Surface area values (m^2/g)					
	high resolution imaging	low resolution imaging	$GSA_{RF} = GSA * RF$	$GSA_{SF} = GSA_{RF}/SF$	high BET literature	low BET literature
Quartz	2.56E-2	4.59E-2	1.18E-1	1.18E-2	1.11E-1	2.25E-2
K-feldspar	2.62E-2	1.49E-2	1.22E-1	1.22E-2	1.52E+0	1.12E-1
Calcite	1.10E-2	7.79E-3	1.15E-1	1.15E-2	1.64E+0	1.39E-2
Smectite	9.33E+0	9.33E+0	8.56E+1	8.56E+0	8.00E+2	3.40E+1
Muscovite	2.38E+0	2.38E+0	1.11E-1	1.11E-2	3.40E+0	1.10E+0
Siderite	1.77E-2	1.72E-2	7.90E-2	7.90E-3	5.17E+1	2.67E+0

Six different sets of surface area (Table 3.3) were determined and used in a systematic series of reactive transport simulations. This included two sets of accessible mineral surface areas determined using images at different resolutions, two sets of geometric surface areas with and without a scaling factor, and two sets of specific surface areas determined from BET analyses (Table 3.3). In CrunchFlow, mineral surface areas are updated as reactions proceed, based on the following relationships for dissolution and precipitation:

$$\text{Dissolution: } A = A_{\text{initial}} \left(\frac{\phi_m}{\phi_m^{\text{initial}}} \right)^{\frac{2}{3}} \left(\frac{\phi}{\phi^{\text{initial}}} \right)^{\frac{2}{3}} \quad (2)$$

$$\text{Precipitation: } A = A_{\text{initial}} \left(\frac{\Phi}{\Phi_{\text{initial}}} \right)^{\frac{2}{3}} \quad (3)$$

where A is the reactive surface area, Φ is the porosity and Φ_m is the individual mineral volume fraction.

3.2.2.2.1 Image obtained accessible surface area

Mineral accessible surface areas used here were calculated using a multi-scale 2D and 3D imaging approach in Qin and Beckingham (2019). Accessible surface was defined as mineral surfaces adjacent to connected pore spaces. In Qin and Beckingham (2019), these image-obtained accessible surface areas were calculated using 2D SEM images of varying resolution, 0.34 μm to 5.71 μm . Here, values from the highest (0.34 μm) and lowest (5.71 μm) image resolution were considered. It should be noted that even the image resolution of 0.34 μm was not sufficient to calculate surface area of smectite and muscovite, thus the surface area of smectite determined using FIB-SEM imaging from Beckingham et al. (2017) and BET measured value for muscovite from Knauss and Wolery (1989) were used here. The sets of image obtained surface areas are given in Table 3 and referred to as high resolution imaging and low resolution imaging.

3.2.2.2.2 Geometric specific and effective surface areas

Geometric surface areas were calculated from the experimentally measured average grain diameter for non-clay and clay minerals assuming spherical grains. The average grain diameters were determined from grain size distributions measured by Weatherford Labs for 7 samples from the Paluxy formation at depths of 1540 m, 1541 m, 1547 m, 1549 m, 1551 m, 1556 m, and 1562 m. The corresponding average grain diameters were 191.8 μm for non-clay minerals and 0.3 μm for clay minerals (details in supplementary materials). To account for mineral surface roughness, the spherical surface areas based on these grain diameters were multiplied by a roughness factor (RF) of 10 where the resulting surface area corresponds to an estimate of a specific surface area. A second set of surface area values reflecting limitations to surface reactivity, as would occur from reduced accessibility or only a fraction of the surfaces being reactive, were also calculated by dividing rough surface areas by a scaling factor, SF . Scaling factors typically range one to three orders of magnitude (White and Peterson, 1990) where a scaling factor of 10 is used here. The resulting surface area is an estimate of an effective surface area where values for both surface areas are given in Table 3.3 and are referred to as GSA_{RF} , the geometric surface area adjusted for surface roughness with a roughness factor, and GSA_{SF} , the rough geometric surface area adjusted by the scaling factor that accounts for both surface roughness and surface site reactivity.

3.2.2.2.3 Literature specific surface area

Mineral specific surface areas measured using the BET method (Brunauer et al., 1938) in previous studies were collected from the literature and used here. For a given

mineral phase, BET surface areas vary up to 4 orders of magnitude (Black et al., 2015; Bourg et al., 2015) depending on sample source, sample condition, adsorption method used, etc. Here, mineral specific surface areas reported in the literature were collected and the highest and lowest measured values on pure mineral samples were selected. These values are referred as the high BET literature and low BET literature in Table 3.3.

3.3. Results

Simulations first consider the impact of image resolution on simulated mineral reactions and reaction rates by comparison of simulations using accessible surface areas obtained from the highest and lowest resolutions images in Qin and Beckingham (2019). Then, this is further compared with simulations using surface area values more easily obtained including geometric surface areas based on average grain diameters and BET obtained specific surface areas. All simulations consider the evolution of mineral volume fractions, ion concentrations, pH, porosity and surface area. For all the simulation results, time starts from negative values, indicating the state of the system before CO₂ injection. At a time of 0 hours, CO₂-saturated brine enters the system. The purpose of this is to better reflect some of the changes happening at early times.

3.3.1 Imaging-based simulations

3.3.1.1 Mineral volume fractions

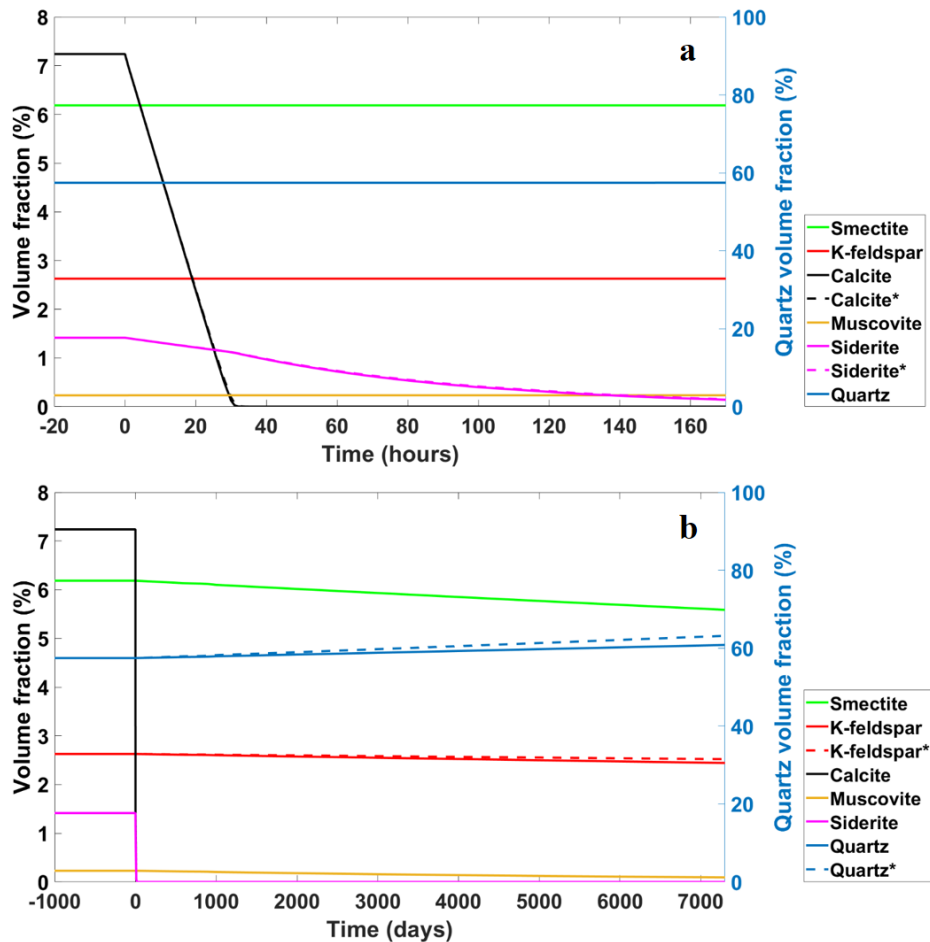


Figure 3. 2. Simulated evolution of mineral volume fraction using imaging-based accessible surface areas depicting (a) the first 170-hours and (b) the entire 7300-day simulation. Solid lines are results of simulations using surface areas from high resolution images (0.34 μm), dashed lines, also labeled with a *, indicate simulation results using surface areas from low resolution images (5.71 μm). A single solid line is shown for minerals with no discernable difference between the two simulations.

The evolution of mineral volume fractions from simulations carried out using imaging-based accessible surface area are shown in Figure 3.2. Here, surface areas vary by less than one order of magnitude for all minerals and result in very small variations in mineral volume fractions where discernable differences only occur at longer times (Figure 3.2b). In these simulations, CO_2 saturated brine enters the system at 0 hours and leads to dissolution of the two carbonate phases - calcite and siderite, while the other mineral phases remain relatively stable during the first 170 hours (Figure 3.2a). Calcite rapidly dissolves and it is close to depletion around 30 hours in both simulations, where the calcite volume fraction decreases from 7.23% to 0.13% in the simulation using the

accessible surface area from high resolution images (solid lines). In simulations using the accessible surface area from low resolution images, the calcite volume fraction decreases to 0.19% (dashed lines) at 30 hours. Compared to calcite, siderite dissolution is relatively slower and the dissolution rate slightly increases as calcite nears depletion. During the first 170 hours, the volume fraction of siderite decreases from 1.41% to 0.14% and to 0.15% in simulations using accessible surface area from high and low resolution images, respectively. Volume fractions of the other mineral phases change by less than 0.01%.

At longer times, quartz precipitates while smectite, K-feldspar and muscovite dissolve. There is little variation between in the two simulations using the different accessible surface area values. Quartz precipitates in both simulations due to the low pH and high $\text{SiO}_2(\text{aq})$ concentrations. It should be noted that previous works have suggested chalcedony, a polymorph of quartz, is the more likely precipitating phase (Audigane et al., 2007; Pham et al., 2011) but this was not observed in this simulation. Quartz surface areas vary within one order of magnitude where a higher accessible surface area, from the lower resolution images, results in a small increase in simulated precipitation, from 57.46% to 63.17% (dashed line) in comparison to the increase to 60.82% (solid lines) in the simulation using the accessible surface area from high resolution images. The volume fraction of K-feldspar decreases from 2.63% to 2.44% and 2.52% in simulations using accessible surface areas from high (solid lines) and low (dashed lines) resolution images, respectively. The volume fraction of smectite decreases from 6.18% to 5.59% and muscovite decreases from 0.23% to 0.09%. As these surface areas cannot be determined from imaging, the same BET surface area values are used for smectite and muscovite in these simulations and therefore no discernable differences in volume fractions of these mineral phases occur.

3.3.1.2 Ion concentration and pH

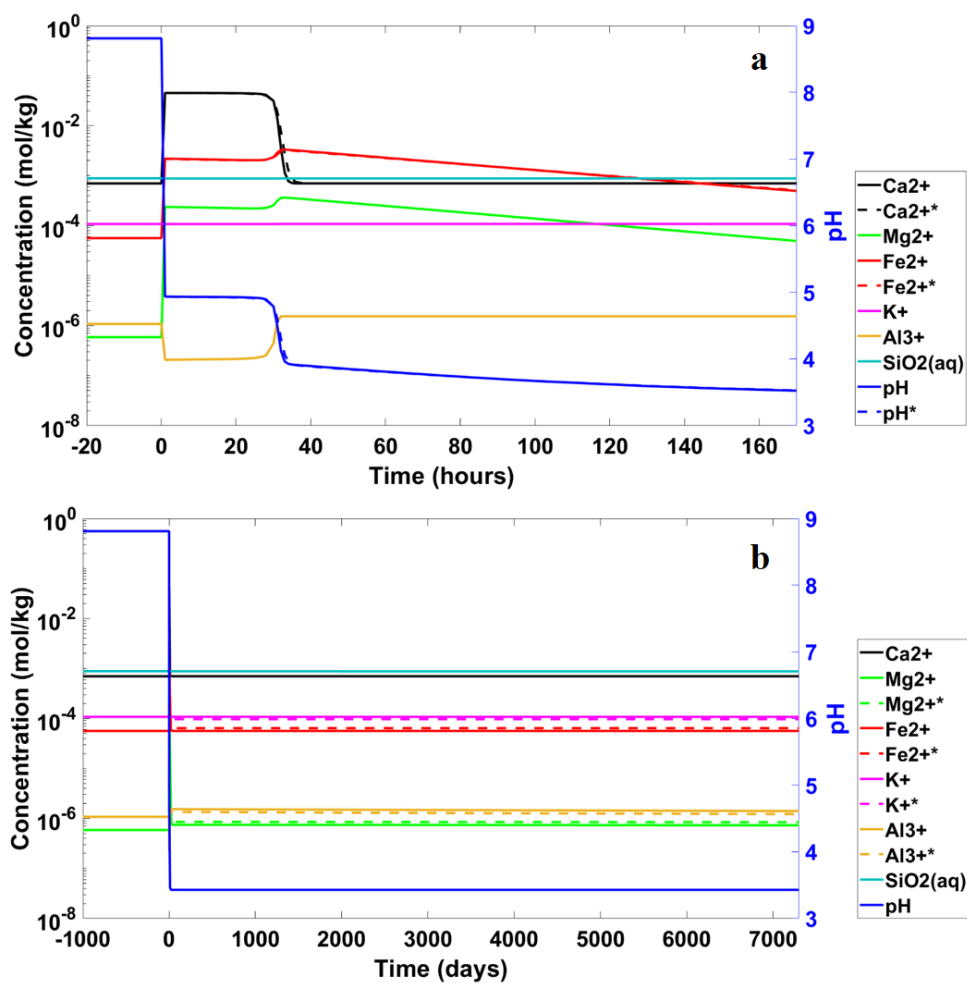


Figure 3.3. Simulated evolution of major ion concentrations and pH over a) 170 hours and b) 7300 days for simulations using imaging-based accessible surface areas. Solid lines are results of simulations using surface area from high resolution images (0.34 μm), dashed lines labeled with superscript * correspond to results of simulations using surface area from lower resolution images (5.71 μm).

The evolution of major ion concentrations and pH are shown in Figure 3.3. The introduction of CO_2 -saturated brine with a pH of 3.5 at 0 hours results in a decrease in the pH in the mineral cell from the initial pH of 8.8 and increases in the concentrations of calcium, magnesium and iron as calcite and siderite dissolve (Figure 3.3a). Calcite dissolution rapidly buffers the pH to 4.9. The decrease of aluminum ion concentration between 0 to 35 hours is most likely to be explained by the high super-saturation of muscovite (Fig. S1 in supplementary material). During this period, muscovite is super-saturated and a small amount of precipitation that is not discernable on the plot (Figure 3.2a) occurs. After 35 hours, when calcite is completely consumed, the pH reduces towards 3.5. These conditions no longer favor muscovite precipitation, so the aluminum concentration returns to the background level. No observable changes occur for potassium and $\text{SiO}_2(\text{aq})$ at early times. At longer times, slow dissolutions of smectite

and muscovite keep the aluminum and magnesium concentration levels slightly elevated above background levels. The concentrations of other ions remain stable at background levels.

Overall, the differences in pH and major ion concentrations are small in these two simulations using accessible surface areas from different resolution images. Only small variations in the evolution of pH and calcium concentration are observed around 35 hours (Figure 3.3a). At longer times, slight variations in magnesium, iron, potassium and aluminum can be observed. The good agreement between simulation results indicate that the variations in mineral accessible surface areas within one order of magnitude caused by differences in image resolution only have a small impact on simulated mineral reactions and reaction rates.

3.3.1.3 Porosity

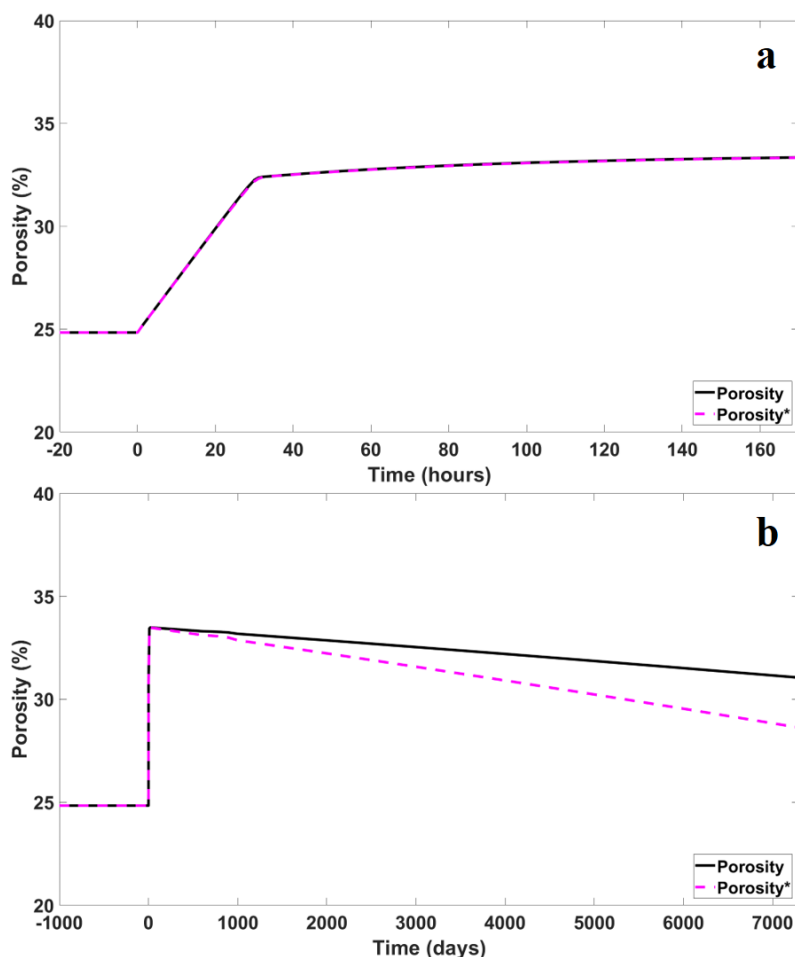


Figure 3. 4. Simulated porosity evolution over a) 170 hours and b) 7300 days for simulations using imaging-based accessible surface areas. Black solid lines are results of simulations using surface area from high resolution images (0.34 μm), magenta dashed lines, labeled with *, indicate results of simulations using surface areas from lower resolution images (5.71 μm).

The simulated porosity evolution for simulations using image obtained surface areas are shown in Figure 3.4. At early times, porosity increases following CO₂-saturated brine entering the system at 0 hours. In the first 170 hours, the porosity increases from 25% to 32% in both simulations (Figure 3.4a), mainly due to the dissolution of calcite. The porosity then further increases from 32% to 33% due to siderite dissolution. At later times, quartz slowly precipitates, resulting in a decrease in porosity from 33% to 31% in the simulation using accessible surface areas from the high resolution image (solid lines) and decreases to 29% in the simulation using accessible surface areas from the low resolution image (dashed lines). There is no discernable difference in porosity evolution over the first 170 hours (Figure 3.4a) and the variation in long-term porosity evolution between the two simulations is small (Figure 3.4b).

3.3.2 Non-imaging based simulations

In this section, results of simulations using BET specific surface areas and geometric specific and effective surface areas are presented and compared with results from simulations using image obtained accessible surface areas.

3.3.2.1 Mineral volume fractions

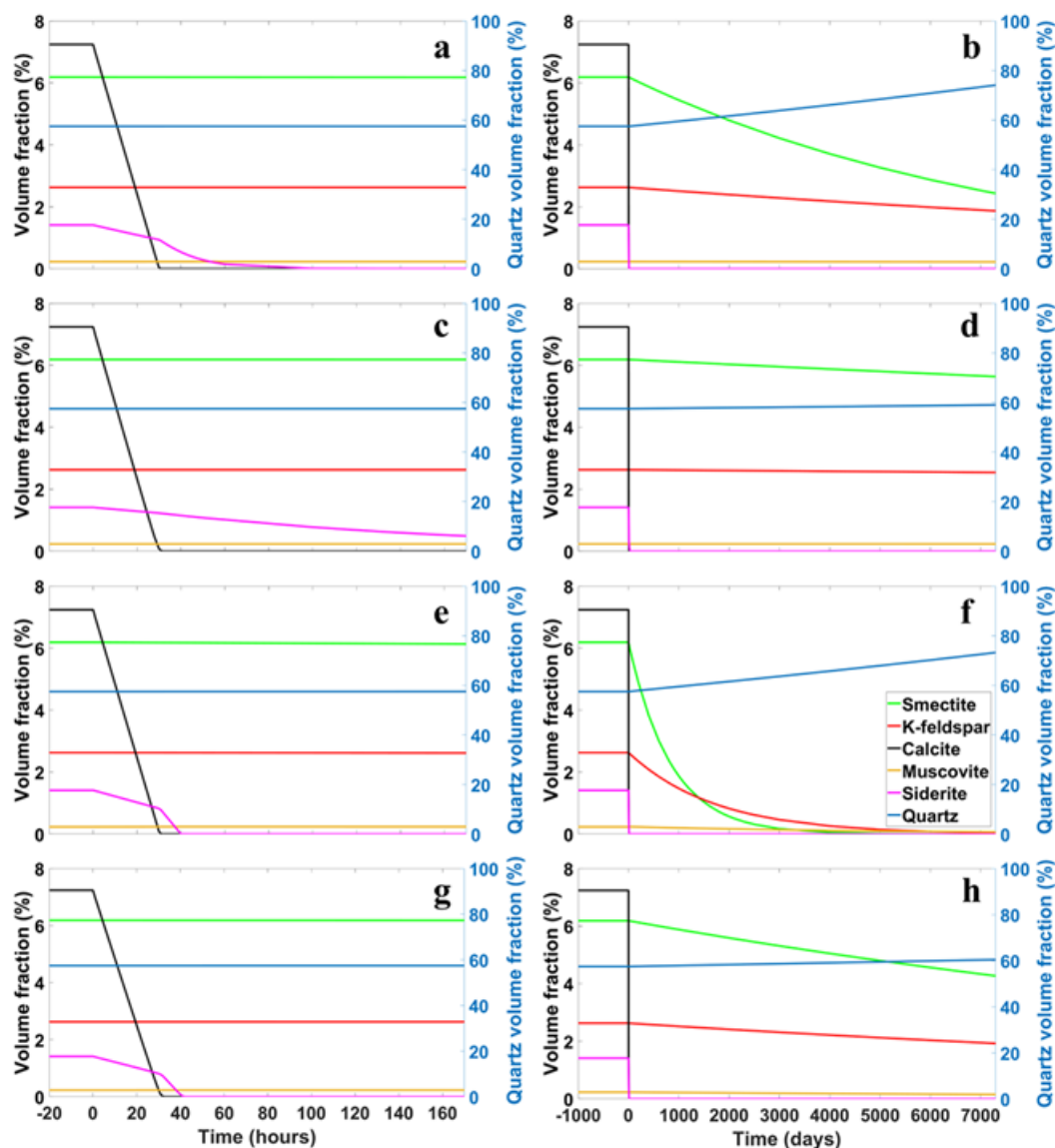


Figure 3. 5. Simulated evolution of mineral volume fractions using (a-b) geometric specific surface areas that account for surface roughness (GSA_{RF}), (c-d) geometric effective surface areas accounting for surface roughness and reactive site density (GSA_{SF}), (e-f) high BET literature specific surface areas, and (g-h) low BET literature specific surface areas.

The evolution of mineral volume fractions for simulations using geometric and BET specific surface areas are shown in Figure 3.5. Following introduction of CO_2 saturated brine (0 hours), calcite and siderite dissolve at early times. The dissolution of

siderite in simulations using geometric specific surface areas (Figure 3.5a), e.g. those that account for surface roughness, is slightly faster than in the two imaging-based simulations (Figure 3.2a). In simulations that use geometric effective surface areas (Figure 3.5c), the evolution of siderite volume fraction agrees relatively well with the two imaging-based simulations. Simulations carried out using literature BET specific surface areas have the fastest siderite dissolution rates and earliest siderite consumption times. In comparison to the accessible surface areas obtained from imaging, the geometric specific surface areas and BET specific surface area of siderite are 1 to 4 orders magnitude higher (Table 3.3). As expected, a higher surface area leads to a faster dissolution rate, particularly after consumption of calcite (30 hours) where the pH is lower. There is little variation in siderite dissolution rates in simulations using the highest surface areas, those from BET analyses (Figure 3.5e and g). While the high BET surface area is more than one order of magnitude larger than the low BET surface, this difference does not further increase the consumption rate of siderite. In comparison, there are more than 2 orders of magnitude variation in calcite surface areas among all simulations but no distinct differences in the calcite consumption rate can be observed. Little variation in volume fractions of the other four minerals occurs within the first 170 hours, in agreement with simulation results using image-obtained surface areas.

Over 7300 days, simulations that use higher surface areas (geometric and BET specific surface areas) have faster dissolution rates compared to simulations using image-obtained accessible surface areas (Figure 3.2), but to varying extents. In the two imaging-based simulations (Figure 3.2b), the smectite volume fraction decreases from 6.18% to 5.58% at 7300 days. In simulations using geometric specific and effective surface areas (Figure 3.5b and d), volume fractions of smectite decrease from 6.18% to 2.43% and 5.64% and decrease to 0.001% and 4.27% in simulations using high and low literature BET specific surface areas (Figure 3.5f and h) where increased depletion is coupled to higher surface area values. In simulations using image-obtained surface areas (Figure 3.2b), the volume fraction of K-feldspar decreases from 2.63% to 2.44% and 2.52% at 7300 days. With the higher surface areas used here (Figure 3.5), the volume fraction of K-feldspar decreases from 2.63% to 1.87% and 2.54% in simulations using geometric specific and effective surface areas (Figure 3.5b and d) and decreases to 0.04% and 1.93% in simulations using literature BET surface areas (Figure 3.5f and h) where increased depletion is also coupled to higher surface area values. Precipitation of quartz occurs to varying extents in all four simulations, driven by the low pH and abundant $\text{SiO}_2(\text{aq})$ in the flowing fluid. The volume fraction of quartz increases from 57.46% to 74.09% and 58.99% in simulations using geometric specific and effective surface areas (Figure 3.5b and d) and 73.21% and 60.42% in simulations using high and low literature BET surface areas (Figure 3.5f and h).

3.3.2.2 Ion concentration and pH

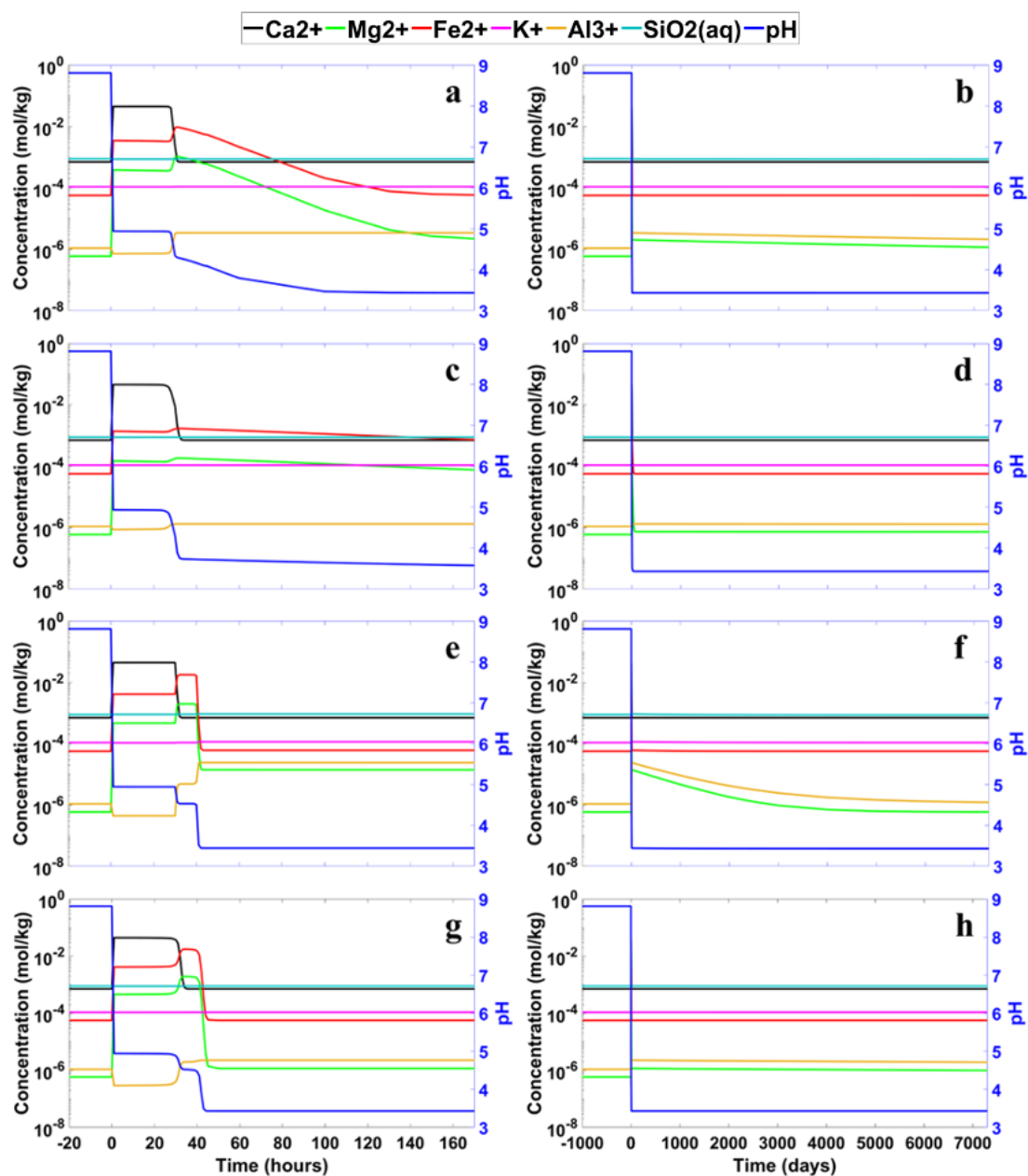


Figure 3. 6. Simulated evolution of major ion concentrations and pH for simulations using (a-b) geometric specific surface areas (those that reflect surface roughness, GSA_{RF}), (c-d) geometric effective surface areas (those accounting for surface roughness and adjusted by a scaling factor to reflect reactive site density, GSA_{SF}), (e-f) high BET literature specific surface areas, and (g-h) low BET literature specific surface areas.

Ion concentrations for simulations using geometric surface areas and BET surface areas from the literature are shown in Figure 3.6. Variations in ion concentrations among simulations, and with simulation results using image-obtained accessible surface areas (Figure 3.3), are readily apparent. As CO_2 -saturated brine enters the system at 0 hours, calcium, magnesium and iron concentrations increase as calcite and siderite dissolve. From 0 to 30 hours, dissolution is dominated by calcite and evident

here through high calcium concentrations. While there are two orders of magnitude variation in geometric and BET surface areas, this only results in small variations in simulated calcium ion concentrations. As calcite approaches depletion, siderite dissolution increases and becomes dominant which leads to further increases in magnesium and iron concentrations after 30 hours. Variations in magnesium and iron occur between simulations, resulting from differences in siderite dissolution rates. Although there is no discernable difference in siderite volume fractions (Figure 3.5e and g), the concentration level of magnesium is higher for simulations using higher BET specific surface areas (Figure 3.6e and g). pH closely follows the dissolution of calcite, buffered by calcite dissolution to 4.9 during 0 to 30 hours and then decreasing to 3.5 after 30 hours when calcite is depleted. The evolution of aluminum concentration follows the change of muscovite saturation index (Figure S1), where muscovite initially precipitates and decreases aluminum concentrations and then dissolves and increases aluminum concentrations.

Variations in concentration tied to surface areas can be observed where higher surface areas result in higher reaction rates and associated ion concentrations. In comparison to simulations using image-obtained accessible surface areas at early times, calcium concentrations return to background levels quicker in comparison to in simulations using geometric specific surface area and high literature BET specific surface area where calcite has a higher surface area by 1-2 orders of magnitude and is depleted more rapidly. This also impacts the evolution of pH, largely controlled by calcite dissolution, and magnesium and iron, where the dissolution rate of siderite increases after calcite depletion. Higher concentrations of iron, magnesium and aluminum and more rapid changes in their concentrations can be observed in the simulations using the higher surface area values.

At longer times, elevated levels of magnesium and aluminum can be observed, reflecting dissolution of smectite and muscovite. In terms of the surface area values used in the simulations, higher surface areas lead to faster dissolution and therefore higher concentrations of magnesium and aluminum in the first 5000 days. After 5000 days, however, there is little variation in magnesium and aluminum concentrations among simulations until smectite and muscovite approaching depletion (Figure 3.5f and Figure 3.6f) where concentrations approach background levels. In comparison, potassium and iron have higher background concentrations, such that the release of potassium and iron due to slight mineral dissolution (e.g. K-feldspar and smectite) do not largely impact potassium and iron concentrations. Overall, variations in ion concentrations among all simulations, including those using image-obtained accessible surface areas, are readily apparent at early times (170 hours) and small at longer times. Simulated ion concentrations after ~500 days agree well for simulations using low BET specific surface areas and geometric specific and effective surface areas. After ~5000 days, simulated ion concentrations for simulations using high BET surface areas agree well with other simulation results.

3.3.2.3 Porosity

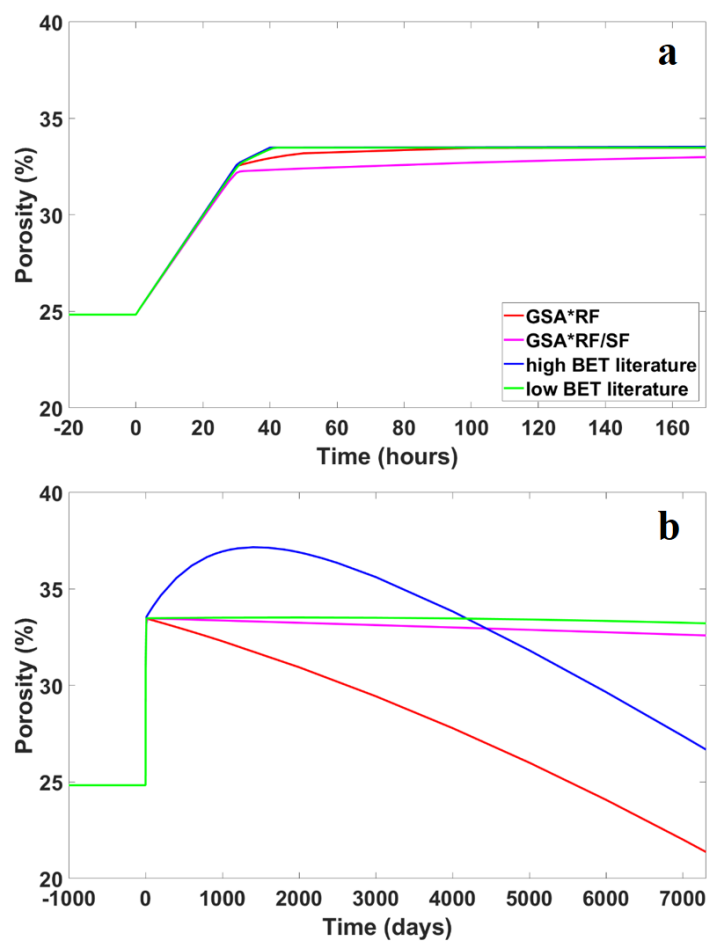


Figure 3. 7. Simulated porosity evolution using geometric specific and effective surface areas and literature BET specific surface areas.

The simulated evolution of porosity for simulations using geometric surface areas and BET specific surface areas are shown in Figure 3.7. Rapid dissolution of carbonate minerals following introduction of CO₂-saturated brine at 0 hours results in an increase in porosity from 25% to around 33% in all four simulations (Figure 3.7a). While the calcite and siderite surface area values in the simulations vary by 2 and 4 orders of magnitude, respectively, the overall difference in porosity increase is small in 170 hours.

Over longer times, variations in surface area values result in larger differences in the simulated evolution of porosity. In simulations that use the highest BET surface area values from the literature (green line), the porosity further increases to 37% due to dissolution of smectite and K-feldspar. In all simulations, after the initial porosity increase, porosity decreases as little additional dissolution occurs and SiO₂ precipitates. The extent of precipitation, and corresponding change in porosity, varies between simulations where the porosity decreases from 33% to 21% in the simulations that use geometric specific surface areas (red lines) and decreases to 27% in the simulations that use high BET literature specific surface area values (green lines). This is higher than

the decrease to 31% and 29% in simulations using surface areas from high- and low-resolution images, respectively. In simulations where smaller surface areas of SiO₂ are used, geometric effective surface areas and low BET specific surface areas (magenta and green lines), the porosity only decreases slightly over 7300 days which better agrees with results from simulations using image obtained accessible surface areas.

3.3.3 Mineral surface area evolution

Here, the simulated evolution of mineral surface areas is tracked where surface areas are updated in CrunchFlow using Equations 2 and 3 for dissolution and precipitation, respectively. Mineral surface area evolutions in the first 170 hours are presented here for calcite and siderite, while the surface areas for the other four mineral phases are minor and given in Figure S2 in the supplementary materials. At longer times, calcite and siderite are completely dissolved and thus only the surface area evolution of the remaining phases, quartz, K-feldspar, smectite and muscovite, are presented here.

3.3.3.1 Short term surface area evolution

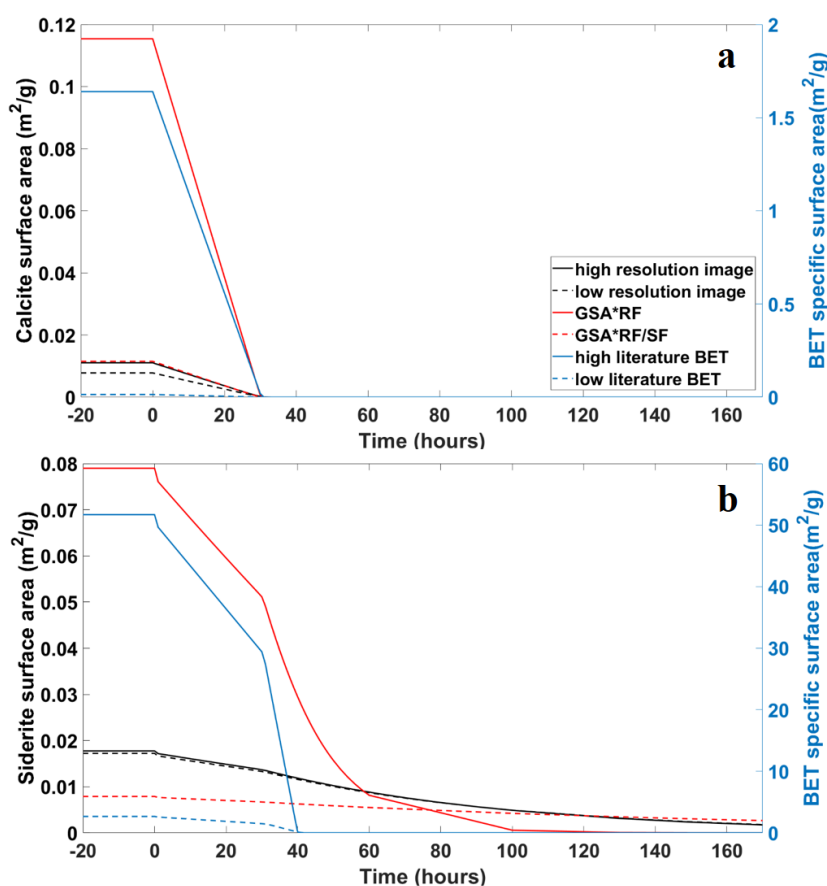


Figure 3. 8. Simulated mineral surface area evolution of carbonate minerals over the first 170 hours: (a) calcite and (b) siderite. The evolution of BET specific surface areas (blue lines) are plotted on the right y-axis.

The simulated evolution of mineral surface area for calcite and siderite for all six

simulations are shown for the first 170 hours in Figure 3.8. There are 2 orders of magnitude variation in calcite surface areas where the simulated evolution of surface areas that are initially higher decreases faster than surface areas that are initially lower. In all simulations, the surface area of calcite decreases to 0 around 30 hours, reflecting calcite depletion (Figure 3.8a). A similar phenomenon can be observed for siderite, where initial surface area values span 4 orders of magnitude. Higher surface areas result in more rapid simulated decreases in surface area. The surface area of siderite additionally decreases even more rapidly upon depletion of calcite. Unlike calcite, the surface area evolution of siderite varies among simulations where the two highest surface areas (BET specific surface areas, Figure 3.8b, blue lines) approach a surface area of 0 around 40 hours, indicating siderite depletion. In the other simulations, it takes longer for the siderite surface area to decrease to 0 and siderite to be consumed. As can be expected from equation 3, the overall surface area evolutions are similar to volume fraction evolutions (Figure 3.2a).

3.3.3.2 Long term surface area evolution

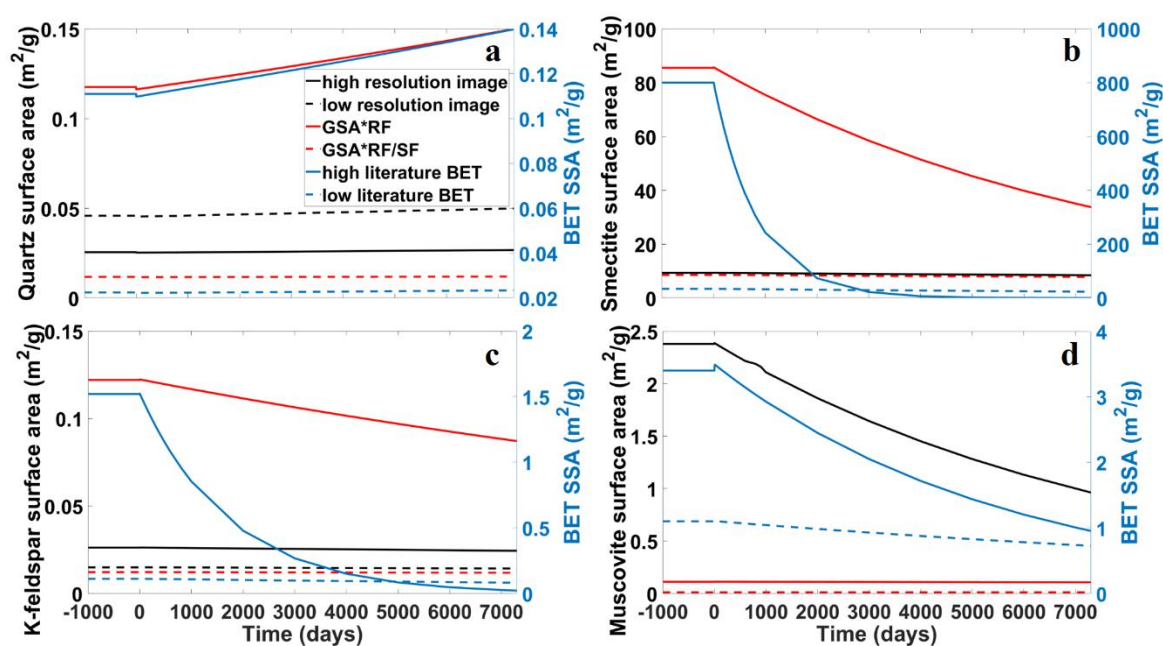


Figure 3. 9. Simulated mineral surface area evolution of non-carbonate minerals over 7300 days: (a) quartz, (b) smectite, (c) K-feldspar and (d) muscovite. The evolution of BET specific surface areas (blue lines) are plotted on the right y-axis.

The evolution of surface area for the non-carbonate minerals at longer times are shown in Figure 3.9. Some distinct variations in the simulated evolution of surface areas can be observed here. Little variation in the simulated evolution of surface area occurs in simulations using smaller surface area values. Conversely, increases and decreases in surface area occur in simulations using larger surface area values (blue and black lines in Figure 3.9a, b and c, blue and black lines in Figure 3.9d). Such changes also correspond to the volume fraction evolution in Figure 3.5, where dissolution

corresponds to a simulated decrease in the surface areas of the dissolving phases and precipitation to an increase in surface area. For example, in Figure 3.9a, the surface area of quartz (SiO₂) increases as SiO₂ precipitates (Figure 3.5b, d, f, h).

3.4. Discussion

Table 3.4 Differences of the surface area values used in reactive transport simulations as compared to values obtained from the 0.34 μm images (high resolution). Surface area value differences = surface area value/ surface area from high-resolution imaging.

Mineral	Surface area value differences					
	high resolution imaging	low resolution imaging	GSA _{RF} = GSA*RF	GSA _{SF} = GSA _{RF} /SF	high BET literature	low BET literature
Quartz	1.00E+0	1.79E+0	4.61E+0	4.61E-1	4.34E+0	8.79E-1
K-feldspar	1.00E+0	5.69E-1	4.66E+0	4.66E-1	5.80E+1	4.27E+0
Calcite	1.00E+0	7.08E-1	1.05E+1	1.05E+0	1.49E+2	1.26E+0
Smectite	1.00E+0	1.00E+0	9.17E+0	9.17E-1	8.57E+1	3.64E+0
Muscovite	1.00E+0	1.00E+0	4.66E-2	4.66E-3	1.43E+0	4.62E-1
Siderite	1.00E+0	9.72E-1	4.46E+0	4.46E-1	2.92E+3	1.51E+2

Differences among the surface area values determined from images, calculated using geometric approaches, and collected from the literature are shown in Table 4 and vary by many orders of magnitude. In general, mineral accessible surface areas calculated from image analyses are small compared to specific surface area values obtained from BET analysis and geometric approaches. The differences between accessible surface areas calculated from images (0.34 μm and 5.71 μm resolutions) are within one order of magnitude. The differences between accessible surface areas and geometric surface areas are mostly within 1 order of magnitude, except for muscovite where there are more than 2 orders of magnitude variation. This, however, is largely dependent on the choice of roughness and scaling factor. Typically, a roughness factor of 10 and scaling factor one to three orders of magnitude is used (Peters, 2009; Landrot et al., 2012; Beckingham et al., 2016; Kweon and Deo, 2017), but there is little guidance in terms of how to select appropriate values. Specific surface areas measured using the BET approach are as much as 1-4 orders of magnitude higher than image obtained surface areas.

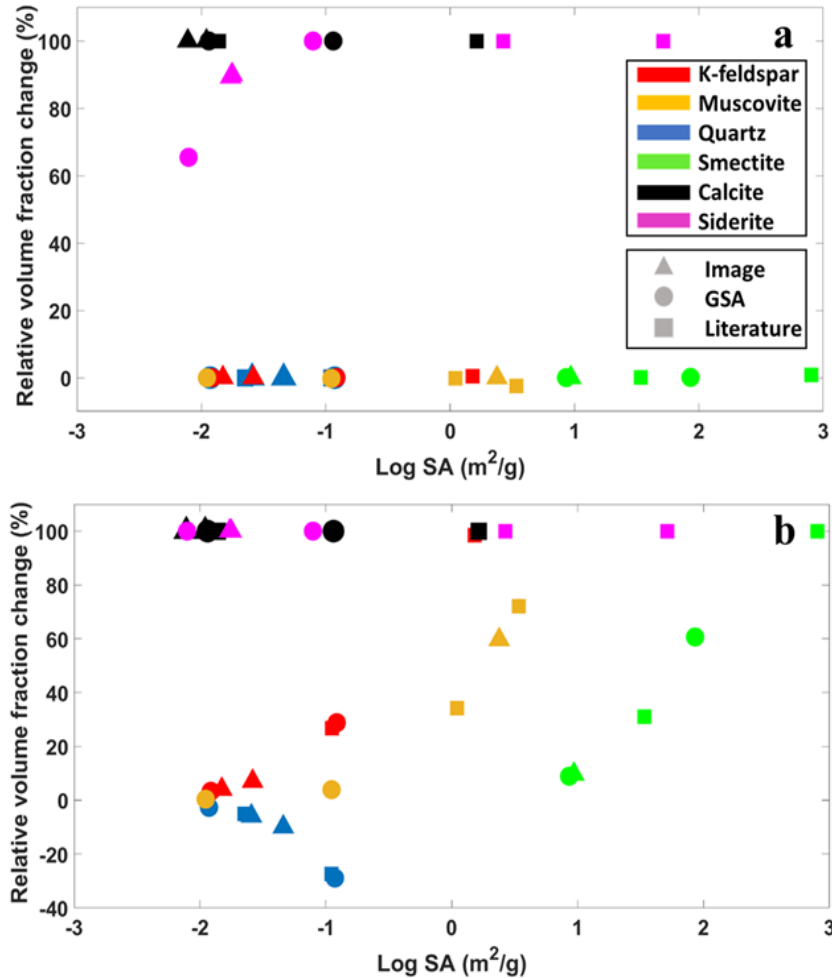


Figure 3. 10. Relative percentage change of simulated mineral volume fractions for different initial surface area values at (a) 170 hours and (b) 7300 days. Relative percentage change is the difference in the initial volume fraction and the final volume fraction over the initial volume fraction. Positive values indicate dissolution (decrease in volume fraction) and negative values indicate precipitation (increase in volume fraction). Simulations using image obtained surface areas are shown with triangles, geometric surface areas simulations with circles, and simulations using BET values from the literature shown with squares.

Mineral reaction rate directly increases with increasing mineral reactive surface area (e.g. Equation 1). This, however, results in different variations in mineral volume fractions among the different mineral phases. The simulated relative percentage change in mineral volume fractions with respect to the reactive surface area values used in the simulations for the different mineral phases is shown in Figure 3.10. This reflects the total change in mineral volume fraction for 170 hours and 7300 days where complete dissolution is indicated by 100%.

Among all simulations, the surface area values of calcite vary up to 2 orders of magnitude (Figure 3.10). Such variations in calcite surface area resulted in no discernable differences in the evolution of calcite volume fraction at 170 hours or 7300

days, where these times correspond to typical laboratory or field conditions, for example. As such, simulations with different calcite surface areas, all reach calcite depletion around the same time (~35 hours). It can thus be inferred that if the timescale of interest in the simulation is beyond the timescale of calcite depletion, even larger variations in surface area will likely not yield any difference in the final simulated calcite volume fraction and contribution of calcite dissolution to porosity. The rate controlling process of the reaction needs to also be considered where reactions have been observed to be either surface or transport controlled. At the conditions considered, calcite has a high reaction rate constant and is very under-saturated in the solution such that the dissolution of calcite here is most likely transport-controlled rather than surface-controlled (Raines and Dewers, 1997; Morse and Arvidson, 2002; Morse et al., 2007). Pokrovsky et al. (2019) also observed that at elevated temperatures (60-100 °C) and $\text{pH} < 4.5$, the calcite reaction rate is not proportional to H^+ activity at the mineral surface, but rather is controlled by transport of H^+ to the calcite surface.

Siderite surface area values used here vary up to 4 orders of magnitude and variations in siderite volume fraction with changing surface area are quite obvious at 170 hours but no longer apparent at 7300 days (Figure 3.10). In simulations using image obtained surface areas, siderite volume fractions change by 90% at 170 days. With one order of magnitude variation in geometric surface areas (Figure 3.10a, magenta circles), the volume fraction of siderite changed by 65% and 100%, respectively. The two highest surface areas - BET specific surface areas, also result in complete consumption of siderite and a 100% decrease in siderite volume fraction at 170 hours. As all simulations result in complete siderite consumption within hundreds of hours, there is agreement in the overall change in siderite volume fraction at 7300 days, even though surface areas span 4 orders of magnitude.

Compared to calcite and siderite, the other four mineral phases have lower reaction rates. Large variations in surface areas for these phases result in less than 0.1% variation in volume fractions at 170 hours. Therefore, selecting surface areas for these mineral phases from different sources would not have large effects on the simulated results if the goal was to understand the extent of reaction of these phases at shorter time scales, e.g. 170 hours or similar timescales. However, at longer times, the changes in mineral volume fraction can vary widely. As shown in Figure 3.10, the differences of surface areas used in the six simulation scenarios are more than 2 orders of magnitude for K-feldspar and muscovite, around 2 orders of magnitude for smectite, and around 1 order of magnitude for quartz. Smaller K-feldspar surface areas result in minor (<5%) dissolution while K-feldspar is almost completely consumed (>95%) at 7300 days when larger surface areas are used. When BET specific surface areas are used (Figure 8b, red square boxes), one order of magnitude variation in surface area results in significant differences in the evolution of mineral volume fractions (from 27% to 99%). On the other hand, when imaging-based accessible surface areas and geometric surface areas are used (Figure 3.8b, red triangles and red circles), the resulted variations in mineral

volume fractions are smaller (from 4% to 29%). A similar phenomenon occurs for muscovite where minor (<5%) dissolution of muscovite occurs when using lower values of surface area and 34% to 72% dissolution of muscovite occurs in simulations using higher surface areas at 7300 days. These variations in mineral volume fraction, however, require >2 orders of magnitude difference in surface area values. The extent of smectite dissolution also depends on surface area where the extent of dissolution increases with increasing surface area (8.9% to >99%). Small variations (<1 order of magnitude) in smectite surface area yield significant differences in the simulated volume fraction. This may lead to variations in estimated formation properties as clay minerals can largely alter the permeability and geomechanical properties of the formations, as observed for formations targeted for CO₂ injection (Bourg, 2015; Bourg et al., 2017).

Quartz surface areas vary by approximately one order of magnitude where increased precipitation occurs with increasing surface area. While the overall variation in volume fraction at the end of the simulation is smaller compared with other mineral phases, there is a significant impact on the resulting porosity because quartz is the most abundant mineral phase in the system (57.46%). As such, a difference in simulated volume fraction of 10% to 30% results in significant variations in simulated sample porosity. Potential precipitation of additional mineral phases was also considered but no such phenomena is simulated to occur, most likely due to constant flow of CO₂-saturated brine and the corresponding consistent low pH conditions.

It should also be noted that while variations in surface areas may not result in discernable differences in mineral volume fractions (Figure 3.5e and g), it can result in differences in the evolution of ion concentrations (Figure 3.6e and g), which could lead to other changes the system. For instance, higher concentrations of magnesium and aluminum could promote precipitation of clay minerals downstream. The simulation model in this work considers CO₂-saturated brine constantly flowing through the system, maintaining pH at a low level – 3.5. This could represent the close-to-well zones during CO₂ injection, for example, where brine is saturated with CO₂. These conditions do not favor precipitation of carbonate or clay minerals but do correspond to conditions favorable for released SiO₂(aq) to precipitate as quartz. Variations in the simulated rate and extent of mineral dissolution and precipitation reactions in these systems could potentially lead to very different results, including changes in porosity and permeability critical for assessing the fate and impact of injected CO₂.

Mineral surface area evolution mimics the evolution of mineral volume fractions where higher initial surface areas result in faster reaction rates and faster changes in surface area (Equations 2 and 3). For minerals with higher reaction rates (e.g. calcite and siderite), the variations in the initial surface area have small impacts on the overall surface area evolution. For reactions with lower reaction rates that are more limited by reaction kinetics, variations in the initial surface area result in different evolutions of mineral surface area as well as mineral volume fraction. Minerals with lower reaction

rates only have distinct changes in surface area at longer times, where variations in initial surface areas result in large differences in the evolution of mineral surface area (Figure 3.9) as well as volume fraction (Figure 3.5). For these minerals, higher initial surface areas result in simulated distinct changes over 7300 days, whereas lower surface areas remain stable throughout the 7300-day simulations (Figure 3.9). For low reaction rate constants (e.g. non-carbonate minerals), impacts of variations surface area will be lessened as reaction kinetics already limit the rate of reaction. However, in the higher ranges of surface area for these phases, where surfaces vary up to 4 orders of magnitude, variations in reaction kinetics are magnified.

Conclusions

This work aims to understand the impact of mineral surface area on simulated mineral reaction extents and reaction rates. Here, mineral surface areas values were obtained from image analyses, literature BET measurements and geometric approximations and used in reactive transport models to simulate CO₂-brine-mineral reactions under reservoir conditions over varying times. Six sets of surface area values were collected, two sets of accessible surface area calculated from image analyses, two sets of specific surface areas from BET measurements in the literature and specific and effective surface areas calculated using geometric approaches. Differences in these surface area values are several orders of magnitude. Variations in simulated results were observed but depend on the mineral phase as well as the time scale.

The variations in accessible surface area caused by image resolution differences are fairly small (< 1 order of magnitude) and have little impact on the simulated reactions on both short (hours) and long (years) time scales. However, selecting surface area values from the literature or calculating surface areas based on geometry could yield significantly different results in regard to the rate and extent of reactions as well as the long-term evolution of porosity.

Table 3.5 Summary of surface area impact on simulated mineral reactions and reaction rates in short term and long term. Numbers listed under surface area variations are referring to the surface area differences in orders of magnitude. Rate constant values: quartz (Brady and Walther, 1990), K-feldspar (Van Hees et al., 2002), calcite (Alkattan et al., 1998), smectite (Amram and Ganor, 2005), muscovite (Knauss and Wolery, 1988; Oelkers et al., 2008), siderite (Golubev et al., 2009).

Reactivity	Category	Mineral	Log k	Surface area variations in orders of magnitude	Short term	Long term
More reactive	carbonate	calcite	-4.21	1-2	minimum	minimum
		siderite	-5.69	1-4	large in higher SA range	minimum
More stable	non-clay	K-feldspar	-11.65	1-2	minimum	large in higher SA range
		muscovite	-12.67	1-3	minimum	large in higher SA range
		quartz	-11.60	1	minimum	large
	clay	smectite	-13.35	2	minimum	large

The extent of impact of variations in surface area on simulated mineral reactions and reaction rates depends on the time scale of interest. A summary of the observations varying surface areas had for each mineral phase over short and long time scales is given in Table 3.5. For minerals with fast reaction rates, large discrepancies in the simulated evolution of mineral phases will occur over short times (10s of hours) with varying surface areas. Among the more reactive minerals, calcite dissolution is not largely impacted by surface area variations while such impacts are more obvious for siderite. The overall impact of variations in calcite and siderite surface areas on the long-term evolution of the system (100s of hours), however, is small. For more stable minerals with lower reaction rates, such as K-feldspar, muscovite, smectite and quartz, variations in surface area have little impact on short time scales. Variations in reaction rates however are important over long times where large variations in the evolution of mineral volume fractions occur with different surface areas for these phases.

Simulations also revealed that it is essential to have a good understanding of the quartz surface area as the overall porosity evolution of the system is largely impacted by simulated SiO₂ precipitation.

Previous work found that accessible surface areas obtained from imaging better reflect the reactive surface areas and better reproduce the observed mineral reaction rates in core-flood experiments when comparing with other means of estimating reactive surface areas (Beckingham et al., 2017). Therefore, estimating accessible surface areas from imaging is generally preferred. However, imaging rock samples and then processing the 2D and 3D images to quantify accessible mineral surface areas is challenging and time and resource intensive. Higher resolution images are preferred when clay minerals are abundant (Qin and Beckingham, 2019), but this results in increased computational costs. Images with lower resolutions and proper processing can yield good results (mineral abundance, accessible surface area) and give similar simulated mineral reactions and reaction rates, especially in comparison to simulations carried out using surface areas calculated from higher resolution images. Depending on the purpose of the simulation, image analyses might not be necessary in some cases. For example, when simulating short term (10s of hours) CO₂-brine-mineral reactions with samples composed predominantly of more stable phases such as K-feldspar, using surface area calculated from images, BET values from the literature, or surface areas estimated from geometry yield similar results. This is also true for long term simulations (100s of hours) of CO₂-brine-mineral reactions for samples predominantly composed of highly reactive phases such as calcite. In either of these cases, imaging samples and processing captured images may not be necessary as other means of mineral surface area estimates are much less time and resource intensive and yield comparable results. However, when research interests are on the short-term evolution of samples composed of highly reactive phases (e.g. calcite and siderite) or the long-term evolution of samples composed of more stable phases (e.g. K-feldspar, muscovite, quartz, etc.), surface areas estimated using different approaches will largely impact the simulated results including the rate and extent of the reactions as well as the evolution of porosity. In these cases, a more thorough understanding of accessible mineral surface area is needed. Close attention also needs to be paid to the surface area of precipitating phases that may largely impact porosity, SiO₂ here, where differences in quartz surface area resulted in critical variations in porosity on long time scales. It was also observed here that other means of estimating effective surface area may be effective where simulations carried out using geometric effective surface areas that account for both surface roughness and surface site reactivity agree relatively well with imaging-based simulations. However, this means of estimating surface area is largely imprecise and relies heavily on the choice of roughness and scaling factor, for which there is little guidance.

Acknowledgement

This work supported by the “Establishing an Early CO₂ Storage Complex in Kemper, MS” project funded by the U.S. Department of Energy’s National Energy Technology Laboratory and cost-sharing partners under grant number FE0029465, managed by the Southern States Energy Board. Analysis of surface area evolution supported by the National Science Foundation under Grant No. EAR-1847243.

References

1. Aagaard, P. and Helgeson, H.C., 1982. Thermodynamic and kinetic constraints on reaction rates among minerals and aqueous solutions; I, Theoretical considerations. *American journal of Science*, 282(3), pp.237-285.
2. Alemu, B.L., Aagaard, P., Munz, I.A. and Skurtveit, E., 2011. Caprock interaction with CO₂: A laboratory study of reactivity of shale with supercritical CO₂ and brine. *Applied Geochemistry*, 26(12), pp.1975-1989.
3. Alkattan, M., Oelkers, E.H., Dandurand, J.L. and Schott, J., 1998. An experimental study of calcite and limestone dissolution rates as a function of pH from -1 to 3 and temperature from 25 to 80 C. *Chemical geology*, 151(1-4), pp.199-214.
4. Atree-Williams, A., Brugger, J., Pring, A. and Bedrikovetsky, P., 2019. Coupled reactive flow and dissolution with changing reactive surface and porosity. *Chemical Engineering Science*, 206, pp.289-304.
5. Amram, K. and Ganor, J., 2005. The combined effect of pH and temperature on smectite dissolution rate under acidic conditions. *Geochimica et Cosmochimica Acta*, 69(10), pp.2535-2546.
6. Anbeek, C., 1992. Surface roughness of minerals and implications for dissolution studies. *Geochimica et Cosmochimica Acta*, 56(4), pp.1461-1469.
7. Apul, D.S., Gardner, K.H. and Eighmy, T.T., 2007. Modeling hydrology and reactive transport in roads: The effect of cracks, the edge, and contaminant properties. *Waste management*, 27(10), pp.1465-1475.
8. Aradóttir, E.S.P., Sonnenthal, E.L., Björnsson, G. and Jónsson, H., 2012. Multidimensional reactive transport modeling of CO₂ mineral sequestration in basalts at the Hellisheidi geothermal field, Iceland. *International Journal of Greenhouse Gas Control*, 9, pp.24-40.
9. Audigane, P., Gaus, I., Czernichowski-Lauriol, I., Pruess, K. and Xu, T., 2007. Two-dimensional reactive transport modeling of CO₂ injection in a saline aquifer at the Sleipner site, North Sea. *American journal of science*, 307(7), pp.974-1008.
10. Bachu, S., 2000. Sequestration of CO₂ in geological media: criteria and approach for site selection in response to climate change. *Energy conversion and Management*, 41(9), pp.953-970.
11. Bacon, D.H., Sass, B.M., Bhargava, M., Sminchak, J. and Gupta, N., 2009. Reactive transport modeling of CO₂ and SO₂ injection into deep saline formations and their effect on the hydraulic properties of host rocks. *Energy Procedia*, 1(1),

- pp.3283-3290.
12. Beckingham, L.E., Mitnick, E.H., Steefel, C.I., Zhang, S., Voltolini, M., Swift, A.M., Yang, L., Cole, D.R., Sheets, J.M., Ajo-Franklin, J.B. and DePaolo, D.J., 2016. Evaluation of mineral reactive surface area estimates for prediction of reactivity of a multi-mineral sediment. *Geochimica et Cosmochimica Acta*, 188, pp.310-329.
 13. Beckingham, L.E., Steefel, C.I., Swift, A.M., Voltolini, M., Yang, L., Anovitz, L.M., Sheets, J.M., Cole, D.R., Kneafsey, T.J., Mitnick, E.H. and Zhang, S., 2017. Evaluation of accessible mineral surface areas for improved prediction of mineral reaction rates in porous media. *Geochimica et Cosmochimica Acta*, 205, pp.31-49.
 14. Black, J.R., Carroll, S.A. and Haese, R.R., 2015. Rates of mineral dissolution under CO₂ storage conditions. *Chemical Geology*, 399, pp.134-144.
 15. Boano, F., Harvey, J.W., Marion, A., Packman, A.I., Revelli, R., Ridolfi, L. and Wörman, A., 2014. Hyporheic flow and transport processes: Mechanisms, models, and biogeochemical implications. *Reviews of Geophysics*, 52(4), pp.603-679.
 16. Bourg, I.C., 2015. Sealing shales versus brittle shales: a sharp threshold in the material properties and energy technology uses of fine-grained sedimentary rocks. *Environmental Science & Technology Letters*, 2(10), pp.255-259.
 17. Bourg, I.C. and Ajo-Franklin, J.B., 2017. Clay, water, and salt: controls on the permeability of fine-grained sedimentary rocks. *Accounts of chemical research*, 50(9), pp.2067-2074.
 18. Bourg, I.C., Beckingham, L.E. and DePaolo, D.J., 2015. The nanoscale basis of CO₂ trapping for geologic storage. *Environmental science & technology*, 49(17), pp.10265-10284.
 19. Brady, P.V. and Walther, J.V., 1989. Controls on silicate dissolution rates in neutral and basic pH solutions at 25 C. *Geochimica et Cosmochimica acta*, 53(11), pp.2823-2830.
 20. Brady, P.V. and Walther, J.V., 1990. Kinetics of quartz dissolution at low temperatures. *Chemical geology*, 82, pp.253-264.
 21. Brunauer, S., Emmett, P.H. and Teller, E., 1938. Adsorption of gases in multimolecular layers. *Journal of the American chemical society*, 60(2), pp.309-319.
 22. Busenberg, E. and Clemency, C.V., 1976. The dissolution kinetics of feldspars at 25 C and 1 atm CO₂ partial pressure. *Geochimica et Cosmochimica Acta*, 40(1), pp.41-49.
 23. Caseri, W.R., Shelden, R.A. and Suter, U.W., 1992. Preparation of muscovite with ultrahigh specific surface area by chemical cleavage. *Colloid and Polymer Science*, 270(4), pp.392-398.
 24. Crandell, L.E., Ellis, B.R. and Peters, C.A., 2009. Dissolution potential of SO₂ co-injected with CO₂ in geologic sequestration. *Environmental science & technology*, 44(1), pp.349-355.
 25. Connell, L., Down, D., Lu, M., Hay, D. and Heryanto, D., 2015. An investigation

- into the integrity of wellbore cement in CO₂ storage wells: Core flooding experiments and simulations. *International journal of greenhouse gas control*, 37, pp.424-440.
26. Cubillas, P., Köhler, S., Prieto, M., Chaïrat, C. and Oelkers, E.H., 2005. Experimental determination of the dissolution rates of calcite, aragonite, and bivalves. *Chemical Geology*, 216(1-2), pp.59-77.
 27. Deng, S., Zuo, L., Aydin, A., Dvorkin, J. and Mukerji, T., 2015. Permeability characterization of natural compaction bands using core flooding experiments and three-dimensional image-based analysis: Comparing and contrasting the results from two different methods. *AAPG Bulletin*, 99(1), pp.27-49.
 28. Duan, Z. and Sun, R., 2003. An improved model calculating CO₂ solubility in pure water and aqueous NaCl solutions from 273 to 533 K and from 0 to 2000 bar. *Chemical geology*, 193(3-4), pp.257-271.
 29. Elkady, Y. and Kavscek, A.R., 2020. Multiscale study of CO₂ impact on fluid transport and carbonate dissolution in Utica and Eagle Ford shale. *Journal of Petroleum Science and Engineering*, p.107867.
 30. Erdem, M. and Özverdi, A., 2005. Lead adsorption from aqueous solution onto siderite. *Separation and Purification Technology*, 42(3), pp.259-264.
 31. Essaid, H.I., Bekins, B.A. and Cozzarelli, I.M., 2015. Organic contaminant transport and fate in the subsurface: Evolution of knowledge and understanding. *Water Resources Research*, 51(7), pp.4861-4902.
 32. Gautier, J.M., Oelkers, E.H. and Schott, J., 1994. Experimental study of K-feldspar dissolution rates as a function of chemical affinity at 150 C and pH 9. *Geochimica et Cosmochimica Acta*, 58(21), pp.4549-4560.
 33. Golubev, S.V., Bénézeth, P., Schott, J., Dandurand, J.L. and Castillo, A., 2009. Siderite dissolution kinetics in acidic aqueous solutions from 25 to 100 C and 0 to 50 atm pCO₂. *Chemical Geology*, 265(1-2), pp.13-19.
 34. Gouze, P. and Luquot, L., 2011. X-ray microtomography characterization of porosity, permeability and reactive surface changes during dissolution. *Journal of contaminant hydrology*, 120, pp.45-55.
 35. Guo, B., Ma, L. and Tchelepi, H.A., 2018. Image-based micro-continuum model for gas flow in organic-rich shale rock. *Advances in Water Resources*, 122, pp.70-84.
 36. Grandclerc, A., Dangla, P., Gueguen-Minerbe, M. and Chaussadent, T., 2018. Modelling of the sulfuric acid attack on different types of cementitious materials. *Cement and Concrete Research*, 105, pp.126-133.
 37. Gunter, W.D., Perkins, E.H. and Hutcheon, I., 2000. Aquifer disposal of acid gases: modelling of water-rock reactions for trapping of acid wastes. *Applied geochemistry*, 15(8), pp.1085-1095.
 38. Hellevang, H., Pham, V.T. and Aagaard, P., 2013. Kinetic modelling of CO₂-water-rock interactions. *International Journal of Greenhouse Gas Control*, 15, pp.3-15.
 39. la Cecilia, D., Riley, W.J. and Maggi, F., 2019. Biochemical modeling of microbial

- memory effects and catabolite repression on soil organic carbon compounds. *Soil Biology and Biochemistry*, 128, pp.1-12.
40. Kennedy, M.J., Pevear, D.R. and Hill, R.J., 2002. Mineral surface control of organic carbon in black shale. *Science*, 295(5555), pp.657-660.
 41. Knauss, K.G., 1989. Muscovite dissolution kinetics as a function of pH and time at 70 C. *Geochimica et Cosmochimica Acta*, 53(7), pp.1493-1501.
 42. Knauss, K.G. and Wolery, T.J., 1988. The dissolution kinetics of quartz as a function of pH and time at 70 C. *Geochimica et Cosmochimica Acta*, 52(1), pp.43-53.
 43. Kweon, H. and Deo, M., 2017. The impact of reactive surface area on brine-rock-carbon dioxide reactions in CO₂ sequestration. *Fuel*, 188, pp.39-49.
 44. Landrot, G., Ajo-Franklin, J.B., Yang, L., Cabrini, S. and Steefel, C.I., 2012. Measurement of accessible reactive surface area in a sandstone, with application to CO₂ mineralization. *Chemical Geology*, 318, pp.113-125.
 45. Lasaga, A.C., 1981. Transition state theory. *Rev. Mineral.; (United States)*, 8.
 46. Lasaga, A.C., 1984. Chemical kinetics of water-rock interactions. *Journal of geophysical research: solid earth*, 89(B6), pp.4009-4025.
 47. Li, L., Maher, K., Navarre-Sitchler, A., Druhan, J., Meile, C., Lawrence, C., Moore, J., Perdrial, J., Sullivan, P., Thompson, A. and Jin, L., 2017. Expanding the role of reactive transport models in critical zone processes. *Earth-science reviews*, 165, pp.280-301.
 48. Liu, P., Zhang, T. and Sun, S., 2019. A tutorial review of reactive transport modeling and risk assessment for geologic CO₂ sequestration. *Computers & geosciences*.
 49. Maher, K. and Navarre-Sitchler, A., 2019. Reactive transport processes that drive chemical weathering: From making space for water to dismantling continents. *Reviews in Mineralogy and Geochemistry*, 85(1), pp.349-380.
 50. Martens, E., Zhang, H., Prommer, H., Greskowiak, J., Jeffrey, M. and Roberts, P., 2012. In situ recovery of gold: Column leaching experiments and reactive transport modeling. *Hydrometallurgy*, 125, pp.16-23.
 51. Martinez, B.C., DeJong, J.T. and Ginn, T.R., 2014. Bio-geochemical reactive transport modeling of microbial induced calcite precipitation to predict the treatment of sand in one-dimensional flow. *Computers and Geotechnics*, 58, pp.1-13.
 52. Meakin, P. and Tartakovsky, A.M., 2009. Modeling and simulation of pore-scale multiphase fluid flow and reactive transport in fractured and porous media. *Reviews of Geophysics*, 47(3).
 53. Metz, V., Raanan, H., Pieper, H., Bosbach, D. and Ganor, J., 2005. Towards the establishment of a reliable proxy for the reactive surface area of smectite. *Geochimica et Cosmochimica Acta*, 69(10), pp.2581-2591.
 54. Miao, X., Wang, Y., Zhang, L., Wei, N. and Li, X., 2019. Improved Vinegar & Wellington calibration for estimation of fluid saturation and porosity from CT

- images for a core flooding test under geologic carbon storage conditions. *Micron*, 124, p.102703.
55. Morse, J.W. and Arvidson, R.S., 2002. The dissolution kinetics of major sedimentary carbonate minerals. *Earth-Science Reviews*, 58(1-2), pp.51-84.
 56. Morse, J.W., Arvidson, R.S. and Lüttge, A., 2007. Calcium carbonate formation and dissolution. *Chemical reviews*, 107(2), pp.342-381.
 57. Navarre-Sitchler, A., Steefel, C.I., Sak, P.B. and Brantley, S.L., 2011. A reactive-transport model for weathering rind formation on basalt. *Geochimica et Cosmochimica Acta*, 75(23), pp.7644-7667.
 58. Navarre-Sitchler, A. and Jung, H., 2017. Complex Coupling of Fluid Transport and Geochemical Reaction Rates: Insights from Reactive Transport Models. *Procedia Earth and Planetary Science*, 17, pp.5-8.
 59. Ng, G.H.C., Bekins, B.A., Cozzarelli, I.M., Baedeker, M.J., Bennett, P.C., Amos, R.T. and Herkelrath, W.N., 2015. Reactive transport modeling of geochemical controls on secondary water quality impacts at a crude oil spill site near Bemidji, MN. *Water Resources Research*, 51(6), pp.4156-4183.
 60. Nogues, J.P., Fitts, J.P., Celia, M.A. and Peters, C.A., 2013. Permeability evolution due to dissolution and precipitation of carbonates using reactive transport modeling in pore networks. *Water Resources Research*, 49(9), pp.6006-6021.
 61. Noiriel, C., Luquot, L., Madé, B., Raimbault, L., Gouze, P. and Van Der Lee, J., 2009. Changes in reactive surface area during limestone dissolution: An experimental and modelling study. *Chemical Geology*, 265(1-2), pp.160-170.
 62. Oelkers, E.H., Schott, J., Gauthier, J.M. and Herrero-Roncal, T., 2008. An experimental study of the dissolution mechanism and rates of muscovite. *Geochimica et Cosmochimica Acta*, 72(20), pp.4948-4961.
 63. Pallud, C., Meile, C., Laverman, A.M., Abell, J. and Van Cappellen, P., 2007. The use of flow-through sediment reactors in biogeochemical kinetics: methodology and examples of applications. *Marine Chemistry*, 106(1-2), pp.256-271.
 64. Papadopoulos, P. and Rowell, D.L., 1988. The reactions of cadmium with calcium carbonate surfaces. *Journal of Soil Science*, 39(1), pp.23-36.
 65. Peters, C.A., 2009. Accessibilities of reactive minerals in consolidated sedimentary rock: An imaging study of three sandstones. *Chemical Geology*, 265(1-2), pp.198-208.
 66. Pham, V.T.H., Lu, P., Aagaard, P., Zhu, C. and Hellevang, H., 2011. On the potential of CO₂-water-rock interactions for CO₂ storage using a modified kinetic model. *International Journal of Greenhouse Gas Control*, 5(4), pp.1002-1015.
 67. Pokrovsky, O.S., Golubev, S.V., Schott, J. and Castillo, A., 2009. Calcite, dolomite and magnesite dissolution kinetics in aqueous solutions at acid to circumneutral pH, 25 to 150 C and 1 to 55 atm pCO₂: New constraints on CO₂ sequestration in sedimentary basins. *Chemical geology*, 265(1-2), pp.20-32.
 68. Qajar, J., 2012. Reactive Flow in Carbonate Cores via Digital Core Analysis.
 69. Qajar, J. and Arns, C.H., 2016. Characterization of reactive flow-induced evolution

- of carbonate rocks using digital core analysis-part 1: Assessment of pore-scale mineral dissolution and deposition. *Journal of contaminant hydrology*, 192, pp.60-86.
70. Qin, F. and Beckingham, L.E., 2019. Impact of image resolution on quantification of mineral abundances and accessible surface areas. *Chemical Geology*, 523, pp.31-41.
 71. Raines, M. and Dewers, T., 1997. "Mixed" kinetics control of fluid-rock interaction in reservoir production scenarios. *Journal of Petroleum Science and Engineering*, 17(1-2), pp.139-155.
 72. Salehikhoo, F., Li, L. and Brantley, S.L., 2013. Magnesite dissolution rates at different spatial scales: The role of mineral spatial distribution and flow velocity. *Geochimica et Cosmochimica Acta*, 108, pp.91-106.
 73. Scheibe, T.D., Mahadevan, R., Fang, Y., Garg, S., Long, P.E. and Lovley, D.R., 2009. Coupling a genome-scale metabolic model with a reactive transport model to describe in situ uranium bioremediation. *Microbial biotechnology*, 2(2), pp.274-286.
 74. Schmidt, M.J., Pankavich, S.D., Navarre-Sitchler, A. and Benson, D.A., 2019. A Lagrangian method for reactive transport with solid/aqueous chemical phase interaction. *Journal of Computational Physics: X*, 2, p.100021.
 75. Schmidt, M.J., Pankavich, S.D., Navarre-Sitchler, A., Engdahl, N.B., Bolster, D. and Benson, D.A., 2019. Reactive Particle-tracking Solutions to a Benchmark Problem on Heavy Metal Cycling in Lake Sediments. 2019arXiv190809818S.
 76. Sen, T.K. and Khilar, K.C., 2006. Review on subsurface colloids and colloid-associated contaminant transport in saturated porous media. *Advances in colloid and interface science*, 119(2-3), pp.71-96.
 77. Shan, Y. and Guo, H., 2013. Fluoride adsorption on modified natural siderite: Optimization and performance. *Chemical engineering journal*, 223, pp.183-191.
 78. Shultz, C.D., Bailey, R.T., Gates, T.K., Heesemann, B.E. and Morway, E.D., 2018. Simulating selenium and nitrogen fate and transport in coupled stream-aquifer systems of irrigated regions. *Journal of Hydrology*, 560, pp.512-529.
 79. Steefel, C.I., Appelo, C.A.J., Arora, B., Jacques, D., Kalbacher, T., Kolditz, O., Lagneau, V., Lichtner, P.C., Mayer, K.U., Meeussen, J.C.L. and Molins, S., 2015. Reactive transport codes for subsurface environmental simulation. *Computational Geosciences*, 19(3), pp.445-478.
 80. Steefel, C.I., DePaolo, D.J. and Lichtner, P.C., 2005. Reactive transport modeling: An essential tool and a new research approach for the Earth sciences. *Earth and Planetary Science Letters*, 240(3-4), pp.539-558.
 81. Steefel, C.I., Molins, S. and Trebotich, D., 2013. Pore scale processes associated with subsurface CO₂ injection and sequestration. *Reviews in Mineralogy and Geochemistry*, 77(1), pp.259-303.
 82. Steefel, C., 2018. *Reactive Transport Modeling: Applications in Subsurface Energy and Environmental Problems*. John Wiley & Sons.

83. Tester, J.W., Worley, W.G., Robinson, B.A., Grigsby, C.O. and Feerer, J.L., 1994. Correlating quartz dissolution kinetics in pure water from 25 to 625 C. *Geochimica et Cosmochimica Acta*, 58(11), pp.2407-2420.
84. Van Hees, P.A.W., Lundström, U.S. and Mörth, C.M., 2002. Dissolution of microcline and labradorite in a forest O horizon extract: the effect of naturally occurring organic acids. *Chemical Geology*, 189(3-4), pp.199-211.
85. White, A.F. and Peterson, M.L., 1990. Role of reactive-surface-area characterization in geochemical kinetic models.
86. White, S.P., Allis, R.G., Moore, J., Chidsey, T., Morgan, C., Gwynn, W. and Adams, M., 2005. Simulation of reactive transport of injected CO₂ on the Colorado Plateau, Utah, USA. *Chemical geology*, 217(3-4), pp.387-405.
87. Xu, T., Kharaka, Y.K., Doughty, C., Freifeld, B.M. and Daley, T.M., 2010. Reactive transport modeling to study changes in water chemistry induced by CO₂ injection at the Frio-I Brine Pilot. *Chemical Geology*, 271(3-4), pp.153-164.
88. Yabusaki, S.B., Fang, Y., Williams, K.H., Murray, C.J., Ward, A.L., Dayvault, R.D., Waichler, S.R., Newcomer, D.R., Spane, F.A. and Long, P.E., 2011. Variably saturated flow and multicomponent biogeochemical reactive transport modeling of a uranium bioremediation field experiment. *Journal of contaminant hydrology*, 126(3-4), pp.271-290.
89. Yang, Y., Bruns, S., Stipp, S.L.S. and Sørensen, H.O., 2018. Impact of microstructure evolution on the difference between geometric and reactive surface areas in natural chalk. *Advances in water resources*, 115, pp.151-159.

Chapter 4. Estimation of mineral accessible surface area from mineral abundance and clay content

Fanqi Qin, Md. Fahim Salek, Parisa Asadi, Chidera Iloejesi, Olivia Brunhoeber, Michael Kiernan, Mukseet Mahmood, Lauren, E. Beckingham*

Department of Civil and Environmental Engineering, Auburn University

*leb@auburn.edu

Manuscript in preparation.

4.1 Introduction

Geochemical reactions occur in a variety of environmental systems, such as chemical weathering on the surface of the earth (Mahdikhani et al., 2018; White and Brantley, 2018; Cao et al., 2019; Yu et al., 2019; Chen et al., 2020), CO₂-brine-mineral interactions in carbon capture and storage (CCS) systems (Navarre-Sitchler et al., 2011; Ng et al., 2015; Cui et al., 2018; March et al., 2018; Snæbjörnsdóttir et al., 2017 and 2018; Bensinger and Beckingham, 2020; Qin and Beckingham, 2021) as well as enhanced oil recovery (Jia and Sheng, 2018; Esene et al., 2019; Gbadamosi et al., 2019; Khurshid, 2021) and subsurface energy storage systems (Kabuth et al., 2017; Fleming et al., 2018; Iloejesi and Beckingham, 2020; Koochi-Fayegh and Rosen, 2020). These reactions are rather complex as the natural environmental systems are often multi-phased systems with varying conditions. For example, the CO₂ induced geochemical reactions in subsurface systems are impacted by many factors such as injection rate, formation depth, porosity, permeability and mineral composition, etc.

Reactive transport modeling is a powerful tool that has been used to simulate these complex geochemical reactions over laboratory and geological timescales (Steeffel et al., 2005, 2013; Pallud et al., 2007; Boana et al., 2014; Li et al., 2017; Steefel, 2018; Maher and Navarre-Sitchler, 2019). To better estimate the rate and extent of the reactions and predict the potential impact of these geochemical reactions on the formation properties (e.g. porosity, permeability), it is essential to have a good understanding of the controlling parameters of the reactions, such as mineral abundance, mineral surface area, pore connectivity, etc. Transition state theory (TST) (Lasaga, 1981, 1984; Aagaard and Helgeson, 1982) is commonly used to calculate mineral reaction rates:

$$R_m = A_m k_m [f \Delta G_r] \quad (1)$$

where A_m represent mineral reactive surface area, k_m is the mineral rate constant, and $f \Delta G_r$ is the thermodynamic driving force for the reaction (Steeffel et al., 2015). Thermodynamic parameters and rate constants are often obtained from a

thermodynamic database, while the mineral porosity, abundance, surface areas are usually measured. For instance, X-ray diffraction (XRD) is commonly used to determine the mineral composition (abundance) of a sample, while mineral specific surface area can be measured through the traditional Brunauer–Emmett–Teller (BET) adsorption method (Brunauer et al., 1938). However, the detection limit of X-ray diffraction (0.33% - 5%) (O'Connell and Regalbuto, 2015) can result in neglect of minor mineral phases. For example, clay content varies among different sandstone samples, and it is challenging to quantify clay abundance through XRD analysis. Clay minerals play an important role on pore connectivity and mineral accessibility as they are commonly present as a coating or bridging phases on/between the surface of other mineral grains (Storvoll et al., 2002; Griffiths et al., 2018; Tang et al., 2018; Wooldridge et al., 2019; Busch, 2020). The BET adsorption method provides good estimation of mineral specific surface area (SSA). However, estimating the specific surface area for each mineral in a multi-mineralic sample is challenging and requires analysis of pure mineral phases as discerning the specific surface area of each mineral phase with multiple minerals present is not feasible. Moreover, the measured BET specific surface areas of pure mineral phases vary widely (Black et al., 2015; Bourg et al., 2015).

Imaging has emerged as a relatively new approach for mineral property quantification (Peters, 2009; Landrot et al. 2012; Beckingham et al., 2016 and 2017; Qin and Beckingham, 2019; Ma et al., 2021). Beckingham et al., 2017 found that simulations carried out using mineral accessible surface areas (ASA) quantified from imaging match the reaction rates observed in core-flood experiments more closely than simulations that use specific surface area. In addition, imaging has the advantage of quantifying mineral phases with abundances less than the XRD detection limit. Although the abundance and accessible mineral surface area quantified from imaging is informative for reactive transport modeling, the time and resources involved in the process from sample preparation, image acquisition and image segmentation to mineral properties quantification can be enormous. Resources may be somewhat reduced by capturing images at lower resolutions where varying impact resolution from 0.3 to 5.7 microns was found to have minor impacts on measured mineral volume fractions and accessible surface areas (within one order of magnitude) (Qin and Beckingham, 2019, 2020). In addition, scanning electron microscopy imaging is inherently destructive, requiring samples to be polished and cut into thin sections for higher image quality (Xiong et al., 2016). Therefore, it is not feasible to compare changes occurring on the exact same location where the images are captured before and after reactions, for example. In this work, we aim to evaluate the potential pattern and relationships among measured mineral properties determined from imaging for various sandstone samples. Mineral abundance, accessibility, accessible surface area, clay content and connected surface area are quantified and then compared and their connections, as well as their individual impact on other properties, considered. Through analysis of these relationships, we aim to be able to estimate and predict mineral accessibility as well as surface area for various samples without having to go through the complicated image

acquisition and segmentation process.

4.2 Materials and Methods

Seven sandstone samples are analyzed through SEM imaging, X-ray nano-CT imaging and image processing in this work. Results from three additional samples previously considered in the literature are also considered here for comparison. This includes a Paluxy sandstone sample studied in Qin and Beckingham (2019), collected from the pilot CO₂ injection site at Kemper County, Mississippi, U.S. (Riestenberg et al., 2018), one Lower Tuscaloosa sample studied in Landrot et al. (2012), collected from a geologic carbon sequestration pilot site in Cranfield, Mississippi (well CFU 31-F2), and another sample extracted from the geothermal well (Vydmantai-1) at a depth of 954.6 m, located at the southeast end of the Baltic Sea in Lithuania (Ma et al., 2021). Sample characteristics and imaging methodologies are described in the following sections.

4.2.1 Sample characterization and preparation

Five sandstone core samples were obtained from Kocurek Industries from the Bandera Grey, Bandera Brown, Bentheimer, Kentucky and Leopard formations. One Lower Tuscaloosa and one Paluxy sandstone sample were obtained from the Geological Survey of Alabama. Sample preparations were performed at Applied Petrographic Services, Inc. (Westmoreland, Pennsylvania), samples purchased from Kocurek Industries were cut into thick sections (0.5 cm thickness) and samples from Geological Survey of Alabama were made into thin sections, all samples were impregnated with epoxy and polished. To prepare for SEM imaging, a conductive carbon coating was applied to each thin section using EMS 550× Sputter Coating Device at Auburn University.

All ten samples considered in this work are sandstone, mainly composed of quartz (66% - 94%), with various amount of feldspars, carbonate and clay minerals as well as trace amount of other mineral species. Porosity of these samples varies from 0.14 to 0.24 (Table 1) (Landrot et al., 2012; Qin and Beckingham, 2019; Ma et al., 2021).

4.2.2 Imaging acquisition and mineral properties quantification

Mineral properties including porosity, mineral abundance, accessibility and accessible surface area were quantified from 2D BSE and 3D nano-CT images. SEM backscatter electron (BSE) images of the seven samples were captured using a ZEISS EVO 50VP Scanning Electron Microscope at Auburn University. Carbon – coated thin sections were imaged under high vacuum mode while the uncoated thick sections were imaged under variable pressure mode. Energy dispersive X-ray spectrometry (EDS) elemental maps were also obtained to help identify mineral phases. Pore-grain segmentation was performed manually in ImageJ. Additional processing and mineral segmentation of the images followed the approach used in Landrot et al., 2012 and

Beckingham et al., 2016. Briefly, SEM BSE images were first manually thresholded in ImageJ. SEM EDS elemental maps were enhanced with filters and custom noise reduction Matlab codes before identifying minerals based on elemental maps and grayscale intensity in SEM BSE images. Each pixel was then assigned to a specific mineral and expressed as a unique color in the processed mineral map. This part of the processing was performed in Matlab (original code modified for each image) and ImageJ.

Following image segmentation, mineral abundances were calculated by counting mineral pixels with the same color, while mineral accessibilities were calculated by counting mineral pixels that are adjacent to pore pixels. Mineral abundance refers to the volume fraction of each mineral phase and mineral accessibility refers to the percentage of each mineral's surface that is adjacent to the pores. Here, both accessibility that only accounts for the connected pore space and that assumes all pores are connected are considered and calculated.

3D X-ray computed nanotomography (X-ray nano-CT) images were taken using a ZEISS Xradia 620 Versa 3D X-ray Microscope at Auburn University. The reconstructed 3D nano-CT images were used to calculate the total connected surface area. This is accomplished by first segmenting the images into grain and pore voxels. Randomly sampled sub-cubes with the same total area as the corresponding 2D SEM BSE image were then sampled from the larger 3D image. The connected surface area of these cubes was then identified and calculated using a marching cubes algorithm in Matlab with a mesh applied to the grain voxels. Ten of these sub-cubes were randomly selected and analyzed to obtain average values of connected surface area. The average connected surface areas were then multiplied by the mineral accessibility calculated from 2D SEM BSE images to estimate the mineral accessible surface areas (Landrot et al., 2012).

A correction factor (CF) is also needed when there is large difference in the resolution of the SEM BSE and nano-CT images. The correction factor was determined by first reducing the image resolution of the BSE images in ImageJ to match with the resolution of the nano-CT images, and then counting the number of connected interfacial pixels in the two images. The correction factor is calculated as,

$$\text{Correction factor } (CF) = \frac{P_{original}}{P_{reduced}}$$

where $P_{original}$ and $P_{reduced}$ refer to the total number of connected interfacial pixels in the original high resolution 2D SEM BSE images and in the resolution-reduced 2D SEM BSE images, respectively. The corrected total connected surface area was then calculated by multiplying the connected surface area measured from 3D nano-CT images with correction factor.

4.3 Results

4.3.1 Image processing and mineral property quantification

In this section, the SEM BSE images and the mineral phase segmented maps of these images are presented. Quantified mineral properties including porosity, mineral abundance, accessibility and accessible surface area are reported in Table 4.1. The accessible surface area of clay minerals, or minerals with many small scale features (e.g. muscovite), cannot be directly measured from these images, and therefore are not reported here.

4.3.1.1 Lower Tuscaloosa

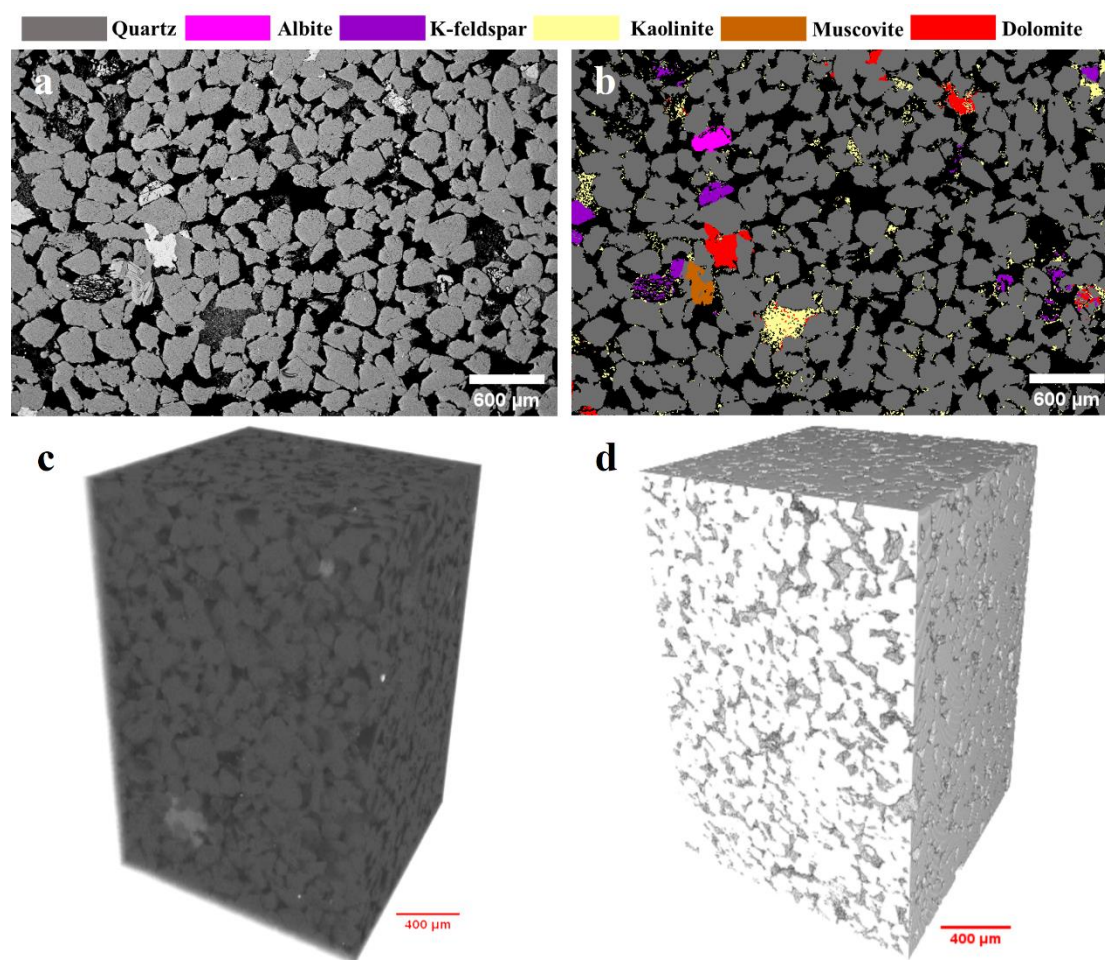


Figure 4. 1 a) 2D SEM BSE image of sample collected from Lower Tuscaloosa formation (Provided by The Geological Survey of Alabama), captured under a resolution of 5.26 μm , covering an area of 12.00 mm^2 ; b) mineral phase segmented map; c) reconstructed 3D nano-CT image with a voxel size of 4.53 μm ; d) thresholded 3D nano-CT image with pores depicted in black and grains in white.

BSE images and the resulting processed mineral map for the Lower Tuscaloosa sandstone are shown in Figure 4.1. In the processed mineral map, each color

corresponds to a different mineral phase. The mineral abundances and accessibilities, determined from pixel counting, are given in Table 4.1. In terms of mineral abundance, this sample is comprised of over 92% quartz with 3.67% kaolinite. The abundances of other mineral phases are all below 2%. The porosity is calculated to be 33%. The accessibility of quartz is over 83%, which is less than its abundance. Conversely, the accessibility of kaolinite, the major clay mineral, is 13.41%, significantly higher than reflected by its abundance. The accessibilities of other 4 mineral phases are all below 2%, consistent with their abundances. There is a difference of two orders of magnitude variation between the calculated mineral accessible surface areas for different mineral phases. The accessible surface area of quartz is calculated to be $3.11\text{E-}01 \text{ m}^2/\text{g}$, while the accessible surface areas of K-feldspar, albite and dolomite are $5.48\text{E-}03$, $1.49\text{E-}03$ and $4.37\text{E-}03 \text{ m}^2/\text{g}$, respectively.

4.3.1.2 Bandera Brown:

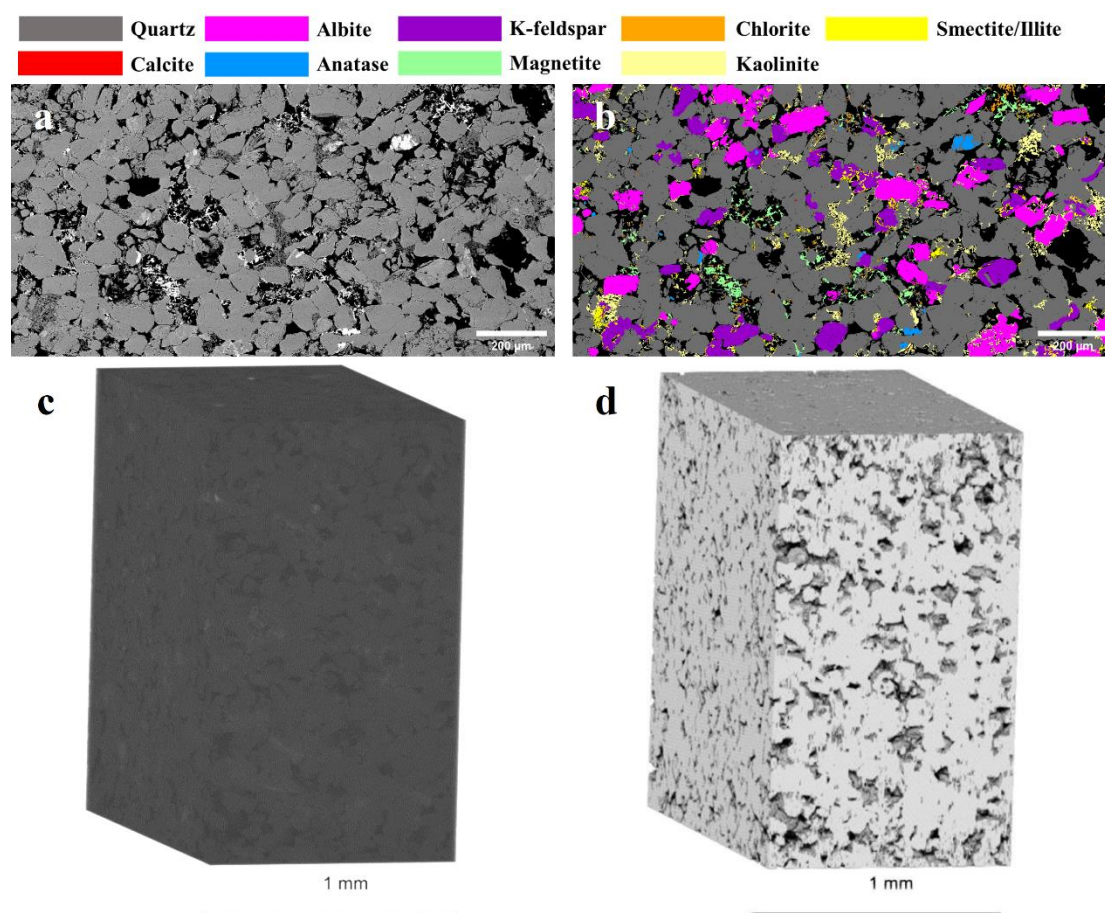


Figure 4. 2. a) SEM BSE image of the sample collected from Bandera Brown formation, captured under a resolution of $0.77 \mu\text{m}$, covering an area of 1.18 mm^2 ; b) mineral phase segmented map; c) reconstructed 3D nano-CT image with a voxel size of $1.36 \mu\text{m}$; d) thresholded nano-CT image with pores in black and grains in light grey.

In the SEM BSE image of Bandera Brown sample (Figure 4.2a), a total of nine minerals have been identified. The identified minerals were mapped in Figure 4.2b. The abundance of quartz is 73.48%, with 8.33% of K-feldspar and 10.24% albite. There are

three clay minerals – kaolinite, illite and chlorite with a total abundance of 5.96%. The abundance of anatase and calcite is 0.47% and 0.007%, respectively. The porosity is calculated to be 21%. Quartz has the highest accessibility (69.44%) among all nine mineral phases and is close to the quartz abundance. Two feldspar minerals – K-feldspar and albite have higher abundances than clay minerals (kaolinite, illite and chlorite), however, the accessibility of clay minerals is higher (Table 4.1). Calcite only has 0.007% abundance and it is embedded in quartz grains, therefore its accessibility is 0%. The calculated accessible surface areas vary up to 3 orders of magnitude. The accessible surface area of quartz is $5.07\text{E-}02 \text{ m}^2/\text{g}$, while the accessible surface area of feldspars and magnetite are approximately one order of magnitude lower than quartz: K-feldspar ($1.80\text{E-}03 \text{ m}^2/\text{g}$), albite ($3.00\text{E-}03 \text{ m}^2/\text{g}$), magnetite ($2.60\text{E-}03 \text{ m}^2/\text{g}$). Anatase has the lowest accessible surface area here ($8.00\text{E-}05 \text{ m}^2/\text{g}$).

4.3.1.3 Leopard:

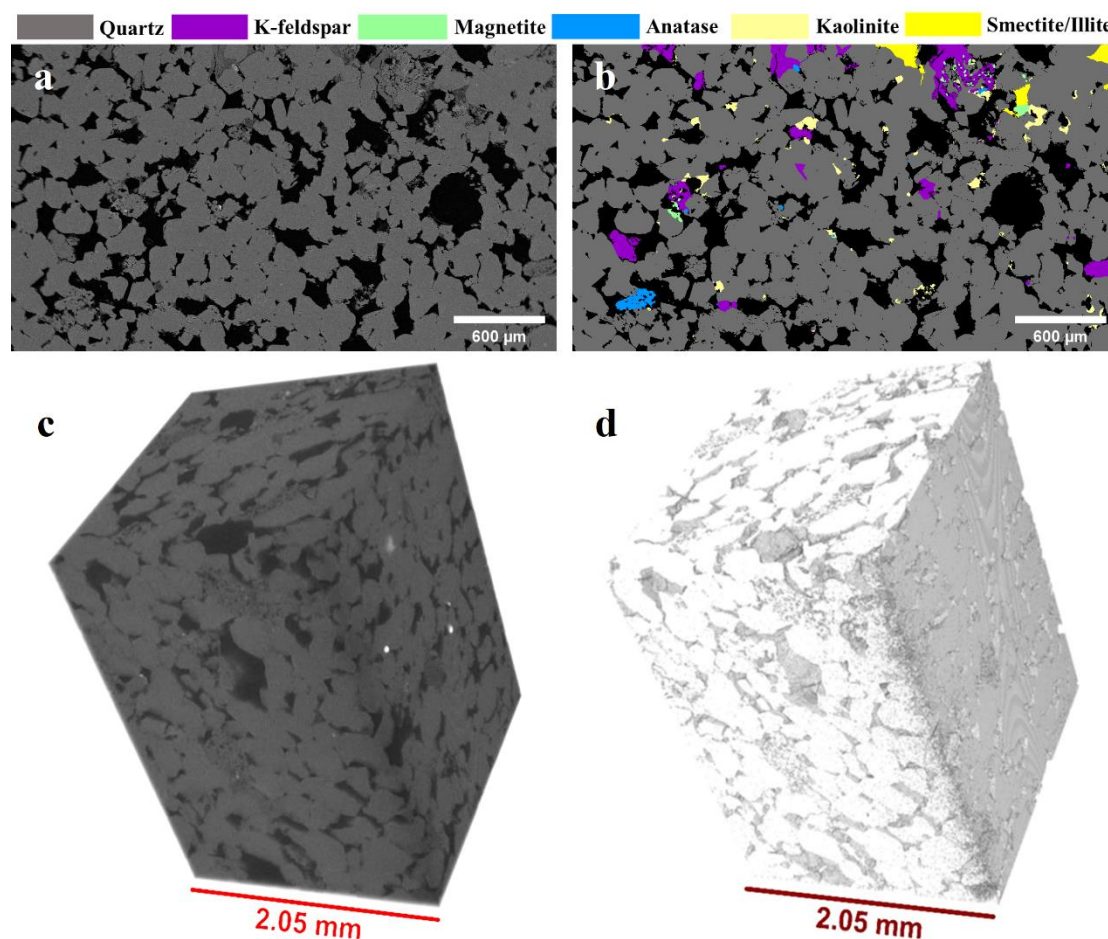


Figure 4. 3. a) SEM BSE image of sample collected from Leopard formation, captured under a resolution of $3.50 \mu\text{m}$, covering an area of 7.21 mm^2 ; b) mineral phase segmented map; c) reconstructed 3D nano-CT image with a voxel size of $1.49 \mu\text{m}$; d) thresholded 3D nano-CT image with pores in black and grains in white.

The SEM BSE image of the Leopard sample is shown in Figure 4.3a. Seven mineral phases have been identified in the area of interest (Figure 4.3b). Quartz has over 93%

abundance, followed by K-feldspar (3.73%) and kaolinite (1.37%), while other mineral species have abundances less than 1%. The accessibility of quartz is 88.84%, while the accessibility of kaolinite and K-feldspar is 4.91% and 5.52%, respectively. The porosity determined from the SEM BSE image is 23%. A small fraction of anatase is found in the image, however, they are not accessible to the connected pores. The calculated accessible surface areas vary up to 4 orders of magnitude. Quartz has the highest accessible surface area ($1.37\text{E}-02 \text{ m}^2/\text{g}$) among the mineral species identified from the SEM BSE image. The accessible surface areas of K-feldspar and magnetite are $8.50\text{E}-04 \text{ m}^2/\text{g}$ and $5.34\text{E}-06 \text{ m}^2/\text{g}$, respectively.

4.3.1.4 Bentheimer:

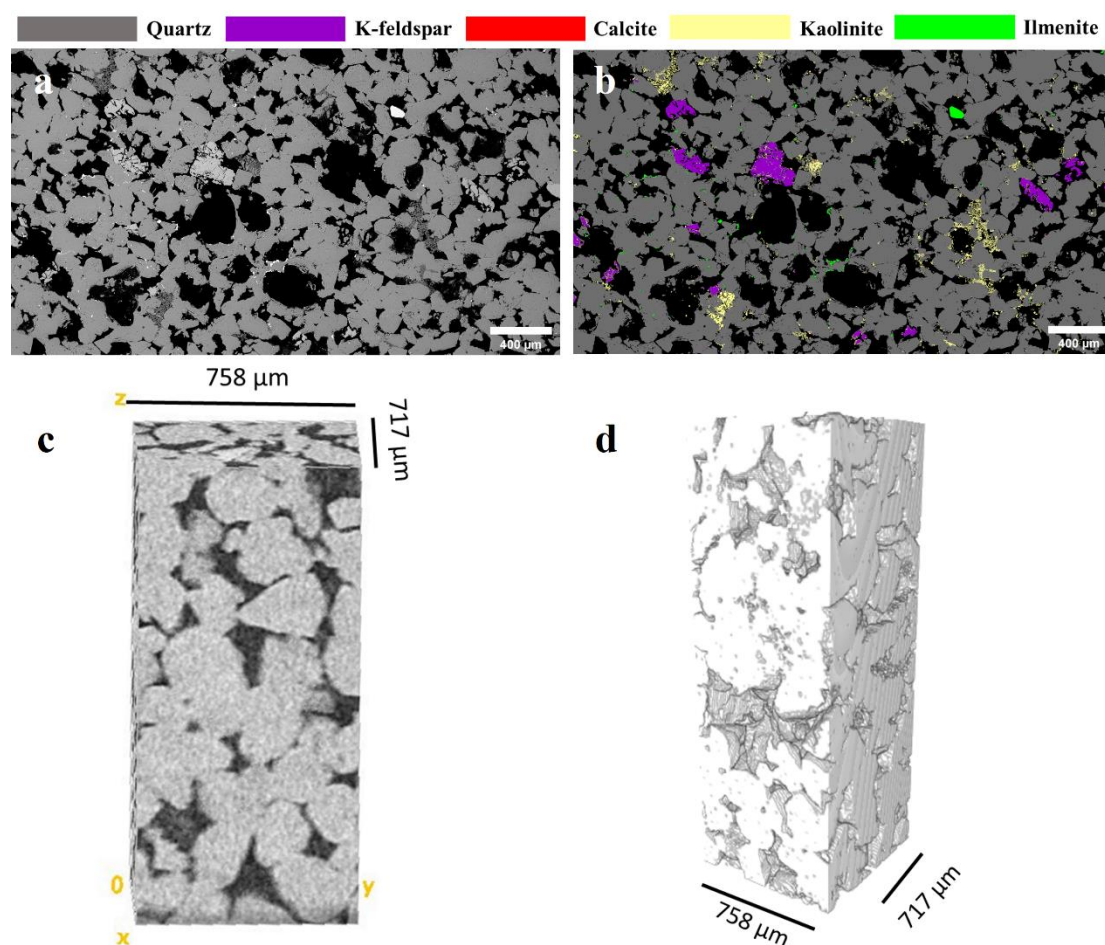


Figure 4. 4. a) SEM BSE image of sample collected from Bentheimer formation, captured under a resolution of $1.23 \mu\text{m}$, covering an area of 7.00 mm^2 . b) mineral phase segmented map; c) reconstructed 3D nano-CT image with a voxel size of $3.98 \mu\text{m}$; d) thresholded CT image with pores shown in black and grains in white.

There are six mineral species identified in the BSE image of Bentheimer sample (Figure 4.4). Quartz takes more than 95% abundance, 2.7% is K-feldspar, 1.64% is kaolinite and the rest minerals have abundances less than 1%. The porosity is calculated to be 32.65%. Among all the mineral surfaces that are accessible to connected pores,

79.1% are quartz, which is less than the abundance of quartz. 16.7% of accessible surfaces if kaolinite, which is significantly higher than the relative abundance of kaolinite. 4.15% of the accessible mineral surface is comprised of K-feldspar and other mineral species have accessibility less than 0.01%. The estimated accessible surface areas vary up to 5 orders of magnitude, with quartz having the highest accessible surface area ($1.47\text{E-}02 \text{ m}^2/\text{g}$). The accessible surface area of K-feldspar, albite and calcite are $7.70\text{E-}04 \text{ m}^2/\text{g}$, $1.67\text{E-}06 \text{ m}^2/\text{g}$ and $3.71\text{E-}07 \text{ m}^2/\text{g}$, respectively.

4.3.1.5 Kentucky:

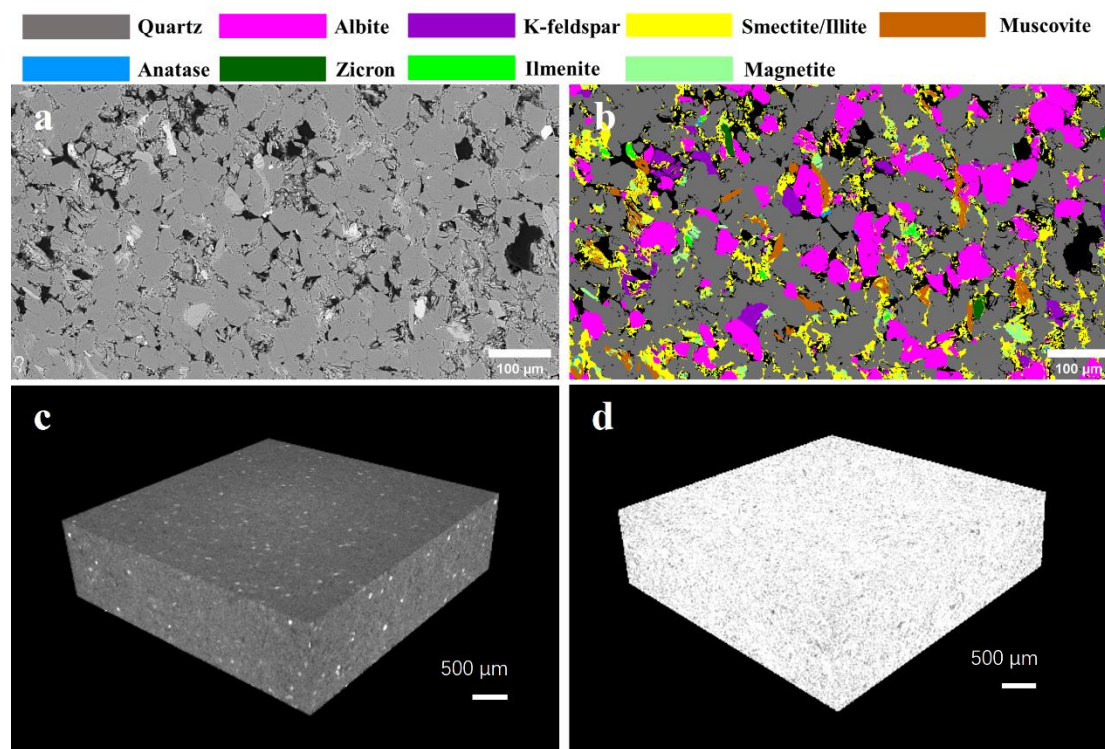


Figure 4. 5. a) the BSE image of sample collected from Bentheimer formation, captured under a resolution of $0.44 \mu\text{m}$, covering an area of 0.41 mm^2 . b) mineral phase segmented map; c) reconstructed 3D nano-CT image with a voxel size of $2.77 \mu\text{m}$; d) thresholded 3D nano-CT image with pores depicted in black and grains in white.

The original and processed images for the Kentucky sandstone sample are shown in Figure 4.5. Among the ten samples considered in this work, the Kentucky sandstone sample has the lowest porosity. The porosity calculated from the BSE image (Figure 4.5a) is 13.25%. Nine mineral species have been identified from Figure 4.5a and mapped in Figure 4.5b. Quartz is the most dominant phase with over 62% abundance, followed by albite (16.79%) and clay mineral – illite (11.73%), K-feldspar and hematite both have around 2.6% abundance, while the abundances of other mineral phases are all lower than 1%. As for accessibility, illite has the highest accessibility – 49.95%, which is significantly higher than the abundance of illite. The accessibilities of quartz and albite are 33.27% and 13.89%, respectively, which is less than the abundance of quartz but similar to the abundance of albite. Around two orders of magnitude variations

in the accessible surface area are observed. The accessible surface area of quartz is calculated to be $7.46\text{E-}02 \text{ m}^2/\text{g}$, followed by albite ($3.11\text{E-}02 \text{ m}^2/\text{g}$), the accessible surface areas of other mineral phases are 1-2 orders of magnitude lower, from high to low are: magnetite ($3.82\text{E-}03 \text{ m}^2/\text{g}$), ilmenite ($1.13\text{E-}03 \text{ m}^2/\text{g}$), K-feldspar ($6.10\text{E-}04 \text{ m}^2/\text{g}$), and anatase ($1.17\text{E-}04 \text{ m}^2/\text{g}$). zircon is not accessible to the connected pore space, therefore, the accessible surface area of zircon is 0.

4.3.1.6 Paluxy:

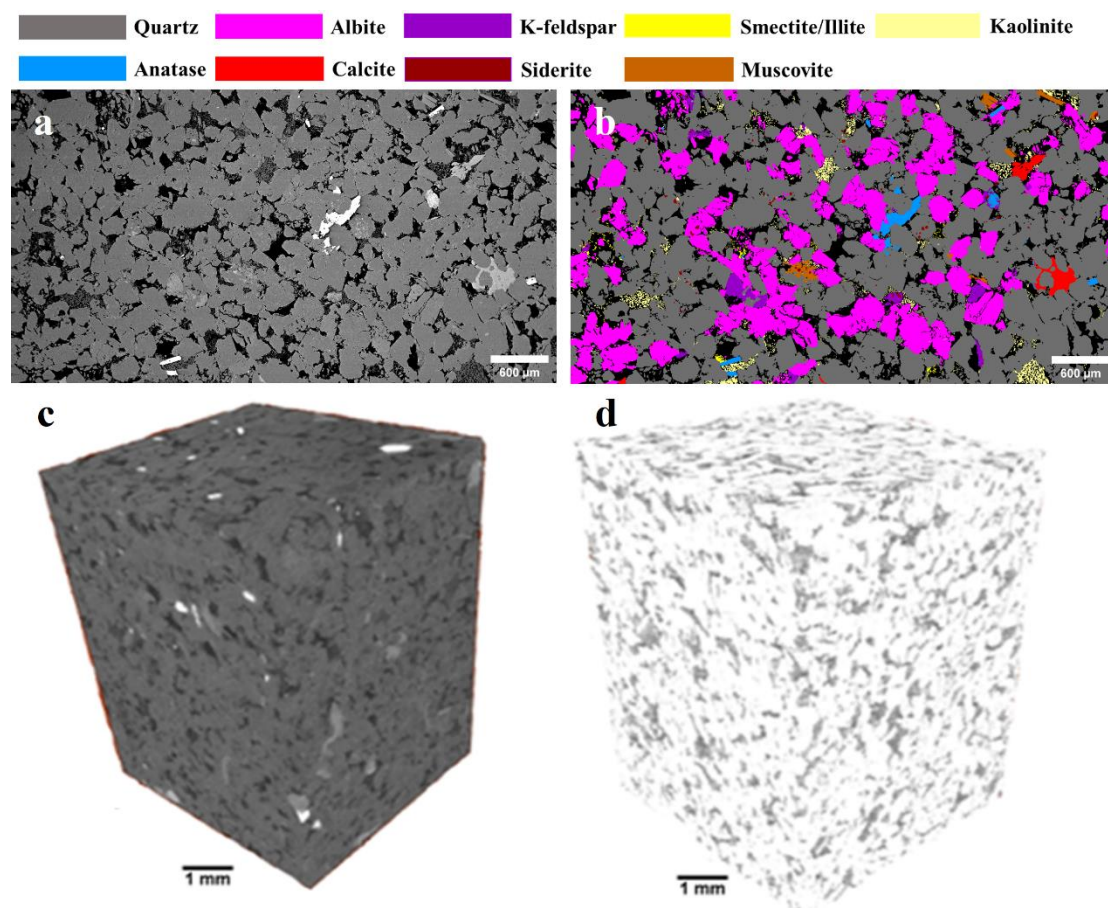


Figure 4. 6. a) the BSE image of sample collected from Paluxy formation (Provided by The Geological Survey of Alabama), captured under a resolution of $1.90 \mu\text{m}$, covering an area of 17.14 mm^2 . b) mineral phase segmented map; c) reconstructed 3D nano-CT image with a voxel size of $5.8 \mu\text{m}$; d) thresholded 3D nano-CT image with pores depicted in black and grains in white.

The original and processed images from the Paluxy sandstone are shown in Figure 4.6. Nine minerals are identified in the BSE image including quartz, whose abundance is 69.31%, albite whose abundance is 24.50% and 1.21% K-feldspar. The abundances of the two clay minerals – kaolinite and smectite are 2.26% and 0.24%, respectively. Other mineral phases are all less than 1%. Porosity calculated from the BSE image is 19%. Quartz has 52% accessibility among the nine mineral species, followed by albite (20%) and kaolinite (24.40%). The accessibility of kaolinite is significantly higher than reflected by the abundance of kaolinite. Accessibilities of other mineral phases are all

below 1.5%. There are 2 orders of magnitude variations in the estimated accessible surface areas, the accessible surface area of quartz and albite are $7.57\text{E-}02 \text{ m}^2/\text{g}$ and $2.91\text{E-}02 \text{ m}^2/\text{g}$, respectively. For other mineral species, the accessible surface areas from high to low are: K-feldspar ($1.40\text{E-}03 \text{ m}^2/\text{g}$), siderite ($5.43\text{E-}04 \text{ m}^2/\text{g}$), calcite ($2.10\text{E-}04 \text{ m}^2/\text{g}$) and anatase ($2.02\text{E-}04 \text{ m}^2/\text{g}$).

4.3.1.7 Bandera Grey:

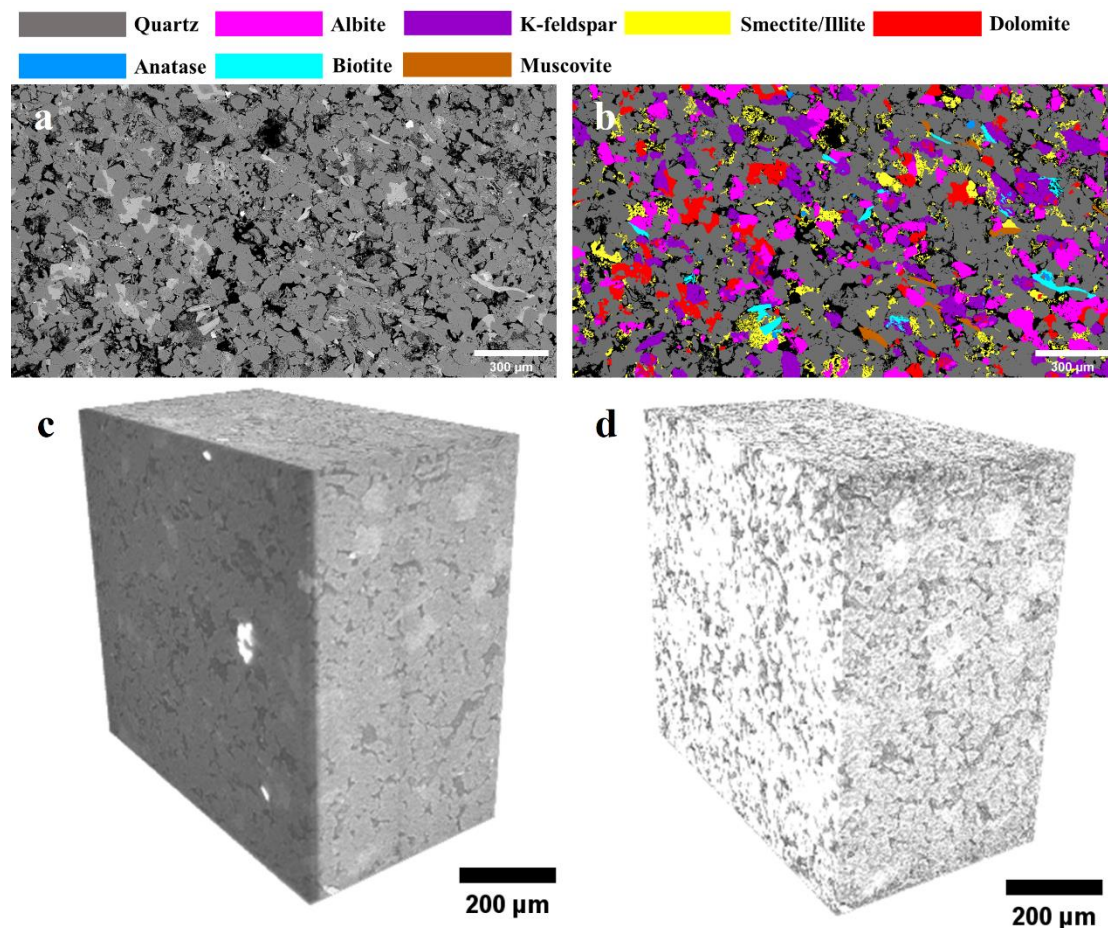


Figure 4. 7. a) the BSE image of sample collected from Bandera Grey formation, captured under a resolution of $0.71 \mu\text{m}$, covering an area of 2.60 mm^2 . b) mineral phase segmented map; c) reconstructed 3D nano-CT image with a voxel size of $2.0 \mu\text{m}$; d) thresholded 3D nano-CT image with pores shown in black and grains in white.

The mineral phase segmented map of the Bandera Grey sandstone sample is shown in Figure 4.7b. It is predominately comprised of quartz – 63.46% abundance, two feldspar minerals – K-feldspar and albite with abundances of 12.12% and 10.22%, respectively. The abundance of calcite is 5.69% and illite is 6.39%. Abundances of other mineral species are all below 1.2%. The calculated porosity from the BSE image is 15%. Quartz has the highest accessibility (60.91%) among 8 mineral phases, followed by clay mineral – illite (26.09%). The accessibility of K-feldspar and albite are 5.59% and 6.59%, respectively. Two mica mineral – muscovite and biotite are also present in the area of interest, however, due to low pore connectivity, the accessibility and their

corresponding accessible surface area are zero. Variations in the calculated accessible surface areas are up to 3 orders of magnitude. Quartz has the highest accessible surface areas among the 8 mineral phases, with a value of $3.32\text{E-}02 \text{ m}^2/\text{g}$, followed by the two feldspar minerals – K-feldspar ($3.05\text{E-}03 \text{ m}^2/\text{g}$) and albite ($3.59\text{E-}03 \text{ m}^2/\text{g}$). The accessible surface area of calcite and anatase are $3.90\text{E-}04 \text{ m}^2/\text{g}$ and $5.65\text{E-}05 \text{ m}^2/\text{g}$, respectively.

Table 4.1 Mineral properties including mineral abundances, accessibilities, accessible surface areas quantified from 2D SEM BSE images and 3D nao-CT images. The surface area of clay minerals (kaolinite, smectite, illite and chlorite) and muscovite cannot be directly quantified from the resolutions of the images obtained.

Formation	Mineral	Abundance (%)	Accessibility (%)	Accessible surface area (m^2/g)
Bandera Brown	Quartz	73.48	69.44	$5.07\text{E-}02$
	K-feldspar	8.33	2.48	$1.80\text{E-}03$
	Albite	10.24	4.17	$3.00\text{E-}03$
	Calcite	0.01	0.00	$0.00\text{E+}00$
	Kaolinite	4.31	12.88	NA
	Illite	1.17	2.74	NA
	Chlorite	0.48	4.54	NA
	Anatase	0.47	0.12	$8.00\text{E-}05$
Lower Tuscaloosa	Magnetite	1.49	3.63	$2.60\text{E-}03$
	Quartz	92.03	83.33	$3.11\text{E-}01$
	K-feldspar	1.58	1.47	$5.48\text{E-}03$
	Muscovite	0.53	0.22	NA
	Kaolinite	3.67	13.41	NA
	Dolomite	1.48	1.17	$4.37\text{E-}03$
Leopard	Albite	0.49	0.40	$1.49\text{E-}03$
	Quartz	93.11	88.84	$1.37\text{E-}02$

	Kaolinite	1.37	4.91	NA
	K-feldspar	3.76	5.52	8.50E-04
	Magnetite	0.31	0.03	5.34E-06
	Smectite/Illite	1.07	0.69	NA
	Anatase	0.46	0.00	0.00E+00
Bentheimer	Quartz	95.32	79.10	1.47E-02
	Albite	0.01	0.01	1.67E-06
	K-feldspar	2.70	4.15	7.70E-04
	Kaolinite	1.64	16.70	NA
	Calcite	0.00	0.00	3.71E-07
	Ilmenite	0.40	0.00	0.00E+00
Kentucky	Quartz	62.58	33.27	7.46E-02
	Albite	16.79	13.89	3.11E-02
	K-feldspar	2.92	0.27	6.10E-04
	Illite	11.73	49.95	NA
	Ilmenite	0.29	0.50	1.13E-03
	Magnetite	2.60	1.70	3.82E-03
	Anatase	0.17	0.05	1.17E-04
	Zircon	0.37	0.00	0.00E+00
	Muscovite	2.55	0.36	NA
Paluxy	Quartz	69.31	52.00	7.57E-02
	K-feldspar	1.21	0.96	1.40E-03
	Calcite	0.78	0.14	2.10E-04
	Kaolinite	2.26	24.40	NA
	Muscovite	0.60	0.61	NA
	Albite	24.50	20.00	2.91E-02

	Siderite	0.29	0.37	5.43E-04
	Anatase	0.81	0.14	2.02E-04
	Smectite/Illite	0.24	1.38	NA
Bandera Grey	Quartz	63.46	60.91	3.32E-02
	K-feldspar	12.12	5.59	3.05E-03
	Albite	10.22	6.59	3.59E-03
	Calcite	5.69	0.71	3.90E-04
	Illite	6.39	26.09	NA
	Muscovite	0.69	0.00	NA
	Biotite	1.14	0.00	0.00E+00
	Anatase	0.29	0.10	5.65E-05

4.3.2 Relationship evaluation of quantified mineral properties

In this section, relationships among mineral abundance, accessibility, accessible surface area and total connected surface area are explored. Mineral accessibilities that account for only connected pores and those that consider all pores are both considered and plotted in the following figures (Figure 4.8, 4.9, 4.10, 4.12). Samples were characterized into three categories to evaluate the potential impact of clay and carbonate content on quantification of mineral properties using the imaging approach (Table 4.2). Four minerals are selected here for analysis – quartz, K-feldspar, albite, and carbonate minerals, which includes calcite and/or dolomite. These phases are present in a majority of the samples considered. BET specific surface area from the literature are also included (Figure 4.9) to compare with accessible surface area determined from images.

Table 4.2 Categories of the ten samples based on relative abundances of clay and carbonate: 1) high clay, high carbonate content sample; 2) high clay, low carbonate content sample and 3) low clay, low carbonate content sample.

Sample category	Formations
High clay and high carbonate content	Bandera Grey
	Paluxy (Kemper)
	Baltic Sea sample (Ma et al., 2021)
High clay and low carbonate content	Bandera Brown
	Kentucky
	Lower Tuscaloosa (Landrot et al., 2012)
Low clay and low carbonate content	Lower Tuscaloosa (Geological Survey of Alabama)
	Leopard
	Bentheimer
	Paluxy (Geological Survey of Alabama)

4.3.2.1 Abundance versus accessibility

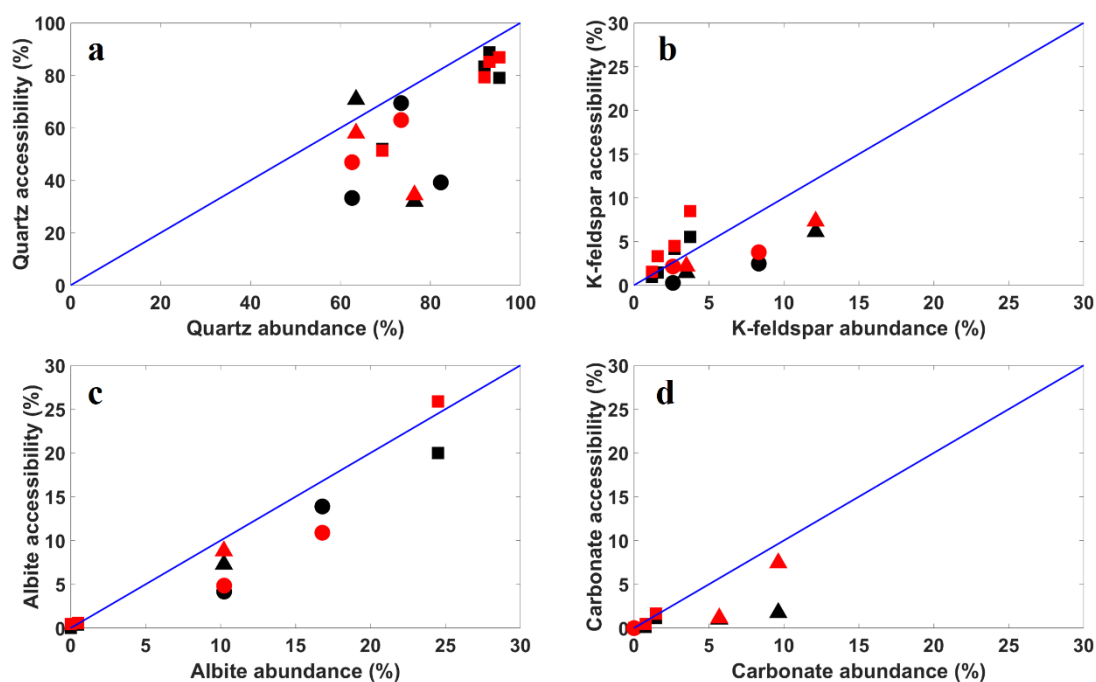


Figure 4. 8. Relationship between mineral abundance and mineral accessibility: a) quartz, b) K-feldspar, c) albite and d) carbonate minerals. Accessible surface area calculated by only accounting the connected pores is marked in black, accessible surface area that accounts for all pores are marked in red. Triangles are data points of samples with high clay and high carbonate content, spheres are samples with high clay and low carbonate content, and squares are samples with low clay and low carbonate content.

Mineral abundances are plotted against accessibilities in Figure 4.8. As the most abundant phase, quartz has the highest accessibility among these mineral species, however, most of the data points falls under the $y = x$ line, indicating relatively less accessibility per abundance than other phases. For the samples with lower clay and carbonate content, where the quartz content is more than 90% (Figure 4.8a), the accessibility per abundance for quartz is close to the $y = x$ line, indicating quartz accessibility is proportional to its abundance when the sample is predominantly composed of quartz. For other samples with less abundance of quartz (<80%), the accessibility per abundance of quartz are almost all below and some are farther away from the $y = x$ line. The impact of clay and carbonate content on accessibility can be considered by comparing samples with low to high clay and carbonate content shown as different symbols in Figure 4.8. The accessibility of quartz largely decreases in samples with higher clay and carbonate content (Figure 4.8a, triangle and sphere shapes), indicating clay and carbonate content has a large impact on the accessibility of quartz.

The accessibility of feldspar minerals – K-feldspar and albite generally increases

with abundance. Comparing with K-feldspar, albite is less impacted by the clay or carbonate content, while K-feldspar is more accessible when the sample has lower clay or lower carbonate content (Figure 4.8b, square shapes). As for carbonate minerals, the accessibility per abundance tends to decrease with increasing abundance (Figure 4.8d). The black and red data points are referring to accessibility accounting for only connected pores and accessibility assuming all pores connected, respectively. The variations in these estimated accessibilities are generally small (< 5%), however, the differences in the two estimated accessibilities of quartz can be large (up to 13%) in samples with relatively low quartz content (Figure 4.8a).

4.3.2.2 Abundance versus accessible surface area

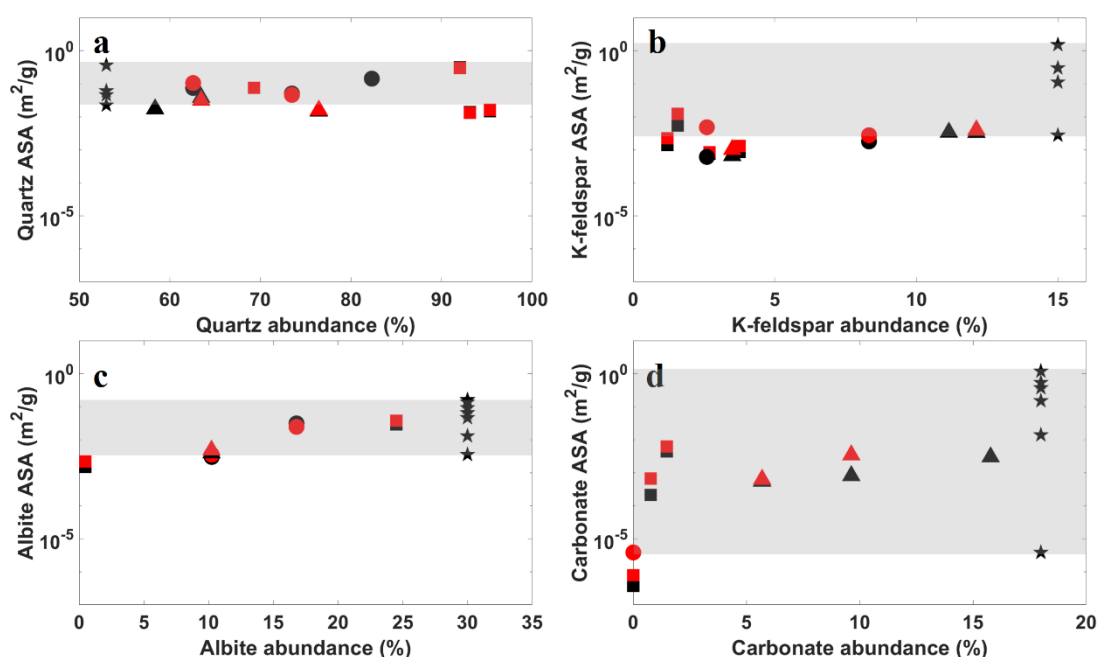


Figure 4. 9. Relationship between mineral abundance and mineral accessible surface area: a) quartz, b) K-feldspar, c) albite and d) carbonate mineral. Accessible surface area calculated by only accounting the connected pores is marked in black, accessible surface area that accounts for all pores are marked in red. Triangles are data points of samples with high clay and high carbonate content, spheres are samples with high clay and low carbonate content, and squares are samples with low clay and low carbonate content. BET specific surface areas reported in the literature are plotted with the star shape and their ranges are marked with grey shadows (abundances for these values are meaningless).

Mineral abundances against accessible surface areas are plotted in Figure 4.9. In general, quartz accessible surface area decreases with increasing abundance, except for the two Lower Tuscaloosa samples whose pores are well-connected compared to other samples. Accessibility of calcite initially increases with increasing abundance, then it becomes stable with no further distinct changes as its abundance increases.

No direct impact of mineral abundance on accessible mineral surface area are observed here for K-feldspar and (Figure 4.9b) which appear to have relatively consistent accessible surface area values while the accessible mineral surface area of albite increases with increasing abundance. In Figure 4.9c and d, it can be observed that samples with extremely low abundances (<1%) of albite and carbonate, the calculated accessible surface areas are much lower than those with higher abundances, the differences can be as large as 3 orders of magnitude (e.g. albite). The BET specific surface area from the literature (Figure 4.9, grey shadow areas) generally covers the range of the accessible surface areas determined from imaging. Overall, the BET specific surface areas are relatively higher than accessible surface area of albite, K-feldspar, carbonate (Figure 4.9b, c, d). Whereas the BET specific surface area of quartz collected from the literature have similar range to the accessible surface areas determined from 2D and 3D images.

4.3.2.3 Variation in accessibility with clay content

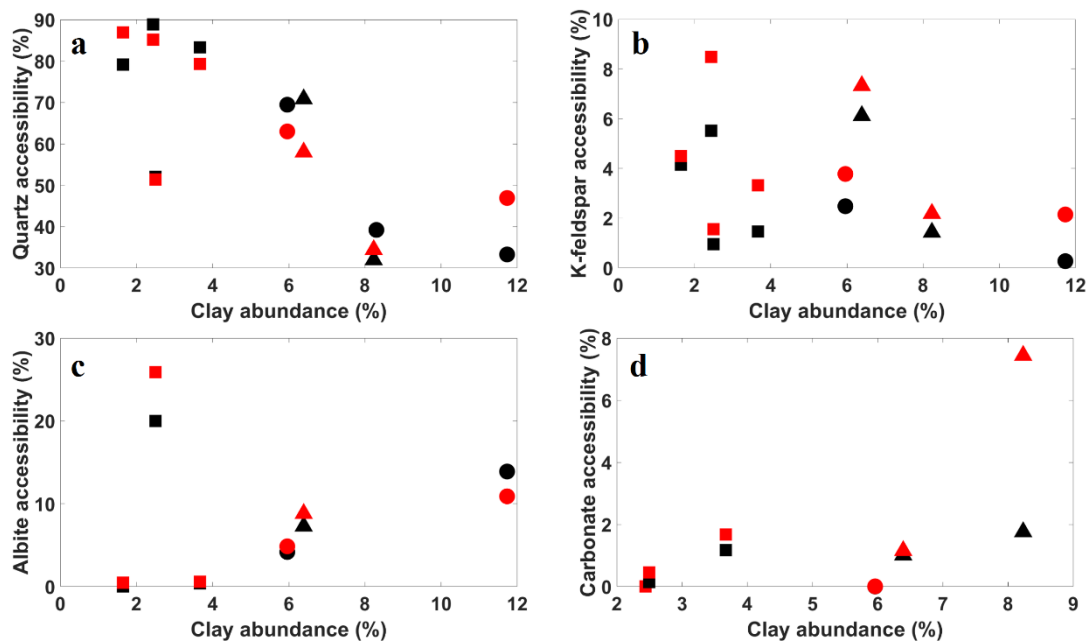


Figure 4. 10. Relationship between clay abundance and mineral accessibility: a) quartz, b) clay mineral, c) carbonate mineral. Triangles are data points of samples with high clay and high carbonate content, spheres are samples with high clay and low carbonate content, and squares are samples with low clay and low carbonate content.

Clay minerals are typically present as coating or bridging phases, which could potentially impact the overall pore connectivity and accessibility between mineral surfaces and pores. Mineral accessibility is plotted against clay abundance in Figure 4.10 to evaluate the potential impact of clay abundance on mineral accessibilities. Among the four mineral species, the accessibility of quartz is affected most by clay abundance, it decreases as the clay abundance increases. When the clay content is greater than 8%, the accessibility of quartz is less than 50%. However, for other three

minerals considered here, no distinct pattern or relationship are observed.

4.3.2.4 Dependence of connected surface area on composition

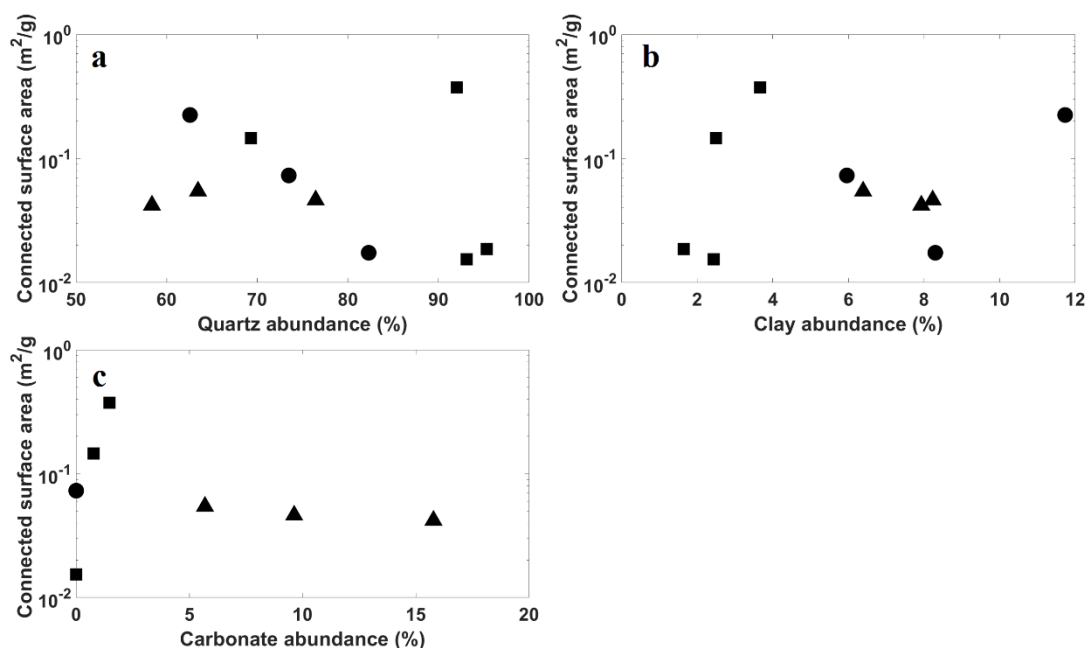


Figure 4. 11. Relationship between mineral abundance and the total connected surface area determined from 3D micro-CT images: a) quartz, b) clay mineral, c) carbonate mineral. Triangles are data points of samples with high clay and high carbonate content, spheres are samples with high clay and low carbonate content, and squares are samples with low clay and low carbonate content.

Variations in the total connected surface area with mineral composition are plotted in Figure 4.11. In general, the connected surface area decreases as quartz abundance increases, likely because of the relative smooth surface (decreased roughness) of quartz grains. Carbonate minerals are commonly present as a cementing phase, which could potentially decrease the overall pore connectivity. Here, the connected surface area slightly decreases as carbonate mineral abundance increases. However, the overall impact of carbonate content on the connected surface area is small. Increased surface area is expected with increasing clay content as clay coating increases the overall surface roughness. Here, smectite/illite and chlorite are assumed to be contributing to pore connectivity due to their well-connected micro-porosity (Landrot et al., 2012; Beckingham et al., 2017). However, certain clay mineral such as kaolinite may also decrease pore connectivity (Kassab et al., 2017). No apparent relationship between the connected surface area and clay content is observed here.

4.3.2.5 Dependence of connected surface area on mineral accessibility

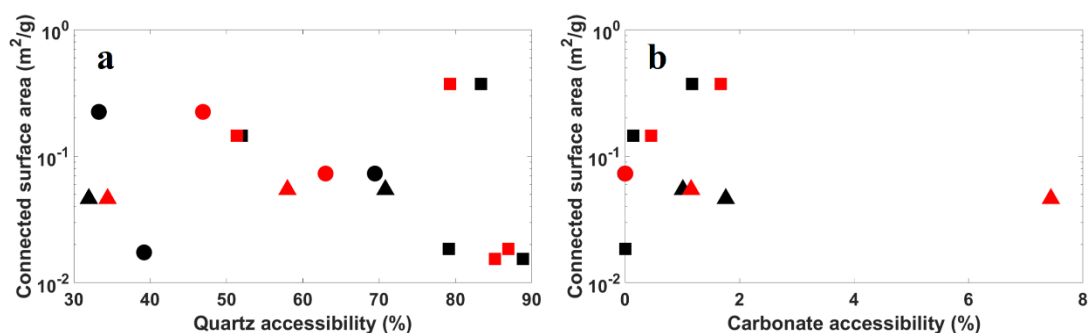


Figure 4. 12. Relationship between mineral accessibility and the total connected surface area calculated from 3D micro-CT images: a) quartz and b) carbonate mineral. Accessibility calculated by only accounting the connected pores is marked in black, accessibility that assumes all pores are connected is marked in red.

To explore how the accessibility of quartz and carbonate minerals impact the total connected surface area, the total connected surface area is plotted versus mineral accessibility in Figure 4.12. Quartz is the most abundant phase in all samples studied here. Compared with other mineral species, the surface of quartz is relatively smooth, and samples with higher quartz accessibility are expected to have lower surface area (Figure 4.12a). This is observed here with the exception of the two Lower Tuscaloosa samples. For carbonate minerals, samples with lower carbonate and clay content (Figure 4.12b, square shaped) tend to have higher surface areas. This is likely because carbonate minerals are usually present as cementing phases, which may decrease the overall pore connectivity and thus connected surface area.

4.4 Discussion

As is shown in Table 4.1, minerals with high accessibility do not necessarily have higher accessible surface area. Mineral accessible surface area also depends on the connected surface areas in three dimension. For example, the accessibility of K-feldspar in Leopard is 5.52%, whereas the accessibility of K-feldspar in Bandera Brown is only 2.48%. However, the accessible surface area of K-feldspar in Bandera Brown is 1.80E-03 m²/g, which is higher than 8.50E-04 m²/g of Leopard. This is due to the connected surface area of Bandera Brown is larger than Leopard. This is more evident for minerals with higher accessibilities. For instance, the accessible surface area of quartz decreases as the abundance increases. However, for the two Lower Tuscaloosa samples (plotted on the upright area of Figure 4.8a) whose connected surface areas are relatively higher than other samples, their accessible surface areas are higher and do not follow the trend.

Mineral accessibility is also impacted by clay and carbonate content. For example, as shown in Figure 4.9 a, b and c, quartz, K-feldspar and albite have relatively lower accessibility per abundance in samples with higher clay or higher carbonate content (triangle and sphere shapes). This is due to the fact that clay minerals are typically

present as coating phase on the surface of other minerals or in a form of bridging phase between mineral grains, and carbonate minerals are usually present as cementing phases among other mineral grains. Carbonate minerals can potentially reduce the pore connectivity, thus affecting the other minerals' accessibility to the pores, while the impact of clay minerals on the pore connectivity depends on clay type as well. In previous work, chlorite (Landrot et al., 2012) and smectite (Beckingham et al., 2017) was found to contain abundant, well-connected micro-porosity, which is permeable and would allow reacting fluid to pass through. Therefore, chlorite and smectite/illite are considered to contributing the overall pore connectivity here. However, Kassab et al. (2017) found that the presence of kaolinite is more likely to reduce the pore connectivity and permeability. Therefore, kaolinite is considered to reduce the overall accessibility in this work and considered as unconnected. In Table 1, it can also be observed that comparing with other mineral phases, clay minerals have higher accessibility per abundance, meaning they are more accessible with increasing abundance. For that reason, quartz is affected most by clay content since it typically has the highest abundance and accessibility, whereas for other mineral phases (Figure 4.10b, c and d), the impact of clay content is not obvious. Since different samples contains different clay types, clay content alone is insufficient to evaluate the relationship between clay and mineral accessibility and clay type also needs to be taken into account.

No apparent pattern between mineral accessible surface area and mineral abundances is observed here. However, the relationship among mineral accessibility, mineral abundance and clay content found here provides valuable insights on the mineral surface area estimation of an unknown sample. From Figure 4.8 and 4.10, we find that the accessibility of albite is almost proportional to its abundance, and it's not directly impacted by the clay content. As for quartz, the same pattern can be observed for samples with low clay content (Figure 4.8a). When clay content increases, the accessibility of quartz decreases (Figure 4.10a). More specifically, when clay content is greater than 8%, the accessibility of quartz is less than 50%. This could be utilized to estimate mineral accessibility if the sample composition is known (e.g. XRD analysis).

Conclusions

In this work, we aim to evaluate the potential relationships among the mineral properties determined from imaging. Here, seven samples were imaged using scanning electron microscopy and nano-computed tomography. The obtained images were processed to estimate porosity, mineral abundances, accessibilities and accessible surface areas. Three additional samples from the literature are also considered here for evaluation (Landrot et al., 2012; Qin and Beckingham, 2019; Ma et al., 2021). Four most common mineral phases found in sandstone were considered here, quartz, feldspar, clay and carbonate minerals. Relationships among the quantified properties of these minerals including mineral abundance, accessibility, accessible surface area, clay/carbonate content and connected surface area were evaluated.

Mineral accessible surface area is not directly related to mineral abundance, but largely depends on the connected surface area determined from 3D nano-CT images. Mineral accessibility can be used to estimate mineral accessible surface area. The process of estimating mineral accessibility from 2D BSE images is rather complicated, it is not only time-consuming, but also has high computational cost. In this work, we found that mineral accessibility of quartz and albite can be estimated with given mineral composition (e.g. determined through XRD analysis). The accessibility of albite increases proportionally with its abundance, thus, it can be estimated by measuring its abundance through a method like XRD analysis. The accessibility of quartz can be interpreted through its abundance and clay content. When samples contain no or low clay content, the accessibility of quartz is expected to be proportional to its abundance, while with increasing clay content, the accessibility decreases, (Figure 4.10a).

We found that the total connected surface area generally decreases with increasing quartz content. However, it does not necessarily solely depend on quartz content. The overall pore connectivity, clay type and clay content also effect the connected pore spaces. Therefore, measuring the connected surface area from 3D nano-CT images is needed and recommended for mineral accessible surface area estimation. In this process, nano-CT images are segmented into pores and grains, but mineral phase identification and registration are not needed. The total connected surface area can then be calculated through burning and marching cube algorithm in Matlab. Comparing with 2D image acquisition, segmentation and registration, quantifying the total connected surface area from 3D CT images is relatively less time, resource, and computational intensive.

No apparent pattern has been found for the estimation of the accessibility of carbonate minerals in this work and more data is needed to discern if a relationship exists.

Acknowledgement

This work is supported by the National Science Foundation under Grant No. EAR-1847243. Purchase of the X-ray Computed Nano-tomography instrument used to obtain results included in this publication was supported by the National Science Foundation under the award CMMI MRI 1919818.

References

1. Aagaard, P. and Helgeson, H.C., 1982. Thermodynamic and kinetic constraints on reaction rates among minerals and aqueous solutions; I, Theoretical considerations. *American journal of Science*, 282(3), pp.237-285.
2. Alfredsson, H.A., Oelkers, E.H., Hardarsson, B.S., Franzson, H., Gunnlaugsson, E. and Gislason, S.R., 2013. The geology and water chemistry of the Hellisheidi, SW-Iceland carbon storage site. *International Journal of Greenhouse Gas Control*, 12, pp.399-418.
3. Beckingham, L.E., Mitnick, E.H., Steefel, C.I., Zhang, S., Voltolini, M., Swift, A.M., Yang, L., Cole, D.R., Sheets, J.M., Ajo-Franklin, J.B. and DePaolo, D.J., 2016. Evaluation of mineral reactive surface area estimates for prediction of reactivity of a multi-mineral sediment. *Geochimica et Cosmochimica Acta*, 188, pp.310-329.
4. Beckingham, L.E., Steefel, C.I., Swift, A.M., Voltolini, M., Yang, L., Anovitz, L.M., Sheets, J.M., Cole, D.R., Kneafsey, T.J., Mitnick, E.H. and Zhang, S., 2017. Evaluation of accessible mineral surface areas for improved prediction of mineral reaction rates in porous media. *Geochimica et Cosmochimica Acta*, 205, pp.31-49.
5. Bensinger, J. and Beckingham, L.E., 2020. CO₂ storage in the Paluxy formation at the Kemper County CO₂ storage complex: Pore network properties and simulated reactive permeability evolution. *International Journal of Greenhouse Gas Control*, 93, p.102887.
6. Black, J.R., Carroll, S.A. and Haese, R.R., 2015. Rates of mineral dissolution under CO₂ storage conditions. *Chemical Geology*, 399, pp.134-144.
7. Boano, F., Harvey, J.W., Marion, A., Packman, A.I., Revelli, R., Ridolfi, L. and Wörman, A., 2014. Hyporheic flow and transport processes: Mechanisms, models, and biogeochemical implications. *Reviews of Geophysics*, 52(4), pp.603-679.
8. Bourg, I.C., Beckingham, L.E. and DePaolo, D.J., 2015. The nanoscale basis of CO₂ trapping for geologic storage. *Environmental science & technology*, 49(17), pp.10265-10284.
9. Brunauer, S., Emmett, P.H. and Teller, E., 1938. Adsorption of gases in multimolecular layers. *Journal of the American chemical society*, 60(2), pp.309-319.
10. Busch, B., 2020. Pilot study on provenance and depositional controls on clay mineral coatings in active fluvio-eolian systems, western USA. *Sedimentary Geology*, 406, p.105721.
11. Cao, Y., Song, H., Algeo, T.J., Chu, D., Du, Y., Tian, L., Wang, Y. and Tong, J., 2019. Intensified chemical weathering during the Permian-Triassic transition recorded in terrestrial and marine successions. *Palaeogeography, Palaeoclimatology, Palaeoecology*, 519, pp.166-177.
12. Chen, X.Y., Teng, F.Z., Huang, K.J. and Algeo, T.J., 2020. Intensified chemical weathering during Early Triassic revealed by magnesium isotopes. *Geochimica et*

- Cosmochimica Acta*, 287, pp.263-276.
13. Esene, C., Rezaei, N., Aborig, A. and Zendehboudi, S., 2019. Comprehensive review of carbonated water injection for enhanced oil recovery. *Fuel*, 237, pp.1086-1107.
 14. Fleming, M.R., Adams, B.M., Randolph, J.B., Ogland-Hand, J.D., Kuehn, T.H., Buscheck, T.A., Bielicki, J.M. and Saar, M.O., 2018, February. High efficiency and large-scale subsurface energy storage with CO₂. In *43rd Workshop on geothermal reservoir engineering, Stanford, CA*.
 15. Gbadamosi, A.O., Junin, R., Manan, M.A., Agi, A. and Yusuff, A.S., 2019. An overview of chemical enhanced oil recovery: recent advances and prospects. *International Nano Letters*, 9(3), pp.171-202.
 16. Griffiths, J., Worden, R.H., Wooldridge, L.J., Utley, J.E. and Duller, R.A., 2018. Detrital clay coats, clay minerals, and pyrite: a modern shallow-core analogue for ancient and deeply buried estuarine sandstones. *Journal of Sedimentary Research*, 88(10), pp.1205-1237.
 17. Ilojeji, C.O. and Beckingham, L.E., 2021. Assessment of geochemical limitations to utilizing CO₂ as a cushion gas in compressed energy storage systems. *Environmental engineering science*, 38(3), pp.115-126.
 18. Jia, H. and Sheng, J.J., 2018. Simulation study of huff-n-puff air injection for enhanced oil recovery in shale oil reservoirs. *Petroleum*, 4(1), pp.7-14.
 19. Kabuth, A., Dahmke, A., Beyer, C., Bilke, L., Dethlefsen, F., Dietrich, P., Duttmann, R., Ebert, M., Feeser, V., Görke, U.J. and Köber, R., 2017. Energy storage in the geological subsurface: dimensioning, risk analysis and spatial planning: the ANGUS+ project. *Environmental Earth Sciences*, 76(1), pp.1-17.
 20. Kassab, M.A., Hashish, M.F.A., Nabawy, B.S. and Elnaggar, O.M., 2017. Effect of kaolinite as a key factor controlling the petrophysical properties of the Nubia sandstone in central Eastern Desert, Egypt. *Journal of African Earth Sciences*, 125, pp.103-117.
 21. Koochi-Fayegh, S. and Rosen, M.A., 2020. A review of energy storage types, applications and recent developments. *Journal of Energy Storage*, 27, p.101047.
 22. Landrot, G., Ajo-Franklin, J.B., Yang, L., Cabrini, S. and Steefel, C.I., 2012. Measurement of accessible reactive surface area in a sandstone, with application to CO₂ mineralization. *Chemical Geology*, 318, pp.113-125.
 23. Lasaga, A.C., 1981. Transition state theory. *Rev. Mineral.; (United States)*, 8.
 24. Lasaga, A.C., 1984. Chemical kinetics of water-rock interactions. *Journal of geophysical research: solid earth*, 89(B6), pp.4009-4025.
 25. Li, L., Maher, K., Navarre-Sitchler, A., Druhan, J., Meile, C., Lawrence, C., Moore, J., Perdrial, J., Sullivan, P., Thompson, A. and Jin, L., 2017. Expanding the role of reactive transport models in critical zone processes. *Earth-science reviews*, 165, pp.280-301.
 26. Lu, J., Kharaka, Y.K., Thordsen, J.J., Horita, J., Karamalidis, A., Griffith, C., Hakala, J.A., Ambats, G., Cole, D.R., Phelps, T.J. and Manning, M.A., 2012. CO₂–

- rock–brine interactions in Lower Tuscaloosa Formation at Cranfield CO₂ sequestration site, Mississippi, USA. *Chemical Geology*, 291, pp.269-277.
27. Ma, J., Ahkami, M., Saar, M.O. and Kong, X.Z., 2021. Quantification of mineral accessible surface area and flow-dependent fluid-mineral reactivity at the pore scale. *Chemical Geology*, 563, p.120042.
 28. Mahdikhani, M., Bamshad, O. and Shirvani, M.F., 2018. Mechanical properties and durability of concrete specimens containing nano silica in sulfuric acid rain condition. *Construction and building materials*, 167, pp.929-935.
 29. Maher, K. and Navarre-Sitchler, A., 2019. Reactive transport processes that drive chemical weathering: From making space for water to dismantling continents. *Reviews in Mineralogy and Geochemistry*, 85(1), pp.349-380.
 30. March, R., Doster, F. and Geiger, S., 2018. Assessment of CO₂ storage potential in naturally fractured reservoirs with dual-porosity models. *Water Resources Research*, 54(3), pp.1650-1668.
 31. Nicot, J.P., Oldenburg, C.M., Houseworth, J.E. and Choi, J.W., 2013. Analysis of potential leakage pathways at the Cranfield, MS, USA, CO₂ sequestration site. *International Journal of Greenhouse Gas Control*, 18, pp.388-400.
 32. O’Connell, K. and Regalbuto, J.R., 2015. High sensitivity silicon slit detectors for 1 nm powder XRD size detection limit. *Catalysis Letters*, 145(3), pp.777-783.
 33. Pallud, C., Meile, C., Laverman, A.M., Abell, J. and Van Cappellen, P., 2007. The use of flow-through sediment reactors in biogeochemical kinetics: methodology and examples of applications. *Marine Chemistry*, 106(1-2), pp.256-271.
 34. Peters, C.A., 2009. Accessibilities of reactive minerals in consolidated sedimentary rock: An imaging study of three sandstones. *Chemical Geology*, 265(1-2), pp.198-208.
 35. Qin, F. and Beckingham, L.E., 2019. Impact of image resolution on quantification of mineral abundances and accessible surface areas. *Chemical Geology*, 523, pp.31-41.
 36. Qin, F. and Beckingham, L.E., 2021. The impact of mineral reactive surface area variation on simulated mineral reactions and reaction rates. *Applied Geochemistry*, 124, p.104852.
 37. Snæbjörnsdóttir, S.Ó., Oelkers, E.H., Mesfin, K., Aradóttir, E.S., Dideriksen, K., Gunnarsson, I., Gunnlaugsson, E., Matter, J.M., Stute, M. and Gislason, S.R., 2017. The chemistry and saturation states of subsurface fluids during the in situ mineralisation of CO₂ and H₂S at the CarbFix site in SW-Iceland. *International Journal of Greenhouse Gas Control*, 58, pp.87-102.
 38. Snæbjörnsdóttir, S.Ó., Gislason, S.R., Galeczka, I.M. and Oelkers, E.H., 2018. Reaction path modelling of in-situ mineralisation of CO₂ at the CarbFix site at Hellisheidi, SW-Iceland. *Geochimica et Cosmochimica Acta*, 220, pp.348-366.
 39. Steefel, C.I., DePaolo, D.J. and Lichtner, P.C., 2005. Reactive transport modeling: An essential tool and a new research approach for the Earth sciences. *Earth and Planetary Science Letters*, 240(3-4), pp.539-558.

40. Steefel, C.I., Molins, S. and Trebotich, D., 2013. Pore scale processes associated with subsurface CO₂ injection and sequestration. *Reviews in Mineralogy and Geochemistry*, 77(1), pp.259-303.
41. Steefel, C., 2018. *Reactive Transport Modeling: Applications in Subsurface Energy and Environmental Problems*. John Wiley & Sons.
42. Storvoll, V., Bjørlykke, K., Karlsen, D. and Saigal, G., 2002. Porosity preservation in reservoir sandstones due to grain-coating illite: a study of the Jurassic Garn Formation from the Kristin and Lavrans fields, offshore Mid-Norway. *Marine and Petroleum Geology*, 19(6), pp.767-781.
43. Tang, L., Gluyas, J. and Jones, S., 2018. Porosity preservation due to grain coating illite/smectite: evidence from Buchan Formation (Upper Devonian) of the Ardmore Field, UK North Sea. *Proceedings of the Geologists' Association*, 129(2), pp.202-214.
44. Waldmann, S., Busch, A., Van Ojik, K. and Gaupp, R., 2014. Importance of mineral surface areas in Rotliegend sandstones for modeling CO₂–water–rock interactions. *Chemical Geology*, 378, pp.89-109.
45. White, A.F. and Brantley, S.L., 2018. Chemical weathering rates of silicate minerals: an overview (pp. 1-22). De Gruyter.
46. Wooldridge, L.J., Worden, R.H., Griffiths, J. and Utley, J.E., 2019. How to quantify clay-coat grain coverage in modern and ancient sediments. *Journal of Sedimentary Research*, 89(2), pp.135-146.
47. Yu, Z., Wu, G., Keys, L., Li, F., Yan, N., Qu, D. and Liu, X., 2019. Seasonal variation of chemical weathering and its controlling factors in two alpine catchments, Nam Co basin, central Tibetan Plateau. *Journal of Hydrology*, 576, pp.381-395.

Chapter 5. Evaluation of mineral accessible surface area evolution induced by geochemical reactions

Fanqi Qin, Lauren, E. Beckingham*

Department of Civil and Environmental Engineering, Auburn University, AL, 36849

*leb@auburn.edu

Manuscript in preparation.

5.1 Introduction

Geochemical reactions such as CO₂-induced mineral dissolution and precipitation reactions can be impacted by temperature, pH, mineral reactive surface area, etc. As mineral reactions progress, formation properties including porosity and permeability can be altered as the pore structure and pore connectivity evolve (Algive et al., 2012; Beckingham et al., 2013; Nogues et al., 2013). This, in turn, could impact the ongoing reactions. Among all these constantly changing factors, mineral reactive surface area may also evolve as reaction proceeds (Carroll et al., 2013; Navarre-Sitchler et al., 2013; Luhmann et al., 2017; Příkryl et al., 2017; Yang et al., 2018). When pore connectivity increases (Navarre-Sitchler et al., 2013) or mineral grains disaggregate (Noiriel et al., 2009; Israeli and Emmanuel, 2018), the mineral reactive surface area could increase, whereas fine mineral grains with large surface area experiencing rapid dissolution (Noiriel et al., 2004; Noiriel et al., 2009) could decrease mineral reactive surface area.

The evolution of mineral reactive surface area during mineral reactions is not well understood. In CunchFlow (Steele et al., 2015), a software developed for multicomponent reactive flow and transport, the reactive surface area of the primary minerals is given by,

$$A_m = A_{m,0} \left\{ \begin{array}{ll} [(\frac{\phi}{\phi_0})(\frac{\phi_m}{\phi_{m,0}})]^{2/3} & \text{dissolution} \\ [\frac{\phi}{\phi_0}]^{2/3} & \text{precipitation} \end{array} \right\} \quad (1)$$

where A_m is mineral reactive surface area, $\phi_{m,0}$ is the initial volume fraction of the mineral m and ϕ_0 refers to the initial mineral porosity. The reactive surface areas of secondary minerals, those that precipitate as the simulation progresses, is calculated in similar form,

$$A_m = A_{m,0} \left\{ \begin{array}{ll} [(\frac{\phi}{\phi_0})\phi_m]^{2/3} & \text{dissolution} \\ [\frac{\phi}{\phi_0}]^{2/3} & \text{precipitation} \end{array} \right\} \quad (2)$$

The surface area is updated at each time step based on the change in mineral volume fraction and porosity. Similar relationships have been used in other studies (Lichtner, 1988; Emmanuel and Berkowitz, 2005; Carroll et al., 2013) where changing surface

area is associated with changing mineral abundance and porosity. These relationships are based on the assumption that mineral grains are spherical and smooth, and mineral surface area decreases with decreasing grain volume. This may reflect the surface area change in some cases (e.g. disaggregated samples), however, it does not necessarily reflect the surface area of consolidated samples or mineral surface roughness. Additionally, calculating mineral surface area assuming grains being spherical implies the entire surface is involved in the reactions, while in reality, it is highly likely that only a fraction of the surface is actively involved in the reactions.

Experimental studies have examined the evolution of mineral surface area during reactions. For instance, Mouzakis et al. (2016) studied the evolution of shale caprock porosity with respect to CO₂-brine-mineral reactions and found out that the total surface area and connected surface area increases when there is obvious increase in mineral porosity and connected porosity. Noiriel et al. (2009) observed that the reactive surface area of limestone (micrite and sparite) increased during an acidic water flow-through experiment, and the change of reactive surface area was impacted by the mineral spatial distribution and pore connectivity. However, it is challenging to determine mineral reactive surface areas since only a fraction of the surface might be actively involved (reactive) during the reactions. To account for surface accessibility, accessible surface areas will be measured through imaging and used as reactive surface area to inform reactive transport simulations. This work aims to estimate the accessible surface area of each mineral phase before and after dissolution experiments. By comparing the change of mineral volume fraction, accessible surface area, and by simulating what is observed in the experiments, the relationship between mineral accessible surface area, mineral volume fraction, and porosity can be developed for different mineral species. Moreover, the evolution of mineral accessible surface areas during geochemical reactions can be estimated.

5.2 Materials and methods

5.2.1 Sample characterization and preparation

Two sandstone samples from the Kentucky and Bandera Grey formations were selected for core-flood experiments and image analysis. Samples were provided by Kocurek Industries. Both of the core samples are 0.5 inch in diameter and 1 inch in length. The expected porosity is 20% for the Bandera Grey sample and 14% for the Kentucky samples (XRD data provided by Kocurek Industries). Both samples are predominantly composed of quartz, with other mineral species including feldspar, carbonate and clay minerals accounting for 12 to 15% of the composition, respectively (Kocurek Industries). Detailed mineralogy is given in Tables 5.1 and 5.2.

Core samples were cut into thick sections of 0.5-inch diameter and 0.5 cm thickness for 2D SEM imaging. One side of each sample was polished and impregnated with clear epoxy. The preparation was performed by Applied Petrographic Services. Inc

(Westmoreland, Pennsylvania). Thick section sample cutting for 2D imaging is by nature a destructive process. Therefore, comparing changes occurring at the exact location from the captured 2D SEM BSE images before and after the experiments is not feasible. However, nano-CT images of the core samples were captured for the same area of interest, from which the differences of the total connected surface areas before and after experiments can be evaluated.

Table 5.1 Mineral composition of Kentucky sandstone sample from XRD data provided by Kocurek Industries.

Mineral	Quartz	Albite	Microcline	Illite
Weight percentage (%)	66	17	3	14

Table 5.2 Mineral composition of Bandera Grey sandstone sample from XRD data provided by Kocurek Industries.

Mineral	Quartz	Albite	Dolomite	Kaolinite	Illite	Chlorite
Weight percentage (%)	59	12	15	3	10	1

5.2.2 Mineral properties quantification

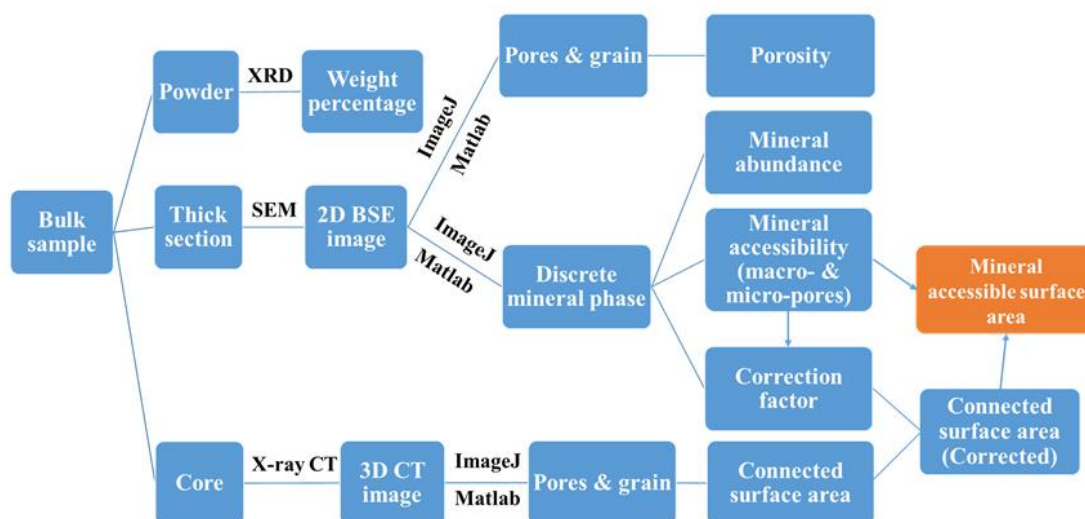


Figure 5. 1. Work flow of mineral properties (porosity, abundance, accessibility, accessible surface area) quantification.

Mineral properties including porosity, mineral abundance, accessibility and accessible surface areas were quantified before and after the core-flood experiments. As shown in Figure 5.1, to obtain 2D SEM BSE images, the sample thick section was imaged using ZEISS EVO 50VP scanning electron microscope provided by the Auburn University Research Instrumentation Facility (AURIF) at Auburn University. Images

were captured under backscatter detector, with a beam intensity of 20 kV and working distance of 8.5 mm. Upon acquisition of the 2D SEM BSE images of sample thick sections, the pores and grains were first segmented by applying the thresholding approach proposed in Peters, 2009. The porosity was calculated as the total number of pore pixels divided by total number of pixels in the image. Following the initial segmentation, each mineral phase was identified through SEM EDS elemental maps where the distributions of different elements were shown. The discrete mineral phases were then registered and assigned different colors to form the final mineral-phase segmented image. Mineral abundance refers to the fraction of the discrete mineral phase in relation to the total mineral volume fraction (pores not included). Mineral abundances were calculated by counting the number of pixels of each mineral phase and dividing by the total number of mineral pixels. Mineral accessibility is defined as the mineral surface which is in direct contact with the pore space, and was calculated by counting the number of mineral pixels for each specific mineral phases that are adjacent to pore pixels. Next, the accessible mineral surface area was calculated for each mineral phase following the 2D and 3D imaging approach proposed in Landrot et al., 2012.

3D X-ray nano-CT images were captured using a ZEISS Xradia 620 Versa X-ray nano-computed tomography microscope at Auburn University. Beam intensity was set to be 100 keV with 8 seconds exposure time and a total of 3601 projections were taken for each sample at a voxel resolution of 2 microns. The reconstruction of the images was performed by the automated reconstruction software provided by ZEISS. The reconstructed 3D nano-CT images were cropped into small cubes with the same total area as the 2D SEM BSE images. The connected pore regions within this cropped cube were identified using a marching cube and burning algorithms, from which the total connected surface area was calculated based on a mesh defined on the associated mineral surfaces. The accessible mineral surface area was then calculated by multiplying the accessibility of each mineral phase by the connected surface area. Lastly, a correction factor (CF) is also calculated to account for the estimation error of connected surface area resulting from resolution differences in the 2D SEM BSE image and 3D nano-CT images. The resolution of the SEM BSE image was reduced to match with the resolution of nano-CT images, and then the number of connected interfacial pixels in the two images was determined. The correction factor was calculated as the number of connected interfacial pixels in the original images divided by the number of connected interfacial pixels in the resolution-reduced images. This was then multiplied with the connected surface area to get the corrected connected surface area.

5.2.3 Core-flood dissolution experiments

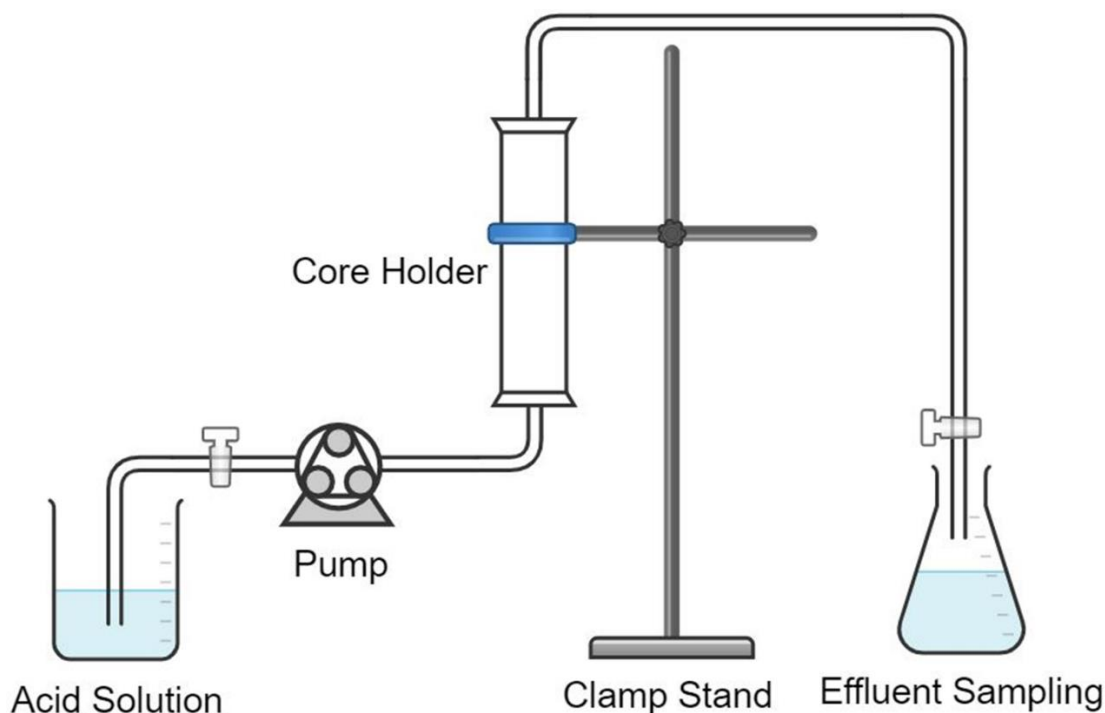


Figure 5. 2. Experimental setup diagram of a single-phase core-flood through dissolution experiment.

The core-flood experiments were conducted under room temperature 20 °C with 0.01 M hydrochloric acid (pH = 2) used as the reacting fluid. A CHEM_TECH peristaltic chemical metering pump was used to provide constant flow rate of 1 ml/min. The core samples were wrapped in a heat shrinkable tube which was then placed in a 3D – printed core holder. The printing material is resin, which hardens under room temperature. The core sample was epoxied to the inner wall of the core holder to prevent acid flow. The core was first flushed with deionized water at a flow rate of 1 ml/min for 24 hours to saturate the sample, followed by 0.01 M hydrochloric acid. The experiments durations were 1 week (168 hours) for the Kentucky sample and 2 weeks (336 hours) for the Bandera Grey sample. At the end of the experiments, deionized water was used again to flush out the acid residue. Effluent samples were periodically collected and evaluated with inductively coupled plasma - optical emission spectrometry (ICP-OES) for the concentration of the following ions: potassium (K^+), sodium (Na^+), magnesium (Mg^{2+}), calcium (Ca^{2+}), iron (Fe^{2+}/Fe^{3+}) and aluminum (Al^{3+}). The ICP-OES analysis was carried out on a Varian 710ES ICP-OES at Auburn University.

5.2 Results

5.3.1 Image segmentation and mineral property quantification

5.3.1.1 Unreacted samples

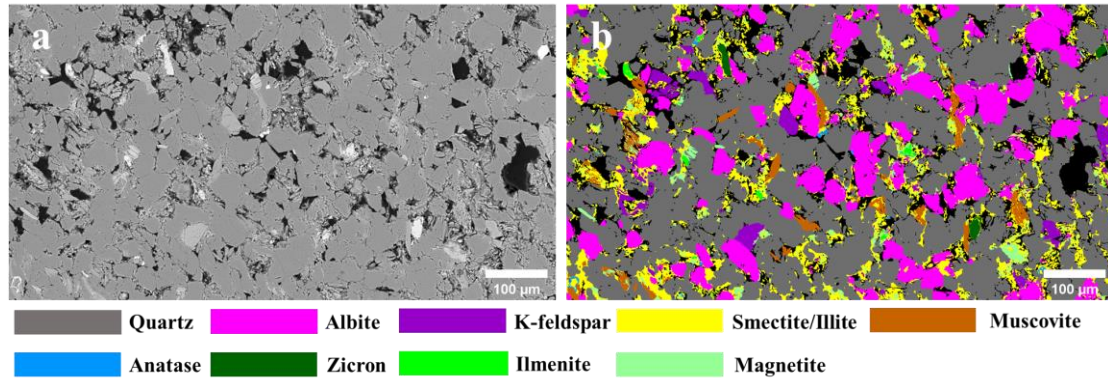


Figure 5. 3. a) 2D SEM BSE image of the unreacted Kentucky sample thick section captured under resolution of 0.44 μm; b) discrete mineral phase map with nine mineral phase identified and segmented, each color corresponds to one mineral specie. (Reproduced from Chapter 4, Figure 4.5).

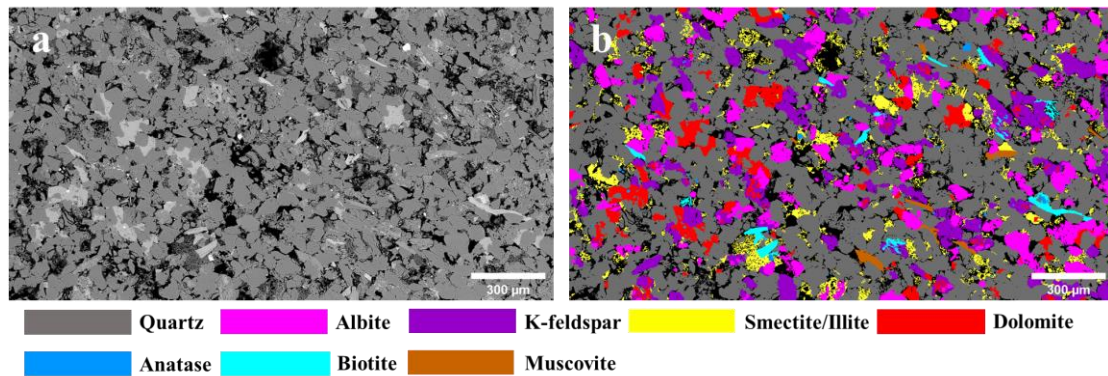


Figure 5. 4. a) 2D SEM BSE image of the unreacted Bandera Grey sample thick section captured under resolution of 0.74 μm; b) mineral phase segmented map with eight minerals identified in the area of interest, each mineral specie expressed in unique color. (Reproduced from Chapter 4, Figure 4.7).

Table 5.3 Mineral properties of the unreacted samples determined from 2D SEM BSE images and 3D nano-CT images (data from Chapter 4, Table 4.1). The accessible surface area of smectite/illite, muscovite and biotite cannot be directly measured through the images captured.

Formation	Mineral	Abundance (%)	Accessibility (%)	Accessible surface area (m ² /g)
Kentucky	Quartz	62.58	33.27	7.46E-02
	Albite	16.79	13.89	3.11E-02
	K-feldspar	2.92	0.27	6.10E-04
	Smectite/Illite	11.73	49.95	NA
	Ilmenite	0.29	0.50	1.13E-03
	Magnetite	2.60	1.70	3.82E-03
	Anatase	0.17	0.05	1.17E-04
	Zircon	0.37	0.00	0.00E+00
	Muscovite	2.55	0.36	NA
Bandera Grey	Quartz	63.46	60.91	3.32E-02
	K-feldspar	12.12	5.59	3.05E-03
	Albite	10.22	6.59	3.59E-03
	Calcite	5.69	0.71	3.90E-04
	Smectite/Illite	6.39	26.09	NA
	Muscovite	0.69	0.00	NA
	Biotite	1.14	0.00	NA
	Anatase	0.29	0.10	5.65E-05

2D BSE images of the unreacted samples and their corresponding mineral-segmented maps are shown in Figure 5.3 and 5.4 (data from Chapter 4, Table 4.1). Nine mineral species were identified in BSE image of Kentucky sample, where quartz has the highest abundance (62.58%), followed by albite with an abundance of 16.79%. The clay content of Kentucky is also high, the clay minerals are determined to be a mix of

smectite and illite, with an abundance of 11.73%. The abundances of other mineral phases are all below 3%. Even though quartz is most dominant phase, the accessibility of quartz is only 33.27% whereas the accessibility of smectite/illite is 49.95%. This is due to the fact that clay minerals commonly exist as coating or bridging phases on/between the surfaces of other mineral grains, which limits the accessibility of other mineral species. The accessibilities of other mineral phases are all below 2%. The calculated accessible surface areas vary up to 2 orders of magnitude (Table 5.3). The accessible surface area of quartz and albite are $7.46\text{E-}02$ and $3.11\text{E-}02$ m^2/g , respectively. For other mineral species, the calculated accessible surface areas fall within the range of $1.17\text{E-}04$ to $3.82\text{E-}03$ m^2/g .

As for Bandera Grey, eight mineral phases were identified and segmented (Figure 5.4) in the area of interest. Quartz is the predominated phase with 63.46% abundance, the abundances of K-feldspar and albite are calculated to be 12.12% and 10.22%. Carbonate mineral – calcite is also found to be present with an abundance of 5.69%. The clay minerals found in the area of interest is mainly composed of smectite and illite mixture. The abundances of other minerals are all below 2%. Quartz here also has the highest accessibility (60.91%), followed by smectite/illite (26.09%). Although the abundances of calcite and smectite/illite are close, the accessibility of calcite (0.71%) is significantly lower than smectite/illite. The accessibility of the two feldspar minerals – K-feldspar and albite are calculated to be 5.59% and 6.59%, respectively. The estimated accessible surface areas of these mineral species vary up to 3 orders of magnitude (Table 3). Quartz has the highest accessible surface area ($3.32\text{E-}02$ m^2/g), followed by two feldspar minerals – K-feldspar ($3.05\text{E-}03$ m^2/g) and albite ($3.59\text{E-}03$ m^2/g). The accessible surface area of calcite is calculated to be $3.90\text{E-}04$ m^2/g , and $5.65\text{E-}05$ m^2/g for anatase.

The resolution of the images captured here is inadequate to measure the surface area of clay minerals and minerals like muscovite/biotite (many small-scale features on the surface), therefore, the accessible surface areas of these mineral species are not discussed here.

5.3.1.2 Reacted samples

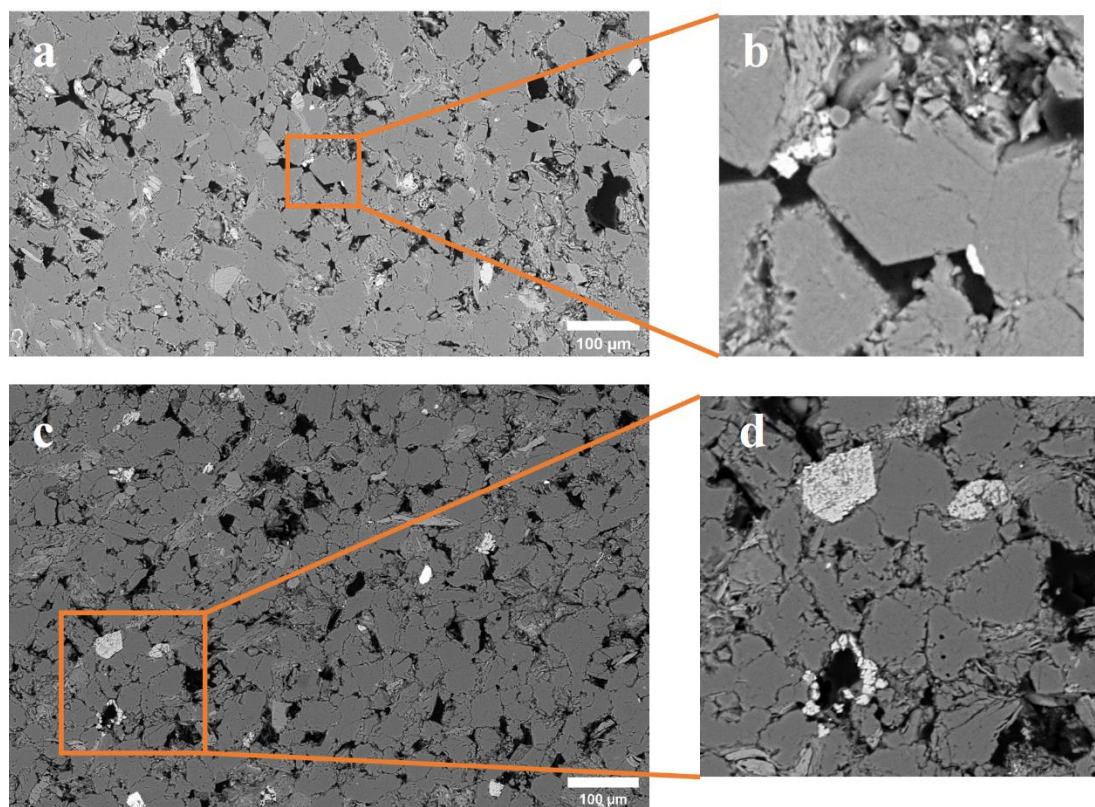


Figure 5. 5. 2D BSE images of Kentucky sample thick section before and after the core-flood dissolution experiment: a) BSE image of the unreacted sample, captured under resolution of 0. 44 μm; b) close-up of unreacted anatase (TiO_2) grains (white grains); c) BSE image of the reacted sample, captured under resolution of 0. 29 μm; d) close-up of the reacted anatase grains.

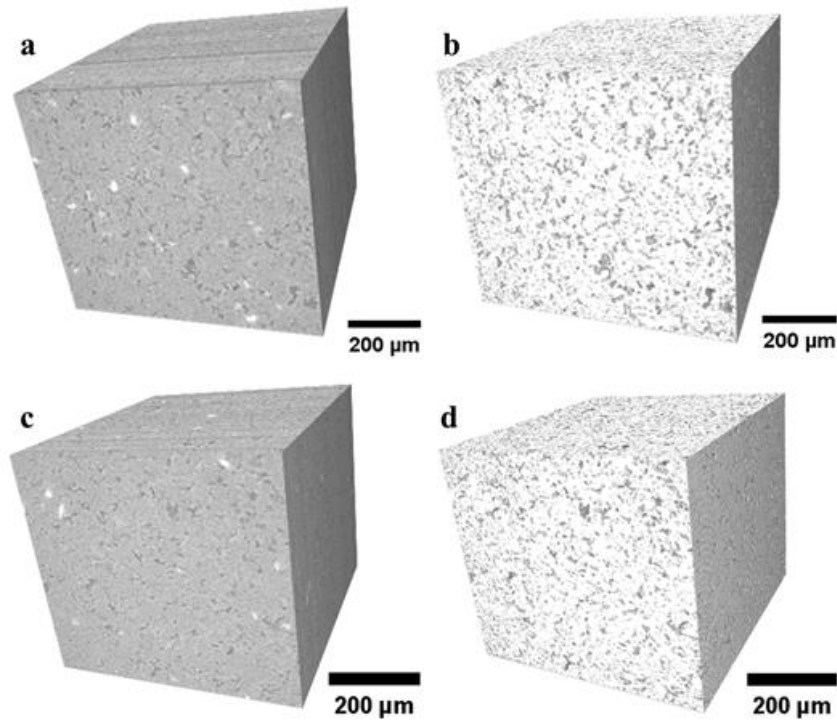


Figure 5. 6. 3D nano-CT images of Kentucky core sample before and after the core-flood experiment: a) reconstructed 3D nano-CT image of the unreacted core sample with a voxel resolution of 2 μm ; b) segmented nano-CT image of the unreacted core sample; c) reconstructed 3D nano-CT image of the reacted core sample with a voxel resolution of 2 μm ; d) segmented nano-CT image of the reacted core sample.

Table 5.4 Porosity and connected surface area calculated from 2D SEM BSE images and 3D nano-CT images, comparing the changes before and after experiment.

Sample	Porosity determined from BSE image (%)	Porosity determined from CT image (%)	Connected surface area (m^2/g)
Kentucky (unreacted)	13.25	10.73	0.02
Kentucky (reacted)	11.49	13.23	0.07
Bandera Grey (unreacted)	15.31	18	
Bandera Grey (reacted)			

The 2D SEM BSE image of the reacted Kentucky sample is given in Figure 5.5 for comparison with the unreacted sample. In general, the sample after core-flood dissolution experiments appears to have increased surface roughness. In the close-up images shown in Fig 5b and d, dissolution of anatase (TiO_2) is observed, which could potentially increase the porosity as well as pore connectivity. Prior to the core-flood dissolution experiment, the anatase grains appear to have smooth surfaces and intact structures. In image of the reacted sample (Figure 5.5c), additional roughness is evident on the surface of anatase grains. In addition, a large portion of one of the anatase appears to be dissolved, which creates additional pore space.

The increase in mineral surface roughness can also be interpreted from the quantitative results (Table 5.4) calculated from 3D nano-CT images (Figure 5.6). There is a slight increase in the porosity calculated from nano-CT images for the Kentucky sandstone sample, where the images were captured in the same area of the core. The porosity increased from 10.73% to 13.23% after the core-flood experiment with a duration of 1 week (168 hours). The connected surface area calculated from 3D nano-CT images increases from 0.02 to 0.07 m^2/g . This suggests the pore connectivity or the mineral surface roughness increased during the dissolution experiment.

Future work:

The core of the Bandera Grey sample was sent to Applied Petrographic services. Inc for thick section cutting, polishing and epoxy impregnation. Similar to Kentucky (Figure 5.5 and 5.6), the thick section of Bandera Grey will be imaged using scanning electron microscope under backscatter electron detector to obtain 2D BSE images. The image will be processed through ImageJ and MATLAB to segment and register each mineral phases. Mineral properties including porosity, abundance, accessibility, accessible surface area, connected surface area will be quantified and compared to the unreacted sample to evaluate any changes resulted from core-flood dissolution experiment.

5.3.1 Effluent sample analysis

5.3.1.1 Kentucky

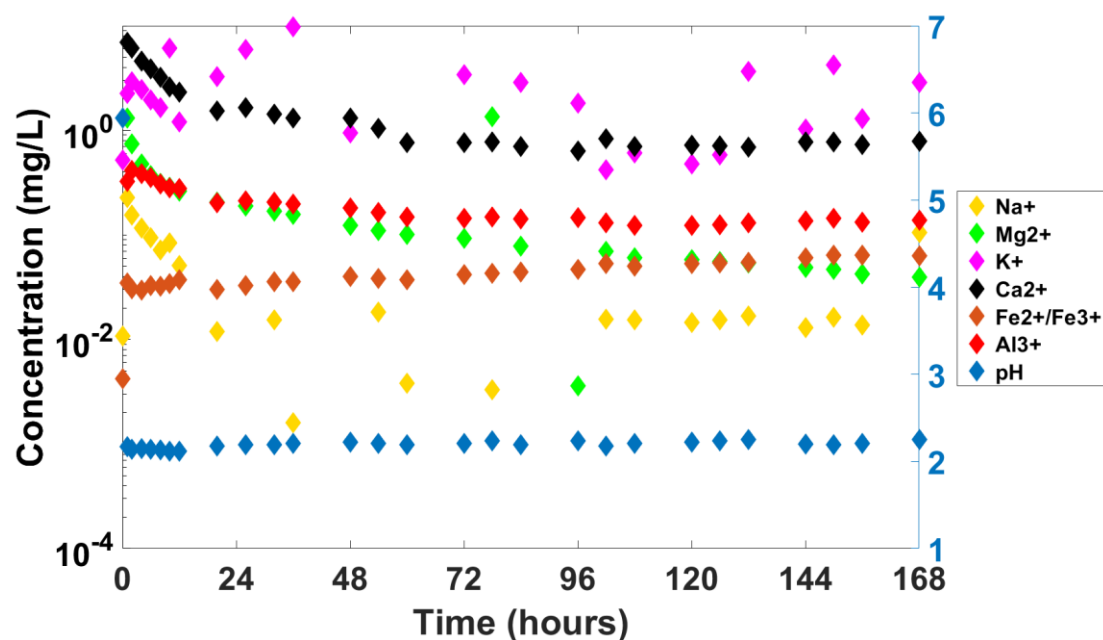


Figure 5. 7. The evolution of the major ion concentrations in the effluent sample collected from core-flood experiment with Kentucky sample, data measured through ICP-OES.

The concentration of major ions in effluent sample collected during the 168-hour core-flood experiment are plotted in Figure 5.7. The initial peak of the calcium (Ca^{2+}) and magnesium (Mg^{2+}) concentration (Figure 5.7, black and green data points) indicates that there is likely small amount of dolomite – $\text{CaMg}(\text{CO}_3)_2$ dissolution. Potassium (K^+) and sodium (Na^+) are expected to result from the dissolution of clay minerals – smectite/illite. The dissolution of feldspar minerals – K-feldspar and albite can also contribute to the release of potassium and sodium ions, however, comparing with clay smectite/illite, feldspars are chemically more stable, and therefore are expected to have lower reaction rates than smectite/illite. Aluminum (Al^{3+}) ions are expected to mainly come from the dissolution of clay minerals (smectite/illite), but dissolution of feldspars and muscovite can also result in increase of aluminum concentration. pH is also measured during the 168-hour period, where it remains stable around 2.2 throughout the experiment.

Future work:

The effluent sample of the Bandera Grey collected from the core-flood experiment will be analyzed using a Varian 710ES ICP-OES at Auburn University. The concentration of the major ions will be measured and plotted to evaluate the evolution of these ions during the experiment.

5.4 Discussion

Opposite phenomena are observed between the results of porosity calculated from 2D SEM BSE images and 3D nano-CT images. This is due to the fact that 2D SEM BSE imaging is a destructive process, where analyzing the exact sample location/area is not feasible. In addition, the homogeneity of the pore distribution also varies among samples. Therefore, small variations in estimated porosity from 2D SEM BSE images are expected. However, the 3D nano-CT images were captured in the same area of the core, thus, the porosity estimated from 3D nano-CT images here are more representative than porosity estimated from 2D SEM BSE images.

Initial analysis suggests that mineral surface roughness and pore connectivity could have increased during the 168-hour core-flood dissolution experiment with 0.01M hydrochloric acid (pH = 2). The overall dissolution reaction rates and extent are expected to be low as no distinct differences were observed before and after experiment from both BSE and CT images. However, pore connectivity could be increased if dissolution reactions occurs at pore throats, which could create more flow path to allow more interactions between the reacting fluid interacting and mineral phases.

Sample effluent analysis with ICP-OES data suggest that carbonate minerals are present in the sample, however, it has not been found in the captured SEM BSE images, most likely due to the its low volume fraction. This corresponds to the XRD analysis of the sample where no carbonate minerals were found, it is plausible that the amount of carbonate present in the sample is under the detection limit of X-ray diffraction instrument.

Acknowledgement

This work is supported by the National Science Foundation under Grant No. EAR-1847243. Purchase of the X-ray Computed Nano-tomography instrument used to obtain results included in this publication was supported by the National Science Foundation under the award CMMI MRI 1919818.

References

1. Algive, L., Békri, S., Nader, F.H., Lerat, O. and Vizika, O., 2012. Impact of diagenetic alterations on the petrophysical and multiphase flow properties of carbonate rocks using a reactive pore network modeling approach. *Oil & Gas Science and Technology–Revue d'IFP Energies nouvelles*, 67(1), pp.147-160.
2. Beckingham, L.E., Peters, C.A., Um, W., Jones, K.W. and Lindquist, W.B., 2013. 2D and 3D imaging resolution trade-offs in quantifying pore throats for prediction of permeability. *Advances in water resources*, 62, pp.1-12.
3. Carroll, S., Hao, Y., Smith, M. and Sholokhova, Y., 2013. Development of scaling parameters to describe CO₂–rock interactions within Weyburn-Midale carbonate flow units. *International Journal of Greenhouse Gas Control*, 16, pp. S185-S193.
4. Emmanuel, S. and Berkowitz, B., 2005. Mixing-induced precipitation and porosity evolution in porous media. *Advances in water resources*, 28(4), pp.337-344.
5. Israeli, Y. and Emmanuel, S., 2018. Impact of grain size and rock composition on simulated rock weathering. *Earth Surface Dynamics*, 6(2), pp.319-327.
6. Lichtner, P.C., 1988. The quasi-stationary state approximation to coupled mass transport and fluid-rock interaction in a porous medium. *Geochimica et Cosmochimica Acta*, 52(1), pp.143-165.
7. Luhmann, A.J., Tutolo, B.M., Bagley, B.C., Mildner, D.F., Seyfried Jr, W.E. and Saar, M.O., 2017. Permeability, porosity, and mineral surface area changes in basalt cores induced by reactive transport of CO₂-rich brine. *Water Resources Research*, 53(3), pp.1908-1927.
8. Mouzakis, K.M., Navarre-Sitchler, A.K., Rother, G., Bañuelos, J.L., Wang, X., Kaszuba, J.P., Heath, J.E., Miller, Q.R., Alvarado, V. and McCray, J.E., 2016. Experimental study of porosity changes in shale caprocks exposed to CO₂-saturated brines I: Evolution of mineralogy, pore connectivity, pore size distribution, and surface area. *Environmental Engineering Science*, 33(10), pp.725-735.
9. Navarre-Sitchler, A.K., Cole, D.R., Rother, G., Jin, L., Buss, H.L. and Brantley, S.L., 2013. Porosity and surface area evolution during weathering of two igneous rocks. *Geochimica et Cosmochimica Acta*, 109, pp.400-413.
10. Nogues, J.P., Fitts, J.P., Celia, M.A. and Peters, C.A., 2013. Permeability evolution due to dissolution and precipitation of carbonates using reactive transport modeling in pore networks. *Water Resources Research*, 49(9), pp.6006-6021.
11. Noiriél, C., Gouze, P. and Bernard, D., 2004. Investigation of porosity and permeability effects from microstructure changes during limestone dissolution. *Geophysical research letters*, 31(24).
12. Noiriél, C., Luquot, L., Madé, B., Raimbault, L., Gouze, P. and Van Der Lee, J., 2009. Changes in reactive surface area during limestone dissolution: An experimental and modelling study. *Chemical Geology*, 265(1-2), pp.160-170.
13. Perrin, J.C. and Benson, S., 2010. An experimental study on the influence of sub-core scale heterogeneities on CO₂ distribution in reservoir rocks. *Transport in porous media*, 82(1), pp.93-109.

14. Příklad, J., Jha, D., Stefánsson, A. and Stipp, S., 2017. Mineral dissolution in porous media: An experimental and modeling study on kinetics, porosity and surface area evolution. *Applied geochemistry*, 87, pp.57-70.
15. Qin, F. and Beckingham, L.E., 2019. Impact of image resolution on quantification of mineral abundances and accessible surface areas. *Chemical Geology*.
16. Steefel, C.I., Appelo, C.A.J., Arora, B., Jacques, D., Kalbacher, T., Kolditz, O., Lagneau, V., Lichtner, P.C., Mayer, K.U., Meeussen, J.C.L. and Molins, S., 2015. Reactive transport codes for subsurface environmental simulation. *Computational Geosciences*, 19(3), pp.445-478.
17. Yang, Y., Bruns, S., Stipp, S.L.S. and Sørensen, H.O., 2018. Impact of microstructure evolution on the difference between geometric and reactive surface areas in natural chalk. *Advances in Water Resources*, 115, pp.151-159.

Chapter 6. Conclusions and contribution to new knowledge

6.1 Enhanced understanding of the impact of image resolution on quantified mineral properties

In the work presented in Chapter 2, a sandstone sample extracted from Paluxy formation located at Kemper pilot CO₂ injection site, Mississippi, U.S. was imaged using scanning electron microscopy under backscatter electron mode. The purpose of this work was to understand how image resolution affects the quantified mineral properties including porosity, mineral abundance, mineral accessibility and accessible surface area. Five BSE images of the same area of interest were captured under resolutions varying from 0.34 μm to 5.71 μm . Image segmentation and registration was performed with consistent methods and procedures to minimize the discrepancies induced by image processing rather than image resolution.

Mineral properties including porosities, abundances and accessibilities were quantified from the segmented 2D BSE images, while the mineral accessible surface areas were calculated by combining the accessibility from 2D BSE image and the connected surface area from 3D CT images. By comparing the obtained results, we found that mineral abundances and porosity agree relatively well with changing resolution, indicating the impact of image resolution is small on mineral abundance and porosity quantification. However, mineral accessibility varies with changing resolution. Minerals like smectite and muscovite that have many small-scale features (e.g. surface roughness, sheet-structure) tend to have decreased accessibility with decreasing resolution. These small-scale features are not captured under lower image resolutions. Variations in the estimated mineral accessible surface areas are less than 1 order of magnitude.

The analysis in this work provides insights on how the quantified mineral properties are impacted by image resolution, and also provides guidance on what image resolution to choose when performing image analysis on geological samples. For example, when a sample contains a high abundance of minerals with small-scale features, image resolutions $< 1 \mu\text{m}$ are recommended. Samples without these minerals can be imaged at lower resolutions and are expected to yield similar results. Image resolution matters since higher resolutions require much more time and computational power to process, and therefore, the analysis of this work is informative to researchers whose goal is to quantifying mineral properties from imaging.

6.2 Improved understanding of the impact of surface area variation on simulated reactions

Reactive mineral surface area is one of the controlling parameters for geochemical reactions, Reactive surface areas can be estimated through various ways, such as the

BET adsorption method, a geometry approximation and imaging techniques. In the first work presented, less than one order of magnitude variations in mineral accessible surface areas were observed, however, the impact of the observed variation in surface area on simulated mineral reaction and reaction rates is unknown. Additionally, reactive surface area estimated through different approaches can vary up to 7 orders of magnitude (Black et al., 2015; Bourg et al., 2015), the impact of such significant surface area variations on simulated reactions needs to be better understood.

In the second work presented in Chapter 3, a reactive transport model was built in CrunchFlow to simulate geochemical reactions induced by CO₂. Simulations were carried out using mineral accessible surface areas calculated from imaging, BET specific surface areas reported in the literature and geometric surface areas. Very small differences occur in the simulations that use mineral accessible surface areas, indicating the variations in surface area resulted from image resolution has a small impact on the simulated reactions. However, when BET specific surface areas and geometric surface areas were used in the simulations, large discrepancies were observed at longer times for non-carbonate minerals, indicating the simulated mineral reactions for these more stable mineral phases are largely impacted by surface area input.

This work provides valuable insights on how different mineral species are impacted by mineral surface area variations over both short (10 – 100 hours) and long (1 – 20 years) period of times. It also provides guidance for surface area estimation/selection in reactive transport modeling. For example, when research interests are focused on short time simulations/experiments, quantifying the accessible surface area of the most reactive mineral phases (e.g. carbonate minerals) from imaging is highly recommended, whereas for longer time simulations/experiments, the surface area of these reactive mineral phases can be collected from the literature or use geometric approximations, and it is expected to yield similar results. This could potentially save plenty of time and computational cost.

6.3 Connections between the quantified mineral properties and estimation of mineral accessibility without image processing

In the third work presented in Chapter 4, we aim to find relationships among the mineral properties quantified from imaging to explore the possibility of predicting mineral accessible surface areas without complicated image processing steps. Ten sandstone samples that were imaged and processed through similar approaches were considered in this work for comparison. Mineral abundance, accessibility, accessible surface area, clay content and connected surface areas were cross-compared to determine the potential relationships. The most common mineral types in sandstone sample were discussed, namely quartz, feldspar (K-feldspar, albite), carbonate (calcite, dolomite) and clay minerals.

The analysis of this work revealed that mineral accessible surface area is highly dependent on the connected surface area, which is impacted by other factors such as quartz content, clay content, pore connectivity, etc. Therefore, it is challenging to directly link mineral accessible surface areas to other properties determined from the images. However, we found that mineral accessibility is predictable for quartz and feldspar minerals. The accessibilities of feldspar minerals are almost proportional to their abundances, while the accessibility of quartz is highly impacted by clay content. With that, the accessibility of these mineral phases can be interpreted with given abundances and clay content, which can be determined through X-ray diffraction analysis. The accessible mineral surface area can be then calculated by multiplying accessibility to the connected surface area obtained from 3D CT images.

The findings in this study can be beneficial to research that aims to quantify accessible mineral surface areas from imaging or utilize mineral accessible surface area for modeling purposes. With known mineral composition (e.g. measured through XRD analysis), the accessibility of the major mineral phases can be interpreted. The primary work load will be focus on quantifying the connected surface area from 3D CT images, which is non-destructive. This not only saves plenty of time and resources, but also preserve the sample integrity.

6.4 Mineral surface area evolution during mineral reactions

Currently, the commonly used theory in reactive transport modeling assumes mineral surfaces are smooth and mineral grains are spherical, where surface area evolves as the grain size changes. However, BSE images of geological samples reveals that majority of the mineral grains are not sphere, and more importantly, the surface of mineral phases has various degree of roughness. In the work presented in Chapter 5, core-flood experiments were designed and performed under room temperature using hydrochloric acid as the reactive fluid. Two geological samples (Kentucky and Bandera Grey) were placed in a 3D-printed core holder and reacted with 0.01 M hydrochloric acid (pH = 2) for 1 week (Kentucky) and 2 weeks (Bandera Grey).

2D BSE images and 3D CT images were captured before and after the experiments, mineral properties including porosity, abundances, accessibility and accessible surface area were then calculated from these images to evaluated any changes in these properties. The changes in mineral accessible surface area will be evaluated and compared with the changes of other mineral properties to evaluate the potential relationships.